Fourier Neural Operator-Based Models for Solving the Shallow Water Equations in Spherical Coordinates

Melissa Ulsøe Jessen (s194322)

Supervisor: Allan Peter Engsig-Karup, DTU Compute

Master Thesis
Mathematical Modelling and Computation

DTU Compute
Technical University of Denmark
February 2, 2025

Preface

This thesis has been prepared over five months at the Department of Applied Mathematics and Computer Science, at the Technical University of Denmark, DTU, in partial fulfillment of the requirements for the degree of Master of Science in Mathematical Modelling and Computation. The project was carried out from September 2024 to February 2025 and is equivalent to 30 ECTS points.

Melissa Ulsøe Jessen (s194322)

Abstract

This Master's thesis explores the integration of numerical and data-driven methodologies to solve the Shallow Water Equations (SWE), a cornerstone in computational fluid dynamics. Accurate and efficient simulation of shallow water dynamics is essential for critical applications such as flood forecasting, tsunami modeling, and coastal management. Traditional numerical approaches, such as the Finite Volume Method (FVM), solve partial differential equations (PDEs) by discretizing the domain into grids. While finer grids enhance accuracy, they substantially increase computational cost, posing a trade-off between accuracy and efficiency.

To address this challenge, this study focuses on solving the SWE in 1D, 2D, and 1D spherical coordinates while comparing Fourier Neural Operators (FNOs) and Convolutional Neural Networks (CNNs) as data-driven approaches. The generated data from the Finite Volume Method is used to train these models. FNOs learn mappings between function spaces, enabling grid-independent solution transfer and efficient handling of non-linearities. This allows FNOs to achieve zero-shot super-resolution by transferring solutions seamlessly between coarse and fine meshes. In contrast, CNNs operate on fixed grids, offering a complementary perspective on spatially localized features.

The thesis evaluates the performance of FNOs and CNNs in predicting the evolution of water levels and assesses their computational efficiency and accuracy. By training on coarse grids and inferring solutions on finer grids, both approaches demonstrate potential scalability and adaptability for real-time applications. The results highlight the strengths and limitations of each method, with FNOs excelling in grid-independent operations and CNNs providing robust localized feature extraction.

This work contributes a comprehensive computational toolkit for solving SWE, combining traditional numerical techniques with advanced neural network methodologies. The findings emphasize the potential of integrating Fourier Neural Operators and Convolutional Neural Networks into hydrodynamic modeling frameworks, paving the way for enhanced disaster preparedness and water resource management.

Acknowledgements

Acronyms

ANN Artificial Neural Network

CNN Convolutional Neural Network

FDM Finite Difference Method

FEM Finite Element Method

FNN Feedforward Neural Network

FNO Fourier Neural Operator

FVM Finite Volume Method

IC Initial Condition

IVP Initial Value Problem

LSWE Linearized Shallow Water Equations

LSTM Long Short-Term Memory

ODE Ordinary Differential Equation

PDE Partial Differential Equation

PINN Physics-Informed Neural Network

SWE Shallow Water Equations

Contents

Chapter 1

Introduction

This chapter provides the motivation for the project, explaining the background and key objectives of the thesis. It also includes a literature review, outlining the key sources relevant to this work. Finally, this chapter offers an overview of the thesis and its structure.

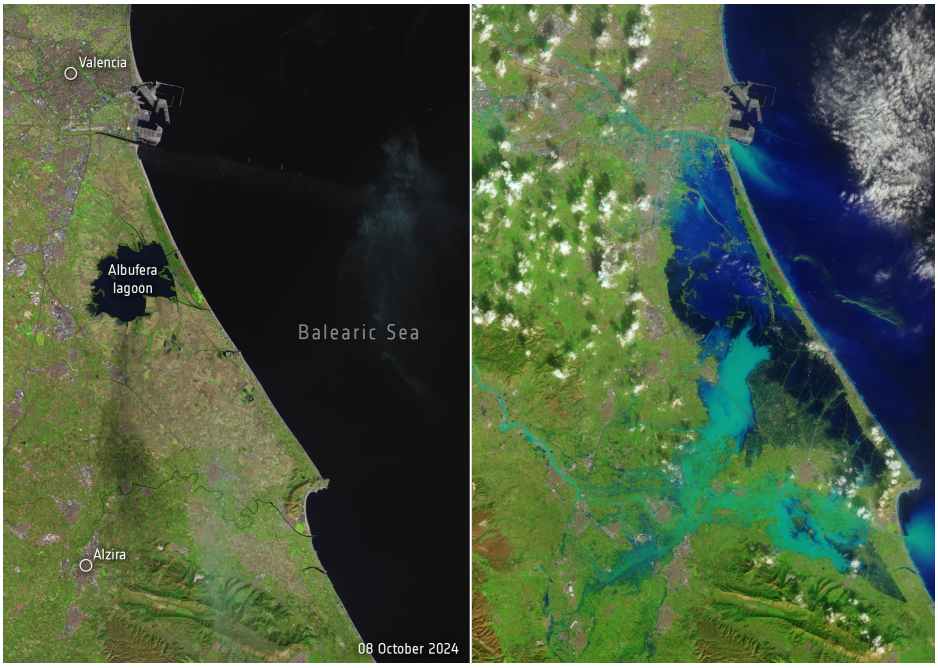

Figure 1.1: Before and after the floods in Valencia, Spain, October 2024.
Source: `https://www.esa.int/ESA_Multimedia/Images/2024/10/Valencia_flood_disaster`.

1.1 Motivation

The Shallow Water Equations (SWE) are a set of hyperbolic partial differential equations that describe the motion of a fluid in a shallow layer of water. These equations are crucial for understanding and simulating water dynamics in shallow water regions, such as coastal areas, rivers, and flood-prone regions. A wide range of problems can be

modeled by the shallow water equations, such as flooding, tsunamis and dam break scenarios. Recent catastrophic events, such as the floods in the Valencia region of Spain in late October 2024, highlight the urgent need for efficient tools to simulate and understand flood behavior. On October 29, 2024, Valencia received a years worth of rain in just eight hours, leading to flash floods that devastated the area, resulting in significant loss of life and property damage [1].

While it is impossible to prevent such disasters from occurring, a robust toolkit to solve the shallow water equations can help us simulate the spreading of floods quickly. This can aid in emergency response and disaster management. The ability to rapidly simulate flood scenarios could significantly reduce the time needed for decision-making in critical situations. Traditional numerical methods already exist to solve the SWE, but their accuracy often comes at the cost of high computational demands. In many cases, the run time can be too long, meaning simulations may be too slow to provide real-time insight during a flood event. This motivates the investigation of data-driven approaches to solve the SWE faster while maintaining an acceptable level of accuracy.

By investigating data-driven methods, this project aims to determine whether they can offer a faster and more efficient way to solve the shallow water equations compared to traditional numerical methods, ultimately improving our ability to respond to and manage flooding disasters. In this work, we will derive the SWE in 1D, 2D, and spherical coordinates to model the flow of water on the Earth's surface. We will explore the Finite Volume Method (FVM) in 1D and 2D, a numerical technique for solving partial differential equations by dividing the domain into small control volumes and integrating the equations over these volumes. This method is widely used in computational fluid dynamics to model fluid behavior. We will implement the FVM and use it to solve the SWE in 1D for several problems, including the dam break problem. We will then extend this approach to 2D and solve the idealized circular dam break problem. The FVM solvers will be validated by comparing them with known test cases, as this validation is critical for generating the data needed to train the data-driven approaches, such as Convolutional Neural Networks (CNN) and Fourier Neural Operators (FNO). The data-driven models will be trained and evaluated based on key performance metrics such as run time, accuracy, long-term prediction capabilities (i.e., their ability to generalize to unseen data), grid transferability, and their response to new initial conditions. These initial conditions could include varying water heights, velocities, and other environmental factors that may change in real-world flood scenarios. We will analyze the advantages and disadvantages of these data-driven methods and compare their run times with those of traditional numerical methods. This comparison will allow us to assess whether data-driven approaches offer a practical solution to efficiently solving the shallow water equations, ultimately improving disaster response and flood prediction, even under varying and unforeseen initial conditions.

1.2 Literature

When working in this area it inevitably to mention the work of E. F. Toro, who has written several books on the topic of Riemann solvers and the Finite Volume Method, specifically for the shallow water equations. In this project, we will use the books *Shock-Capturing Methods for Free-Surface Shallow Flows* [2], *Riemann Solvers and Numerical Methods for Fluid Dynamics* [3] and the rather new book from 2024 *Computational Algorithms for Shallow Water Equations* [4] as references. The books have been especially useful when deriving the shallow water equations and the Riemann solvers used in this project, as well as understanding and describing the Finite Volume Method. The course *Advanced Numerical Methods for Environmental Models* at the University of Trento, has provided a good foundation for the numerical methods used in this project, both in terms of lecture notes and exercises [5].

Working with the shallow water equations in spherical coordinates, the papers *Well-balanced methods for the shallow water equations in spherical coordinates* by Castro et al. [6] and *Physics-informed neural networks for the shallow-water equations on the sphere* by Bihlo et al. [7] are key references for deriving the SWE in spherical coordinates. Additionally, the lecture notes *Shallow water on a sphere* by Raymond from New Mexico Tech [8] have been valuable in this derivation. Further, the papers by Gavete [9] and Galewsky [10] also provide important insights into the spherical shallow water equations. Implementing the FVM to solve the shallow water equations in spherical coordinates is a challenging task, as exact literature on the topic is limited. However, some sources

discussing the Discontinuous Galerkin scheme for solving the spherical shallow water equations have been somewhat useful in this cont

The field of Fourier Neural Operators (FNO) is relatively new, and as a result, there is limited literature on the topic. However, the paper *Fourier Neural Operator for Parametric Partial Differential Equations* [11], written by several authors, is a key reference. In the last years the company Nvidia has done some very interesting work on the topic of FNO, and they have published several blog posts on the topic. One of the posts consider the use of Spherical Fourier Neural Operators (SFNO) to generate weather forecasts around the globe [12]. Another paper is [13]. These papers suggest that FNOs has shown great potential in being an efficient and resolution independent operator in the field of scientific machine learning. Suggested, a key reason their success is their ability to make long-term predictions. The papers also explains the introduction of Spherical FNOs (SFNOs) for learning operators on spherical geometries. Convolutional Neural Networks (CNNs) are a well-researched area, with numerous sources available on the topic. For this project, the sources [14] and [15] have been particularly helpful in explaining the theoretical foundations of the methods.

1.3 Thesis overview

In chapter 2, we derive the shallow water equations in 1D, 2D, and spherical coordinates. In chapter 3, we present the Finite Volume Method (FVM) used to solve the shallow water equations, including the Riemann problem and the numerical fluxes essential for the FVM. These chapters form the theoretical and methodological foundation for the numerical methods employed in this project, leading into the discussion of data-driven methods.

In chapter 4, we introduce the concepts of Fourier Neural Operators (FNO) and Convolutional Neural Networks (CNN), explaining how these methods can be applied to solve the shallow water equati In chapter 5, we describe the process of generating the data required for the data-driven methods, as we produce all the data used in this project ourselves.

Chapter 6 focuses on the numerical results for the 1D and 2D shallow water equations using the FVM. To validate these results, we compare the FVM outputs with test cases from the literature. Validation is crucial since the data-driven models are trained on the FVM data. In chapter 7, we present the results for the shallow water equations using the data-driven models, comparing performance in terms of runtime and accuracy. We analyze the outcomes, discuss the performance of the data-driven models, and compare them to the numerical results.

Finally, in chapter 8, we discuss the findings, and in chapter 9, we conclude the thesis and propose directions for future work.

Chapter 2

The Shallow Water Equations

In this chapter, we explore the theory behind the shallow water equations (SWE). We begin by introducing the relevant notation used throughout the report. Next, we derive the nonlinear SWE in conservative form and present them in both vector and integral forms for 1D and 2D in cartesian coordinates. Finally, we extend the derivation to spherical coordinates, addressing both the linear and nonlinear cases.

2.1 Notation

Before deriving the shallow water equations (SWE), we will introduce the notation that will be used throughout this report. In both the 1D case and the 2D case of the SWE, we use cartesian coordinates (x, y, z) with time denoted by t. Given that linear algebra is a fundamental tool used in this report, we first establish the relevant notation. Lowercase bold letters represent vectors, while uppercase bold letters represent matrices. For instance, $\mathbf{a}$ is a vector of size $r \times 1, r \in \mathbb{R}$, and $\mathbf{A}$ is a matrix of size $m \times n, m, n \in \mathbb{R}$. The identity matrix, denoted by $\mathbf{I}$, is a square matrix with ones along the diagonal and zeros elsewhere. For example, the 3×3 identity matrix is given by:

$$\mathbf{I} = \begin{bmatrix} 1 & 0 & 0 \\ 0 & 1 & 0 \\ 0 & 0 & 1 \end{bmatrix}.$$

In this project, differential calculus plays a significant role. We denote partial derivatives using the following notation:

$$f_x = \frac{\partial f}{\partial x}, \quad f_y = \frac{\partial f}{\partial y}, \quad f_z = \frac{\partial f}{\partial z}. \tag{2.1.1}$$

The gradient operator, denoted by ∇, gives the gradient of a scalar function $f(x, y, z)$ as a vector:

$$\nabla f = \begin{bmatrix} \frac{\partial f}{\partial x} & \frac{\partial f}{\partial y} & \frac{\partial f}{\partial z} \end{bmatrix}$$

Given two vectors $\mathbf{a} = \begin{bmatrix} a_1 & a_2 & a_3 \end{bmatrix}^\top$ and $\mathbf{b} = \begin{bmatrix} b_1 & b_2 & b_3 \end{bmatrix}^\top$, the dot product of $\mathbf{a}$ and $\mathbf{b}$ is given by:

$$\mathbf{a} \cdot \mathbf{b} = a_1 b_1 + a_2 b_2 + a_3 b_3.$$

The dot product can also be written as a matrix product:

$$\mathbf{a} \cdot \mathbf{b} = \mathbf{a}^\top \mathbf{b}.$$

The divergence operator, represented as $\nabla\cdot$, gives the divergence of a vector $\mathbf{a}$ as:

$$\nabla \cdot \mathbf{a} = \frac{\partial a_1}{\partial x} + \frac{\partial a_2}{\partial y} + \frac{\partial a_3}{\partial z} = a_{1x} + a_{2y} + a_{3z},$$

using the notation for partial derivatives introduced in (2.1.1). The tensor product of two vectors $\mathbf{a}$ and $\mathbf{b}$, denoted as $\mathbf{a} \otimes \mathbf{b}$, is a matrix where each element is the product of the elements of $\mathbf{a}$ and $\mathbf{b}$, i.e.,

$$\mathbf{a} \otimes \mathbf{b} = \begin{bmatrix} a_1b_1 & a_1b_2 & a_1b_3 \\ a_2b_1 & a_2b_2 & a_2b_3 \\ a_3b_1 & a_3b_2 & a_3b_3 \end{bmatrix}.$$

Establishing this relevant notation, we can now derive the shallow water equations.

2.2 Derivation of the SWE with conservative variables

Now, we can begin the derivation of the shallow water equations (SWE) in conservative form. The Shallow Water Equations (SWE) are a set of hyperbolic partial differential equations that describe the motion of a fluid in a shallow layer of water. The SWE are derived from the conservation laws for mass and momentum, and are fundamental in fluid dynamics. The derivation follows four steps: First we consider the conservation laws for mass and momentum, and then we consider the boundary conditions for a free surface problem. Afterwards we make some neccessary assumptions and finally we use the boundary conditions to integrate the conservation laws over depth. The derivation follows the methods outlined in [2] and [16].

Conservation laws

The SWE are derived from the conservation laws for mass and momentum, which are fundamental in fluid dynamics. The conservation laws for mass and momentum can be expressed generally as follows (source: eq. (2.1) and (2.2) in [2]):

$$\rho_t + \nabla \cdot (\rho \mathbf{v}) = 0, \tag{2.2.1}$$

$$(\rho \mathbf{v})_t + \nabla \cdot (\rho \mathbf{v} \otimes \mathbf{v} + p\mathbf{I} - \mathbf{T}) = \rho \mathbf{g}, \tag{2.2.2}$$

where ρ is the fluid density, $\mathbf{v} = \begin{bmatrix} u & v & w \end{bmatrix}^\top$ is the fluid velocity in the x, y and $z-$direction respectively, p is the pressure, $\mathbf{I}$ is the identity matrix, and the vector $\mathbf{g} = \begin{bmatrix} g_1 & g_2 & g_3 \end{bmatrix}^\top$ represents body forces including gravity. In these equations, the density ρ and the pressure p are dependent of x, y, z and t, but later we will introduce some assumptions that simplify the equations. The matrix $\mathbf{T}$ is the viscous stress tensor, given by

$$\mathbf{T} = \begin{bmatrix} \tau_{xx} & \tau_{xy} & \tau_{xz} \\ \tau_{yx} & \tau_{yy} & \tau_{yz} \\ \tau_{zx} & \tau_{zy} & \tau_{zz} \end{bmatrix},$$

which accounts for the viscous forces in the fluid. However, in this project the viscous stress tensor $\mathbf{T}$ is neglected, since we assume the function $\tau(x, y, z)$ is constant. The matrix $\mathbf{v} \otimes \mathbf{v}$ represents the tensor product of the velocity vector $\mathbf{v}$ with itself, i.e.,

$$\mathbf{v} \otimes \mathbf{v} = \begin{bmatrix} u^2 & uv & uw \\ vu & v^2 & vw \\ wu & wv & w^2 \end{bmatrix}.$$

Note that $\mathbf{v} \otimes \mathbf{v} = \mathbf{v}\mathbf{v}^\top$. Putting this together, we can rewrite the momentum equation (2.2.2) as

$$(\rho \mathbf{v})_t + \nabla \cdot (\rho \mathbf{v}\mathbf{v}^\top + p\mathbf{I}) - \rho \mathbf{g} = 0. \tag{2.2.3}$$

Applying the divergence operator and the product rule for differentiation, we can write out the mass equation (2.2.1) as

$$\rho_t + \rho(u_x + v_y + w_z) + u\rho_x + v\rho_y + w\rho_z = 0.$$

In this project we consider incompressible fluids, meaning that the fluid density ρ is independent of the pressure p. We also assume that the fluid density only depends on temperature and salinity, and thus is independent of t, x, y and z. Additionally, we assume ρ is nonzero. Hence we obtain

$$u_x + v_y + w_z = 0, \tag{2.2.4}$$

also referred to as the mass conservation equation. Applying the divergence operator $\nabla\cdot$, the momentum conservation equation (2.2.3) can be written out as:

$$\rho_t \mathbf{v} + \rho \mathbf{v}_t + \rho \begin{bmatrix} (u^2+p)_x + (uv)_y + (uw)_z \\ (vu)_x + (v^2+p)_y + (vw)_z \\ (wu)_x + (wv)_y + (w^2+p)_z \end{bmatrix} - \rho \mathbf{g} = 0. \tag{2.2.5}$$

We neglect all body forces in $\mathbf{g}$, expect the gravitational force in the $z-$direction, i.e., $\mathbf{g} = \begin{bmatrix} 0 & 0 & -g \end{bmatrix}$, where g is the gravity acceleration, which we assume to be constant. Hence, by using the product rule in (2.2.5) and that $\rho_t = 0$ we obtain

$$\rho \begin{bmatrix} u_t \\ v_t \\ w_t \end{bmatrix} + \rho \begin{bmatrix} p_x + uu_x + vu_y + wu_z + u(u_x + v_y + w_z) \\ p_y + uv_x + vv_y + wv_z + v(u_x + v_y + w_z) \\ p_z + uw_x + vw_y + ww_z + w(u_x + v_y + w_z) \end{bmatrix} - \rho \begin{bmatrix} 0 \\ 0 \\ -g \end{bmatrix} = 0. \tag{2.2.6}$$

We apply (2.2.4) to (2.2.6) to remove some terms, we move the pressure terms to the right hand side, and we divide by ρ. Putting it all together, the mass equation (2.2.1) and the momentum equation (2.2.3), split in x, y and $z-$directions, simplify to

$$\left.\begin{aligned} u_x + v_y + w_z &= 0, \\ u_t + uu_x + vu_y + wu_z &= -\frac{1}{\rho} p_x, \\ v_t + uv_x + vv_y + wv_z &= -\frac{1}{\rho} p_y, \\ w_t + uw_x + vw_y + ww_z &= -\frac{1}{\rho} p_z - g. \end{aligned}\right\} \tag{2.2.7}$$

Boundary conditions

The focus is on the flow of water with a free surface, meaning that the surface is not fixed and can move or change over time. To solve the SWE, it is essential to impose boundary conditions at both the bottom of the water column and at the free surface. We assumme the bottom b is defined by a function

$$z = b(x, y),$$

meaning that the bottom is dependent on x and y, but not on the time t. Since the bottom is not moving over time, we refer to it as fixed. The free surface is defined by

$$z = s(x, y, t) \equiv b(x, y) + h(x, y, t),$$

where $h(x, y, t)$ is the water depth at time t. The following illustration helps to visualize the setup:

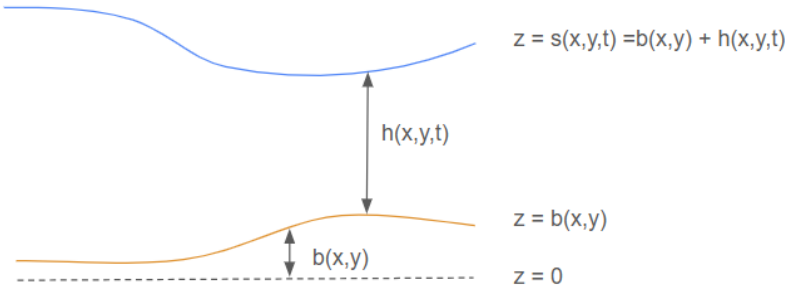

Figure 2.1: Illustration of a water column with a free surface.

We impose boundary conditions at the bottom and at the free surface, adressing both kinematic and dynamical conditions. To describe the boundaries mathematically, we introduce a boundary function $\psi(x, y, z, t)$ that is zero on the boundaries:

$$\psi(x, y, z, t) = 0.$$

For the free surface, this boundary is given by

$$\psi|_{z=s} = z - s(x, y, t) = 0, \tag{2.2.8}$$

and for the bottom, it is described by

$$\psi|_{z=b} = z - b(x, y) = 0. \tag{2.2.9}$$

In the kinematic condition, we assume that fluid particles on the boundary remain on the boundary over time. Mathematically this is expressed as

$$\frac{\mathrm{d}}{\mathrm{d}t}\psi(x, y, z, t) = 0.$$

Recall, that $\frac{\partial\psi}{\partial t}$ is the partial derivative of ψ with respect to t, while the total derivate $\frac{\mathrm{d}\psi}{\mathrm{d}t}$ accounts for both the direct change of ψ with respect to t and the changes due to the movement of the fluid in the x, y and z directions. Hence, the total derivative of ψ wrt. t is given by

$$\frac{\mathrm{d}\psi}{\mathrm{d}t} = \frac{\partial\psi}{\partial t} + \frac{\mathrm{d}x}{\mathrm{d}t}\frac{\partial\psi}{\partial x} + \frac{\mathrm{d}y}{\mathrm{d}t}\frac{\partial\psi}{\partial y} + \frac{\mathrm{d}z}{\mathrm{d}t}\frac{\partial\psi}{\partial z}.$$

We see that $\frac{\mathrm{d}x}{\mathrm{d}t}$ denotes the velocity in the $x-$direction, i.e., u, and correspondingly $\frac{\mathrm{d}y}{\mathrm{d}t}$ and $\frac{\mathrm{d}x}{\mathrm{d}t}$ denotes v and w respectively. Thus, the kinematic condition is given by

$$\frac{\mathrm{d}}{\mathrm{d}t}\psi = \psi_t + u\psi_x + v\psi_y + w\psi_z = 0. \tag{2.2.10}$$

Applying this to the free surface by substituting (2.2.8) into the kinematic condition (2.2.10) yields

$$(s_t + us_x + vs_y - w)|_{z=s} = 0. \tag{2.2.11}$$

Similarly, for the bottom, substitung (2.2.9) into the kinematic condition (2.2.10) gives

$$(ub_x + vb_y - w)|_{z=b} = 0. \tag{2.2.12}$$

The dynamical condition is related to the pressure distribution at the free surface. We assume that the pressure at the free surface is equal to the pressure in the air above the surface, that is, the atmospheric pressure. Since absolute pressure levels are irrelevant, as we are primarily concerned with pressure differences, we set the pressure at the free surface to zero. This leads to the following expression for the pressure at the free surface:

$$p(x, y, z, t)|_{z=s} = 0. \tag{2.2.13}$$

This condition, known as the dynamical condition, relates to the forces acting on the boundaries of the fluid.

Assumptions

To derive the SWE it is neccessary to make some physical assumptions. The shallow water equations are an approximation to the full free-surface problem and result from the assumption that the vertical compononent of the acceleration is negligible. Therefore, we begin by assuming that the vertical acceleration, represented by the total derivative of the vertical velocity component w with respect to time, is negligible. This assumption leads to the condition

$$\frac{\mathrm{d}w}{\mathrm{d}t} = w_t + uw_x + vw_y + ww_z = 0.$$

Applying $\frac{\mathrm{d}w}{\mathrm{d}t} = 0$ in the $z-$momentum conservation equation (2.2.7) simplifies it to

$$p_z = -\rho g.$$

By using properties of an integral, together with (2.2.13) we get

$$\int_{b(x,y)}^{z} -\rho g \ \mathrm{d}t + \int_{z}^{s(x,y,t)} -\rho g \ \mathrm{d}t = \int_{b(x,y)}^{s(x,y,t)} -\rho g \ \mathrm{d}t = p|_{z=s(x,y,t)} = 0.$$

This implies that the pressure distribution follows

$$p = \int_{b(x,y)}^{z} -\rho g \ \mathrm{d}t = \int_{z}^{s(x,y,t)} \rho g \ \mathrm{d}t = \rho g(s - z), \tag{2.2.14}$$

where s is the surface height. Differentiating (2.2.14) with respect to x and y yields

$$p_x = \rho g s_x, \quad p_y = \rho g s_y.$$

Substituting these expressions into the $x-$ and $y-$momentum conservation equations (2.2.7) leads to

$$\left.\begin{aligned} u_t + uu_x + vu_y + wu_z &= -gs_x, \\ v_t + uv_x + vv_y + wv_z &= -gs_y, \end{aligned}\right\} \tag{2.2.15}$$

which can be further simplified. We realize that both p_x and p_y are independent of z, implying that $\frac{\mathrm{d}u}{\mathrm{d}t}$ and $\frac{\mathrm{d}v}{\mathrm{d}t}$ are also independent of z. Hence $u_z = v_z = 0$, implying that (2.2.15) can be simplified to

$$\left.\begin{aligned} u_t + uu_x + vu_y &= -gs_x, \\ v_t + uv_x + vv_y &= -gs_y. \end{aligned}\right\} \tag{2.2.16}$$

These are the momentum equations for the shallow water equations in two dimensions.

Integration over depth

The next step in deriving the SWE is to integrate the conservation equations over the vertical direction z. We integrate the mass conservation equation (2.2.4) and the momentum conservation equations in (2.2.16), from the bottom, $z = b(x, y)$ to the free surface, $z = s(x, y, t)$. Starting with the mass conservation equation (2.2.4), we have

$$\int_{b}^{s} + v_y + u \, \mathrm{d}z = 0,$$

implying that, using linearity of the integral, we get

$$\int_{b}^{s} u_x \ \mathrm{d}z + \int_{b}^{s} v_y \ \mathrm{d}z + w|_{z=s} - w|_{z=b} = 0. \tag{2.2.17}$$

We will use Leibniz's integral rule [17], which is stated as follows:

$$\frac{\mathrm{d}}{\mathrm{d}x}\int_{a(x)}^{b(x)} f(x,t)\ \mathrm{d}t = \int_{a(x)}^{b(x)} \frac{\partial}{\partial x} f(x,t)\ \mathrm{d}t + f(x,b(x))\frac{\mathrm{d}}{\mathrm{d}x}b(x) - f(x,a(x))\frac{\mathrm{d}}{\mathrm{d}x}a(x), \tag{2.2.18}$$

to integrate the first two terms in (2.2.17), which yields

$$\left.\begin{aligned}\int_b^s u_x\,\mathrm{d}z &= \frac{\mathrm{d}}{\mathrm{d}x}\int_b^s u\,\mathrm{d}z - u|_{z=s}\frac{\mathrm{d}s}{\mathrm{d}x} + u|_{z=b}\frac{\mathrm{d}b}{\mathrm{d}x},\\ \int_b^s v_y\,\mathrm{d}z &= \frac{\mathrm{d}}{\mathrm{d}y}\int_b^s v\,\mathrm{d}z - v|_{z=s}\frac{\mathrm{d}s}{\mathrm{d}y} + v|_{z=b}\frac{\mathrm{d}b}{\mathrm{d}y}.\end{aligned}\right\} \tag{2.2.19}$$

Note that since a change in x does not affect the y-component of the bottom or surface, we have that $\frac{\mathrm{d}s}{\mathrm{d}x} = s_x$ and $\frac{\mathrm{d}b}{\mathrm{d}x} = b_x$, and correspondingly for s_y and b_y. Likewise we can substitute $\frac{\mathrm{d}}{\mathrm{dx}}$ with $\frac{\partial}{\partial x}$ in the integrals, since the integrals are with respect to z, and u and v are independent of z. Inserting these results in (2.2.19) gives

$$\left.\begin{aligned}\int_b^s u_x\ \mathrm{d}z &= \frac{\partial}{\partial x}\int_b^s u\ \mathrm{d}z - u|_{z=s}s_x + u|_{z=b}b_x,\\ \int_b^s v_y\ \mathrm{d}z &= \frac{\partial}{\partial y}\int_b^s v\ \mathrm{d}z - v|_{z=s}s_y + v|_{z=b}b_y.\end{aligned}\right\} \tag{2.2.20}$$

We can now insert the integrals (2.2.20) into the integrated mass conservation equation (2.2.17) to get

$$\frac{\partial}{\partial x}\int_b^s u\ \mathrm{d}z - u|_{z=s}s_x + u|_{z=b}b_x + \frac{\partial}{\partial y}\int_b^s v\ \mathrm{d}z - v|_{z=s}s_y + v|_{z=b}b_y + w|_{z=s} - w|_{z=b} = 0. \tag{2.2.21}$$

To simplify this equation further, we consider the boundary conditions. From (2.2.12) we have

$$w|_{z=b} = (ub_x + vb_y)|_{z=b}, \tag{2.2.22}$$

and from (2.2.11) we have

$$w|_{z=s} = (s_t + us_x + vs_y)|_{z=s}. \tag{2.2.23}$$

We note that $s = b + h$ and hence $s_t = h_t$, as the bottom is fixed. Recall that u and v are independent of z, and the water depth is $h = s - b$, meaning we have

$$\int_b^s u\ \mathrm{d}z = u(s-b) = hu, \quad \int_b^s v\ \mathrm{d}z = v(s-b) = hv.$$

Putting it all together the equation (2.2.21) simplifies to

$$h_t + (hu)_x + (hv)_y = 0, \tag{2.2.24}$$

which is also the first equation in the SWE in conservative form. When integrating the momentum equations (2.2.16) over the vertical direction, we see that since the equations are independent of z, the resulting equations are simply

$$\left.\begin{aligned}h(u_t + uu_x + vu_y + gs_x) &= 0,\\ h(v_t + uv_x + vv_y + gs_y) &= 0.\end{aligned}\right\} \tag{2.2.25}$$

We multiply (2.2.24) with u and v respectively, and add the resulting two equations to (2.2.25). Recall that $s = h + b$. By using the product rule for differentiation and collecting terms, we obtain the momentum equations in conservative form:

$$\left.\begin{aligned}(hu)_t + (hu^2 + \frac{1}{2}gh^2)_x + (huv)_y &= -ghb_x,\\ (hv)_t + (huv)_x + (hv^2 + \frac{1}{2}gh^2)_y &= -ghb_y.\end{aligned}\right\} \tag{2.2.26}$$

The three partial differential equations in (2.2.24) and (2.2.26) are the shallow water equations in conservative form.

2.3 The SWE in vector form

We present the SWE in vector form, which is useful as it allows all three partial differential equations to be combined into a single unified equation. The SWE can be written in differential conservation law form as the vector equation

$$\mathbf{U}_t + \mathbf{F}(\mathbf{U})_x + \mathbf{G}(\mathbf{U})_y = \mathbf{S}(\mathbf{U}), \tag{2.3.1}$$

where

$$\mathbf{U} = \begin{bmatrix} h \\ hu \\ hv \end{bmatrix}, \quad \mathbf{F}(\mathbf{U}) = \begin{bmatrix} hu \\ hu^2 + \frac{1}{2}gh^2 \\ huv \end{bmatrix}, \quad \mathbf{G}(\mathbf{U}) = \begin{bmatrix} hv \\ huv \\ hv^2 + \frac{1}{2}gh^2 \end{bmatrix} \quad \text{and} \quad \mathbf{S}(\mathbf{U}) = \begin{bmatrix} s_1 \\ s_2 \\ s_3 \end{bmatrix} = \begin{bmatrix} 0 \\ -ghb_x \\ -ghb_y \end{bmatrix}.$$

We call $\mathbf{U}$ the vector of conserved variables, $\mathbf{F}(\mathbf{U})$ and $\mathbf{G}(\mathbf{U})$ the flux vectors in the x and y direction, and $\mathbf{S}(\mathbf{U})$ the source term vector. Note that the source term vector $\mathbf{S}(\mathbf{U})$ often includes additional terms, such as the Coriolis force, friction, and other external forces. However, since only gravity is considered in this case, the source term vector is simplified to the expression shown above. Moreover, if $\mathbf{S}(\mathbf{U}) = 0$, then we consider a homogeneous equation, and if $\mathbf{S}(\mathbf{U}) \neq 0$, we consider an inhomogeneous equation.

We also consider the one-dimensional case of the SWE in vector form, where the flow is only in the $x-$direction. The vector form of the SWE in 1D is given by

$$\mathbf{U}_t + \mathbf{F}(\mathbf{U})_x = \mathbf{S}(\mathbf{U}), \tag{2.3.2}$$

where

$$\mathbf{U} = \begin{bmatrix} h \\ hu \end{bmatrix}, \quad \mathbf{F}(\mathbf{U}) = \begin{bmatrix} hu \\ hu^2 + \frac{1}{2}gh^2 \end{bmatrix} \quad \text{and} \quad \mathbf{S}(\mathbf{U}) = \begin{bmatrix} 0 \\ -ghb_x \end{bmatrix}. \tag{2.3.3}$$

When deriving schemes in the Finite Volume Method (FVM), the vector form of the 1D SWE can be used as a foundation. The 1D formulation is preferred over the 2D version for this purpose because the principles underlying the numerical schemes remain the same in both dimensions. Using the 1D SWE provides a simpler framework to introduce and analyze core aspects of the method, such as flux evaluation, conservation laws, and the treatment of source terms. Once these concepts are well-understood in 1D, the method can be extended to 2D by applying similar principles, with modifications to account for the additional spatial dimension and the directional components of fluxes and source terms.

2.4 The 1D SWE in integral form

It is often more convenient to work with the integral form of the SWE, since the integral form of equations of the form (2.3.2) and (2.3.3) allows discountinuous solutions. We derive the integral form of the inhomogeneous one-dimensional case of the SWE in vector form (2.3.2). The integral form is obtained by integrating the vector form (2.3.2) over a control volume V in the x, t plane

$$V = [x_L, x_R] \times [t_1, t_2].$$

The control volume is illustrated in Figure 2.2.

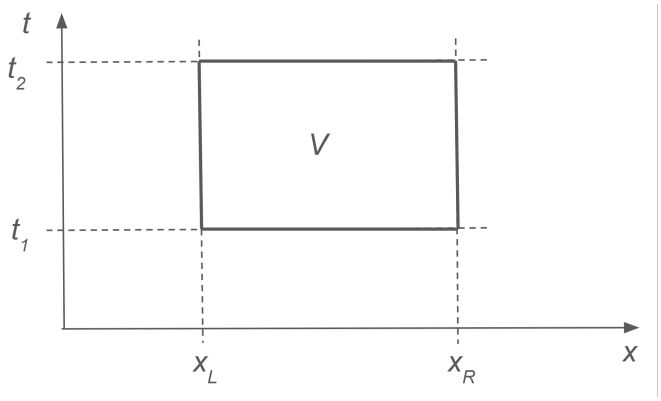

Figure 2.2: Illustration of a control volume V in the x, t plane. Illustration modified from [4].

First we integrate the vector form of the SWE (2.3.2) over x from x_L to x_R to obtain

$$\int_{x_L}^{x_R} \mathbf{U}_t \, \mathrm{d}x + \int_{x_L}^{x_R} \mathbf{F}(\mathbf{U})_x \, \mathrm{d}x = \int_{x_L}^{x_R} \mathbf{S}(\mathbf{U}) \, \mathrm{d}x. \tag{2.4.1}$$

Using the fundamental theorem of calculus, we get that

$$\int_{x_L}^{x_R} \mathbf{F}(\mathbf{U}) \, \mathrm{d}x = \mathbf{F}(\mathbf{U}(x_R, t)) - \mathbf{F}(\mathbf{U}(x_L, t)),$$

which we insert in (2.4.1):

$$\int_{x_L}^{x_R} \mathbf{U}_t \, \mathrm{d}x = \mathbf{F}(\mathbf{U}(x_L, t)) - \mathbf{F}(\mathbf{U}(x_R, t)) + \int_{x_L}^{x_R} \mathbf{S}(\mathbf{U}) \, \mathrm{d}x. \tag{2.4.2}$$

Then we integrate (2.4.2) over time from t_1 to t_2 to get

$$\int_{t_1}^{t_2} \int_{x_L}^{x_R} \mathbf{U}_t \, \mathrm{d}x\mathrm{d}t = \int_{t_1}^{t_2} \mathbf{F}(\mathbf{U}(x_L, t)) \, \mathrm{d}t - \int_{t_1}^{t_2} \mathbf{F}(\mathbf{U}(x_R, t)) \, \mathrm{d}t + \int_{t_1}^{t_2} \int_{x_L}^{x_R} \mathbf{S}(\mathbf{U}) \, \mathrm{d}x\mathrm{d}t.$$

Rewriting the left hand side using the fundamental theorem of calculus, we get

$$\int_{x_L}^{x_R} \mathbf{U}(x, t_2) \, \mathrm{d}x = \int_{x_L}^{x_R} \mathbf{U}(x, t_1) \, \mathrm{d}x + \int_{t_1}^{t_2} \mathbf{F}(\mathbf{U}(x_L, t)) \, \mathrm{d}t - \int_{t_1}^{t_2} \mathbf{F}(\mathbf{U}(x_R, t)) \, \mathrm{d}t + \int_{t_1}^{t_2} \int_{x_1}^{x_2} \mathbf{S}(\mathbf{U}) \, \mathrm{d}x\mathrm{d}t, \tag{2.4.3}$$

which is the integral form of the conservation laws for the SWE in 1D. An alternative integral form of (2.3.2) is stated in [4]:

$$\frac{\mathrm{d}}{\mathrm{d}t} \int_{x_L}^{x_R} \mathbf{U}(x, t) \, \mathrm{d}x = \mathbf{F}(\mathbf{U}(x_L, t)) - \mathbf{F}(\mathbf{U}(x_R, t)) + \int_{x_L}^{x_R} \mathbf{S}(\mathbf{U}) \, \mathrm{d}x. \tag{2.4.4}$$

From (2.4.4) we get that the integral form of the homogeneous SWE in 1D is given by

$$\frac{\mathrm{d}}{\mathrm{d}t} \int_{x_L}^{x_R} \mathbf{U}(x, t) \, \mathrm{d}x = \mathbf{F}(\mathbf{U}(x_L, t)) - \mathbf{F}(\mathbf{U}(x_R, t)), \tag{2.4.5}$$

meaning that the rate of change of the integral over a domain is equal to the flux through the boundaries of the domain. In chapter 3 we will use the integral form of the SWE (2.4.3) to derive the Finite Volume Method (FVM) for the SWE in 1D.

2.5 SWE in Spherical Coordinates

Until now we have derived the shallow water equations in cartesian coordinates. In this section, we will derive the shallow water equations in spherical coordinates. We will follow the methods used in [6] [7], [8] and [18]. To illustrate the spherical coordinates, we will use the latitude and longitude system, visualized in Figure 2.3.

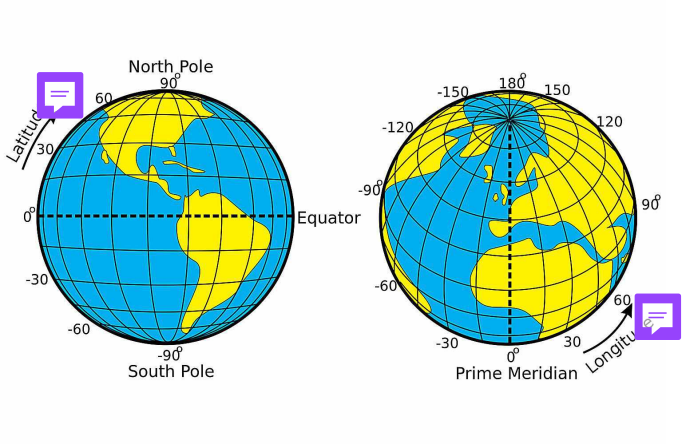

Figure 2.3: Illustration of latitude and longitude on the planet earth. Illustration from [19].

We see that the latitude direction is the north-south component, whereas the longitude direction is the east-west component. The latitude angle, denoted by ϕ, goes from $-\frac{\pi}{2}$ radians at the south pole to $\frac{\pi}{2}$ radians at the north pole, and the longitude angle, denoted by θ, goes from 0 at the prime meridian, increasing to the east, to 2π radians. The spherical coordinates we use are (r, θ, ϕ), where r is the radius from the center of the sphere, θ is the longitude angle, and ϕ is the latitude angle. Both angles are measured in radians. This also means, that any point on the surface of the sphere can be represented by the coordinates (θ, ϕ). We consider a small domain of the sphere, as illustrated in Figure 2.4.

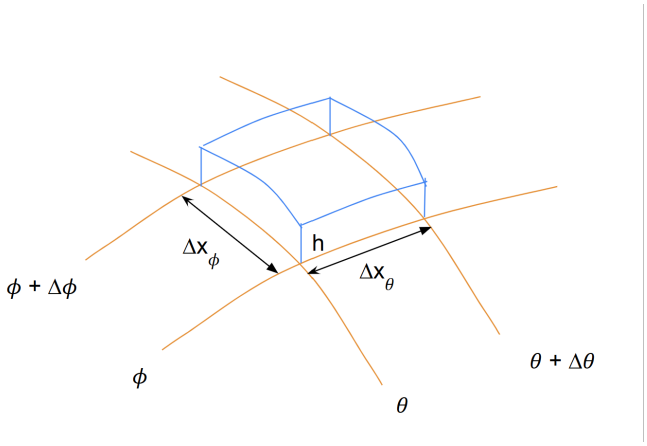

Figure 2.4: Illustrations of a small domain of the surface of the sphere.

We want to find expressions for Δx_ϕ and Δx_θ, the distances in the ϕ and θ directions, respectively, as illustrated in Figure 2.4. We can find these distances by using the arc length formula. Recall that the circumreference of a full circle is $2\pi r$, where r is the radius of the circle. The arc length is a fraction of the full circumreference, and it

is given by the formula $l = rv$, where l is the arc length, r is the radius, and v is the angle in radians. Assuming Earth's latitude side is a circle, we can find the distance Δx_ϕ by using the arc length formula, as:

$$\Delta x_\phi = r\Delta\phi,$$

where $\Delta\phi$ is the change in the latitude angle and r is the radius of the sphere. We assume that Earth is a perfect sphere, meaning that the radius is constant. Considering the distance in the longitude dimension Δx_θ, we need to make some adjustments, as we can see that the circumreference at equator is larger than at the poles. That is, we need to consider the radius of the circle at the given latitude ϕ. To illustrate this, we consider Figure 2.5.

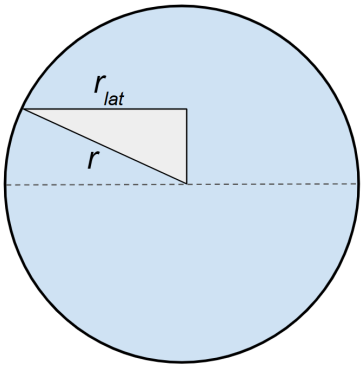

Figure 2.5: Illustration of the radius of the circle at the given latitude ϕ.

In Figure 2.5, we consider a right triangle with the hypotenuse as the radius of the sphere. The length of the adjacent side r_{lat} is the radius of the longitude circle at the given latitude ϕ. and the adjacent side as the radius of the circle at the given latitude ϕ. Thus, we can express the radius of the circle at the given latitude ϕ as

$$r_{lat} = r\cos(\phi).$$

Using that, together with the formula for the arc length, we can find the distance Δx_θ as:

$$\Delta x_\theta = r\cos(\phi)\Delta\theta.$$

We can then compute the volume of a small domain of the sphere, as shown in Figure 2.4. The volume V is given by

$$\begin{aligned} V &= \Delta x_\phi \Delta x_\theta h \\ &= r^2 h\cos(\phi)\Delta\phi\Delta\theta, \end{aligned}$$

assuming that the height of the domain is h, and that the domain is rectangular. This is a fair assumption for small values of Δx_ϕ and Δx_θ. We also assume that ϕ is not too close to the poles, as $\cos(\phi)$ will go to zero at the poles. We are interested in the rate of change of the volume with respect to time, and we can find this by taking the time derivative of the volume. That is, we consider the partial derivative with respect to time of the volume V:

$$\frac{\partial V}{\partial t} = r^2\cos(\phi)\Delta\phi\Delta\theta\frac{\partial h}{\partial t}, \tag{2.5.1}$$

where we have utilized that r is constant, and that $\cos(\phi), \Delta\phi$ and $\Delta\theta$ are independent of the time t. We use u_θ and u_ϕ to denote the velocities in the θ and ϕ increasing directions, respectively. We are interested in the rate at which fluid volume enters the region from the sides. We can find this rate by considering the flux of fluid volume through the sides of the domain. That is, we consider how much fluid volume enters the domain from the θ direction, and how much fluid volume enters the domain from the ϕ direction. We calculate the influx at the θ line and the outflux

at $\theta + \Delta\theta$ line, see Figure 2.4, to find the net flux. The influx is the area of the θ line times the velocity in the θ direction at the θ line. The influx is

$$F_{in} = u_\theta(\theta)h(\theta)r\Delta\phi,$$

where $h(\theta)$ is the height of the water at the θ line, assumed to be constant along the line. This way we can compute how much the volume changes due to the influx. For the outflux we do the same just for the $\theta+\Delta\theta$ line, introducing the notation $\theta' = \theta + \Delta\theta$ meaning the outflux is

$$F_{out} = u_\theta(\theta + \Delta\theta)h(\theta + \Delta\theta)r\Delta\phi = u_\theta(\theta')h(\theta')r\Delta\phi.$$

The net flux in the θ direction is the difference between the influx and the outflux, and is given by

$$F_{net} = F_{in} - F_{out} = \left(u_\theta(\theta)h(\theta) - u_\theta(\theta')h(\theta')\right) r\Delta\phi.$$

We can do the same for the ϕ direction, also using the notation $\phi' = \phi + \Delta\phi$. Using (2.5.1) and the net fluxes for both directions we can write:

$$r^2 h\cos(\phi)\Delta\phi\Delta\theta = \left(u_\theta(\theta)h(\theta) - u_\theta(\theta')h(\theta')\right) r\Delta\phi + \left(u_\phi(\phi)h(\phi)\cos(\phi) - u_\phi(\phi')h(\phi')\cos(\phi')\right) r\Delta\theta. \tag{2.5.2}$$

Since we are interested in the rate of change in the water height h with respect to time, we divide (2.5.2) by the area of the element $r^2\cos(\phi)\Delta\phi\Delta\theta$. Hence we get

$$\frac{\partial h}{\partial t} = \frac{u_\theta(\theta)h(\theta) - u_\theta(\theta')h(\theta')}{r\cos(\phi)\Delta\theta} + \frac{u_\phi(\phi)h(\phi)\cos(\phi) - u_\phi(\phi')h(\phi')\cos(\phi')}{r\cos(\phi)\Delta\phi}, \tag{2.5.3}$$

where $\phi \neq \pm\frac{\phi}{2}$. By collecting terms to the left hand side and changing the order of the numerators, we can rewrite (2.5.3) as

$$\frac{\partial h}{\partial t} + \frac{u_\theta(\theta')h(\theta') - u_\theta(\theta)h(\theta)}{r\cos(\phi)\Delta\theta} + \frac{u_\phi(\phi')h(\phi')\cos(\phi') - u_\phi(\phi)h(\phi)\cos(\phi)}{r\cos(\phi)\Delta\phi} = 0. \tag{2.5.4}$$

Next step is to investigate the limit values, as $\Delta\theta$ and $\Delta\phi$ goes to zero. We can find the limit values by using the definition of the derivative. The derivative of a function f with respect to x is defined as

$$f'(x) = \lim_{\Delta x\to 0}\frac{f(x+\Delta x) - f(x)}{\Delta x}.$$

We can use this definition to find the limit values in (2.5.4).

$$\lim_{\Delta\theta\to 0}\frac{u_\theta(\theta')h(\theta') - u_\theta(\theta)h(\theta)}{\Delta\theta} = \frac{\partial}{\partial\theta}(hu_\theta),$$

and

$$\lim_{\Delta\phi\to 0}\frac{u_\phi(\phi')h(\phi')\cos(\phi') - u_\phi(\phi)h(\phi)\cos(\phi)}{\Delta\phi} = \frac{\partial}{\partial\phi}(hu_\phi\cos(\phi)).$$

Inserting these results in (2.5.4) yields

$$h_t + \frac{1}{r\cos(\phi)}\left((hu_\theta)_\theta + (hu_\phi\cos(\phi))_\phi\right) = 0,$$

which is the mass conservation equation in spherical coordinates and is the first equation in the shallow water equations in spherical coordinates. The next step is to derive the momentum equations in spherical coordinates. In this case, we focus on the horizontal velocity components, specifically the velocity tangential to the surface of the sphere, i.e., the θ and ϕ velocities. The vertical velocity is neglected, as the key assumption in the shallow water equations is that the vertical component of the acceleration is negligible. Additionally, when considering Earth, the water layer is thin compared to the radius of the Earth, referred to as a thin-layer approximation. We need

to express the horizontal velocity u_h, which is dependent on the variables θ, ϕ and t. Since θ and ϕ are angles, we introduce the unit vectors $\mathbf{e}_\theta$ and $\mathbf{e}_\phi$ on the surface in the θ and ϕ directions, respectively. The unit vectors are illustrated in Figure 2.6.

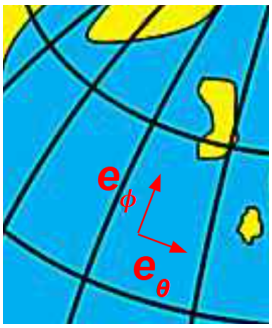

Figure 2.6: Illustration of the unit vectors $\mathbf{e}_\theta$ and $\mathbf{e}_\phi$.

We can express the horizontal velocity u_h in terms of the unit vectors as

$$u_h(\theta, \phi, t) = u_\theta \mathbf{e}_\theta + u_\phi \mathbf{e}_\phi. \tag{2.5.5}$$

We are then interested in the total derivative of the horizontal velocity u_h in (2.5.5) with respect to time. The total derivative is given by

$$\frac{\mathrm{d}u_h}{\mathrm{d}t} = \frac{\partial u_h}{\partial t} + \frac{\mathrm{d}\theta}{\mathrm{d}t}\frac{\partial u_h}{\partial \theta} + \frac{\mathrm{d}\phi}{\mathrm{d}t}\frac{\partial u_h}{\partial \phi}. \tag{2.5.6}$$

If we differentiate the longitude angle θ with respect to time, we get the angular velocity ω_θ in the θ direction, i.e.,

$$\frac{\mathrm{d}\theta}{\mathrm{d}t} = \omega_\theta,$$

meaning that if $\omega_\theta > 0$, the point is moving eastwards, and if $\omega_\theta < 0$, the point is moving westwards. Similarly, if we differentiate the latitude angle ϕ with respect to time, we get the angular velocity ω_ϕ in the ϕ direction, i.e.,

$$\frac{\mathrm{d}\phi}{\mathrm{d}t} = \omega_\phi,$$

meaning that if $\omega_\phi > 0$, the point is moving northwards, and if $\omega_\phi < 0$, the point is moving southwards. By using the arc length formula, we get that

$$\frac{\mathrm{d}\theta}{\mathrm{d}t} = \frac{u_\theta}{r\cos(\phi)}, \quad \frac{\mathrm{d}\phi}{\mathrm{d}t} = \frac{u_\phi}{r}. \tag{2.5.7}$$

We can now insert (2.5.7) into (2.5.6) to find the total derivative of the horizontal velocity split into the θ and ϕ directions:

$$\begin{aligned} \frac{\mathrm{d}u_\theta}{\mathrm{d}t} &= \frac{\partial u_\theta}{\partial t} + \frac{u_\theta}{r\cos(\phi)}\frac{\partial u_\theta}{\partial \theta} + \frac{u_\phi}{r}\frac{\partial u_\theta}{\partial \phi}, \\ \frac{\mathrm{d}u_\phi}{\mathrm{d}t} &= \frac{\partial u_\phi}{\partial t} + \frac{u_\theta}{r\cos(\phi)}\frac{\partial u_\phi}{\partial \theta} + \frac{u_\phi}{r}\frac{\partial u_\phi}{\partial \phi}. \end{aligned} \tag{2.5.8}$$

We know that the right hand side of (2.5.8) are the given physical forces acting on the fluid. Earlier in this project, we focused on the shallow water equations in cartesian coordinates, accounting solely for gravitational forces. However, in spherical coordinates, additional physical forces must be considered. These include the Coriolis force, centripetal acceleration, and the effects of Earth's curvature. First we consider the gravitational force acting

on the fluid, descibed as $-g\Delta h$, where g is the gravitational constant, and is the gradient of the height h. We consider the gradient of $h(\theta, \phi)$:

$$\Delta h = \frac{1}{r\cos(\phi)} h_\theta \mathbf{e}_\theta + \frac{1}{r} h_\phi \mathbf{e}_\phi, \tag{2.5.9}$$

meaning that the gravity force acting on the fluid in the θ and ϕ directions are given by:

$$\begin{aligned} \theta - \text{direction:} \quad & -\frac{g}{r\cos(\phi)} h_\theta, \\ \phi - \text{direction:} \quad & -\frac{g}{r} h_\phi. \end{aligned}$$

Hence, we obtain the two momentum equations in spherical coordinates as

$$\begin{aligned} (u_\theta)_t + \frac{u_\theta}{r\cos(\phi)}(u_\theta)_\theta + \frac{u_\phi}{r}(u_\theta)_\phi &= -\frac{g}{r\cos(\phi)} h_\theta + \text{other forces}, \\ (u_\phi)_t + \frac{u_\theta}{r\cos(\phi)}(u_\phi)_\theta + \frac{u_\phi}{r}(u_\phi)_\phi &= -\frac{g}{r} h_\phi + \text{other forces}. \end{aligned} \tag{2.5.10}$$

The next force we consider is the Coriolis force, which is a force that acts on moving objects on the surface of the earth [20]. The Coriolis force is given by $f = 2\Omega\sin(\phi)$, where Ω is the angular velocity of the earth. The Coriolis force in the θ and ϕ directions are then given by:

$$\begin{aligned} \theta - \text{direction:} \quad & f u_\phi, \\ \phi - \text{direction:} \quad & -f u_\theta. \end{aligned}$$

The last thing we need to take into account when working in the spherical domain is the curvature of the earth. This adds the following terms:

$$\begin{aligned} \theta - \text{direction:} \quad & \frac{u_\theta u_\phi}{r}\tan(\phi), \\ \phi - \text{direction:} \quad & -\frac{u_\theta^2}{r}\tan(\phi). \end{aligned}$$

There are several formulations of the SWE in spherical coordinates. Inserting these forces into the momentum equations, we get the following formulation of the shallow water equations in spherical coordinates:

$$\left.\begin{aligned} h_t + \frac{1}{r\cos(\phi)}\left((hu_\theta)_\theta + (hu_\phi\cos(\phi))_\phi\right) &= 0, \\ (u_\theta)_t + \frac{u_\theta}{r\cos(\phi)}(u_\theta)_\theta + \frac{u_\phi}{r}(u_\theta)_\phi - \frac{u_\theta u_\phi}{r}\tan(\phi) + \frac{g}{r\cos(\phi)} h_\theta - f u_\phi &= 0, \\ (u_\phi)_t + \frac{u_\theta}{r\cos(\phi)}(u_\phi)_\theta + \frac{u_\phi}{r}(u_\phi)_\phi + \frac{u_\theta^2}{r}\tan(\phi) + \frac{g}{r} h_\phi + f u_\theta &= 0, \end{aligned}\right\} \tag{2.5.11}$$

where r is the radius, (θ, ϕ) are the longitude and latitude angles, h is the height of the water, u_θ and u_ϕ are the velocities in the θ and ϕ directions, g is the gravitational constant.

2.6 Linearized SWE in Spherical Coordinates

In this section, we derive the linearized shallow water equations (SWE) in spherical coordinates, focusing on one spatial dimension, the longitude (θ), and time (t). This approach assumes a constant latitude (ϕ), simplifying the equations to a one-dimensional framework. The linearized SWE are employed for their simplicity, providing a foundation for understanding wave dynamics in a spherical geometry. Later in this project, we will apply the finite

volume method to solve these equations numerically. The derivation and methodology presented here are based on the sources [21] and [22]. We neglect all body forces other than gravity. We linearize by assuming that the height of the water h and the velocities u are small perturbations from a state of rest. We set $h = h_0 + h'$, $u = u_0 + u'$, where h_0 and u_0 are the equilibrium height and velocity, respectively, and h' and u' are the perturbations. We also assume that the equilibrium height h_0 is constant. To linearize the equations, we assume small perturbations around a mean state. Let the perturbations in water height and velocity be represented by:

$$h = h_0 + h', \quad u_\theta = u'_\theta, \quad u_\phi = u'_\phi,$$

where h_0 is the mean water height, and h', u'_θ, and u'_ϕ represent the perturbations in the water height and velocity components, respectively. Substituting these perturbed variables into the original equations and neglecting second-order terms (i.e., terms that involve products of perturbations), we obtain the following linearized shallow water equations:

$$\left.\begin{aligned} h'_t + \frac{h_0}{r\cos(\phi)} u'_\theta = 0, \\ u'_t + \frac{g}{r\cos(\phi)} h'_\theta = 0. \end{aligned}\right\} \tag{2.6.1}$$

These equations describe the evolution of small perturbations in water height and velocity on a spherical surface. We can also write the linearized shallow water equations in spherical coordinates in vector form as

$$\mathbf{W}_t + \mathbf{A}\mathbf{W}_\theta = 0, \tag{2.6.2}$$

where $\mathbf{W} = \begin{bmatrix} h' \\ u' \end{bmatrix}$ and the coefficient matrix $\mathbf{A}$ is constant and given as: $\mathbf{A} = \begin{bmatrix} 0 & \frac{h_0}{r\cos(\phi)} \\ \frac{g}{r\cos(\phi)} & 0 \end{bmatrix}$.

Integral form of the 1D spherical LSWE

As we consider the longitude θ as the spatial dimension, the domain is the circle $[0, 2\pi]$, which is divided into N cells or control volumes, each of length $\Delta\theta = \frac{2\pi}{N}$. Each cell i has a cell center at θ_i and cell boundaries/interfaces at $\theta_{i-1/2}$ and $\theta_{i+1/2}$.

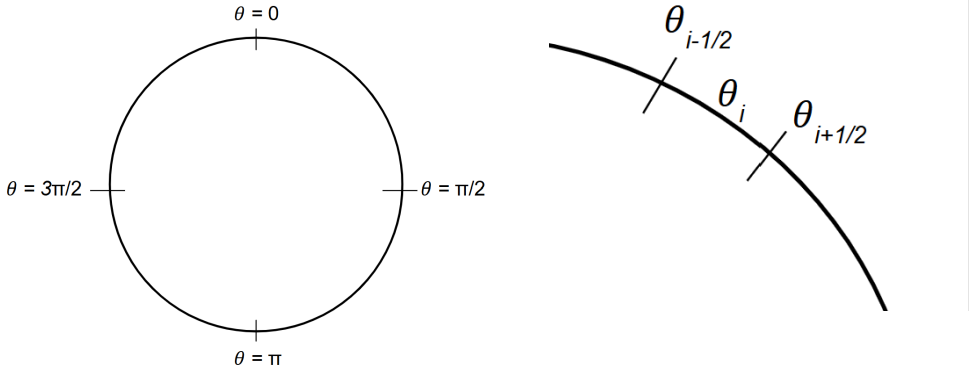

(a) Illustration of the grid for the 1D SWE with small cells.

(b) Illustration of the grid for the 1D SWE with a small domain.

Figure 2.7: Grid illustrations for the 1D SWE in spherical coordinates.

As when deriving the finite volume scheme for the 1D SWE in cartesian coordinates, we start by integrating the linearized shallow water equations over the control volume, and then divide by the cell length to obtain the finite volume scheme. We integrate the vector form of the 1D SWE in spherical coordinates without the coriolis force over θ from $\theta_L := \theta_i - \frac{1}{2}\Delta\theta$ to $\theta_R := \theta_i + \frac{1}{2}\Delta\theta$ to obtain

$$\int_{\theta_L}^{\theta_R} \mathbf{W}_t \, \mathrm{d}\theta + \int_{\theta_L}^{\theta_R} \mathbf{A}\mathbf{W}_\theta \, \mathrm{d}\theta = 0.$$

Since the matrix $\mathbf{A}$ is constant, we can take it out of the integral:

$$\int_{\theta_L}^{\theta_R} \mathbf{W}_t \, \mathrm{d}\theta + \mathbf{A}\int_{\theta_L}^{\theta_R} \mathbf{W}_\theta \, \mathrm{d}\theta = 0.$$

We also use the fundamental theorem of calculus to rewrite the integral of the derivative as the difference of the function at the boundari

$$\int_{\theta_L}^{\theta_R} \mathbf{W}_t \, \mathrm{d}\theta = \mathbf{A}\left(\mathbf{W}(\theta_L, t) - \mathbf{W}(\theta_R, t)\right). \tag{2.6.3}$$

We can also write the equations out to get a better understanding of the terms:

$$\left.\begin{aligned} \frac{\partial}{\partial t}\int_{\theta_L}^{\theta_R} h \, \mathrm{d}\theta + \frac{h_0}{r\cos(\phi)}(u_R - u_L) = 0, \\ \frac{\partial}{\partial t}\int_{\theta_L}^{\theta_R} u \, \mathrm{d}\theta + g(h_R - h_L) + f u_i = 0. \end{aligned}\right\} \tag{2.6.4}$$

Then we integrate (2.6.3) over time from $t_1 := t_n$ to $t_2 := t_{n+1}$:

$$\int_{t_1}^{t_2}\int_{\theta_L}^{\theta_R} \mathbf{W}_t \, \mathrm{d}\theta \, \mathrm{d}t = \mathbf{A}\left(\int_{t_1}^{t_2} \mathbf{W}(\theta_L, t) \, \mathrm{d}t - \int_{t_1}^{t_2} \mathbf{W}(\theta_R, t) \, \mathrm{d}t\right).$$

Rewriting, using the fundamental theorem of calculus, gives

$$\int_{\theta_L}^{\theta_R} \mathbf{W}(\theta, t_2) \, \mathrm{d}\theta = \int_{\theta_L}^{\theta_R} \mathbf{W}(\theta, t_1) \, \mathrm{d}\theta - \mathbf{A}\left(\int_{t_1}^{t_2} \mathbf{W}(\theta_R, t) \, \mathrm{d}t - \int_{t_1}^{t_2} \mathbf{W}(\theta_L, t) \, \mathrm{d}t\right), \tag{2.6.5}$$

which we refer to as the integral form of the linearized shallow water equations in spherical coordinates with one spatial dimension and time. The integral form (2.6.5) is the foundation for the finite volume method, which we will use to solve the linearized shallow water equations in spherical coordinates numerically.

Chapter 3

The Finite Volume Method

In this section, we present the finite volume method (FVM) for solving nonlinear systems of balance laws, specifically focusing on the shallow water equations (SWE). Nonlinear problems are more challenging than linear problems, as stability and convergence theory are more difficult to establish. In particular, when dealing with hyperbolic systems such as the SWE, the presence of discontinuities such as shock waves, hydraulic jumps, and rarefaction waves requires special treatment. Our focus is on discontinuous solutions, which can accurately capture these shocks and other discontinuities. The FVM provides a framework for dealing with such solutions in a robust and efficient manner. Unlike traditional methods, which may struggle to capture sharp gradients or discontinuities, FVM inherently incorporates a mechanism to resolve such features by solving local Riemann problems at the interfaces between computational cells. This characteristic makes it particularly well-suited for problems involving abrupt changes in the flow, such as those encountered in the modeling of floods, tsunamis, or dam breaks.

The approach described here is based on the work of LeVeque [23], who developed a framework for using FVM in the context of hyperbolic systems of partial differential equations. The key idea is to discretize the computational domain into small cells or control volumes and compute the fluxes across the boundaries of these cells. The solution within each cell is then updated using the information from neighboring cells, ensuring that conservation laws are satisfied. By solving the local Riemann problem at the cell interfaces, the FVM can accurately capture discontinuities and preserve the sharp transitions between different flow regimes. In addition to its ability to handle discontinuities, the FVM also has several other advantages, such as its ability to conserve mass, momentum, and energy in a discrete sense. This property is crucial when solving balance laws, as it ensures that the physical conservation laws are respected even at the discrete level. The method is also highly flexible, allowing for the use of unstructured grids, which can be beneficial for complex geometries and irregular domains. Despite its advantages, the finite volume method also has limitations. The accuracy of the method depends heavily on the choice of numerical flux function and the resolution of the computational grid. In the presence of strong discontinuities, additional techniques such as limiters or high-order schemes may be required to maintain stability and avoid spurious oscillations. Furthermore, while the FVM is well-suited for handling hyperbolic problems, it may not be as effective for problems with smooth solutions or for capturing fine-scale features in the solution without sufficient grid resolution.

In this chapter, we derive the finite volume scheme for the 1D SWE and extend it to 2D in cartesian coordinates. We introduce the MUSCL scheme for higher-order accuracy and discuss the finite volume method for the 1D linearized SWE in spherical coordinates. Additionally, we examine the Riemann problem, including the dam break test case, and present numerical flux functions for solving local Riemann problems at cell interfaces.

3.1 Finite Volume Methods for the 1D SWE

We begin by introducing finite volume methods for the SWE in one spatial dimension. Specifically, we work in the x, t-plane, discretizing the domain into finite control volumes, or cells. In chapter 2, we derived the integral form for a single control volume $V = [x_L, x_R] \times [t_1, t_2]$. Here, we extend this approach to a global domain consisting of multiple cells. To accommodate this, we update the notation: $x_{i-1/2}$ and $x_{i+1/2}$ denote the cell interfaces, while t_n and t_{n+1} represent the time levels. The control volume for cell i at time level n, V_i^n, is defined as:

$$V_i = [x_{i-1/2}, x_{i+1/2}] \times [t_n, t_{n+1}],$$

where $\Delta x = x_{i+1/2} - x_{i-1/2}$ is the length of the cell and $\Delta t = t_{n+1} - t_n$ is the time step. The cell V_i^n is illustrated in Figure 3.1.

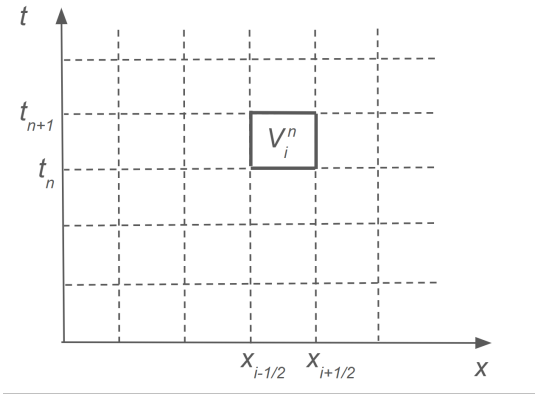

Figure 3.1: Illustration of the control volume V_i^n in the x, t plane.

The grid can be uniform or non-uniform, depending on the application. For now, we will assume a uniform grid for simplicity. The finite volume formula is derived from the integral form of the 1D SWE (2.4.3). The integral form stated in the new variables ($x_{i-1/2}$, $x_{i+1/2}$, t_n, t_{n+1}) over the cell V_i^n is given by

$$\begin{aligned}\int_{x_{i-1/2}}^{x_{i+1/2}} \mathbf{U}(x, t_{n+1})\, \mathrm{d}x = \int_{x_{i-1/2}}^{x_{i+1/2}} \mathbf{U}(x, t_n)\, \mathrm{d}x + \int_{t_n}^{t_{n+1}} \mathbf{F}(\mathbf{U}(x_{i-1/2}, t))\, \mathrm{d}t - \int_{t_n}^{t_{n+1}} \mathbf{F}(\mathbf{U}(x_{i+1/2}, t))\, \mathrm{d}t \\ + \int_{t_n}^{t_{n+1}} \int_{x_{i-1/2}}^{x_{i+1/2}} \mathbf{S}(\mathbf{U})(x, t) \mathrm{d}x \mathrm{d}t.\end{aligned} \tag{3.1.1}$$

We divide the integral form (3.1.1) by the cell length Δx to obtain

$$\begin{aligned}\frac{1}{\Delta x}\int_{x_{i-1/2}}^{x_{i+1/2}} \mathbf{U}(x, t_{n+1})\, \mathrm{d}x = \frac{1}{\Delta x}\int_{x_{i-1/2}}^{x_{i+1/2}} \mathbf{U}(x, t_n)\, \mathrm{d}x \\ - \frac{\Delta t}{\Delta x}\left[\frac{1}{\Delta t}\int_{t_n}^{t_{n+1}} \mathbf{F}(\mathbf{U}(x_{i+1/2}, t))\, \mathrm{d}t - \frac{1}{\Delta t}\int_{t_n}^{t_{n+1}} \mathbf{F}(\mathbf{U}(x_{i-1/2}, t))\, \mathrm{d}t\right] \\ + \frac{\Delta t}{\Delta x \Delta t}\int_{x_{i-1/2}}^{x_{i+1/2}} \int_{t_n}^{t_{n+1}} \mathbf{S}(\mathbf{U})(x, t) \mathrm{d}x \mathrm{d}t.\end{aligned}$$

To simplify the numerical implementation, we introduce cell-averaged values. These are defined as the averages of the conserved variables $\mathbf{U}$, the fluxes $\mathbf{F}$, and the source terms $\mathbf{S}$ over the volume V_i^n. This leads to the explicit conservative form of the finite volume scheme:

$$\mathbf{U}_i^{n+1} = \mathbf{U}_i^n - \frac{\Delta t}{\Delta x}\left(\mathbf{F}_{i+1/2}^n - \mathbf{F}_{i-1/2}^n\right) + \Delta t \mathbf{S}_i. \tag{3.1.2}$$

The value $\mathbf{U}_i^n$ is the average value over the i-th cell at time t_n:

$$\mathbf{U}_i^n = \frac{1}{\Delta x} \int_{x_{i-1/2}}^{x_{i+1/2}} \mathbf{U}(x, t_n)\, \mathrm{d}x,$$

also known as the cell average. The flux $\mathbf{F}_{i-1/2}^n$ is the average flux across the line $x = x_{i-1/2}$ from time t_n to t_{n+1}:

$$\mathbf{F}_{i-1/2}^n = \frac{1}{\Delta t} \int_{t_n}^{t_{n+1}} \mathbf{F}(\mathbf{U}(x_{i-1/2}, t))\, \mathrm{d}t,$$

and correspondingly the flux $\mathbf{F}_{i+1/2}^n$ is the average flux across the line $x = x_{i+1/2}$ from time t_n to t_{n+1}:

$$\mathbf{F}_{i+1/2}^n = \frac{1}{\Delta t} \int_{t_n}^{t_{n+1}} \mathbf{F}(\mathbf{U}(x_{i+1/2}, t))\, \mathrm{d}t.$$

The source term $\mathbf{S}_i$ is the average source term over the i-th cell at time t_n:

$$\mathbf{S}_i = \frac{1}{\Delta t \Delta x} \int_{t_n}^{t_{n+1}} \int_{x_{i-1/2}}^{x_{i+1/2}} \mathbf{S}(x, t)\, \mathrm{d}x\mathrm{d}t.$$

The values are illustrated in Figure 3.2.

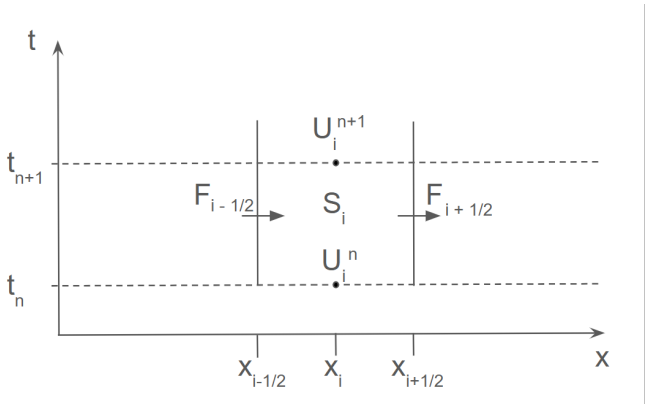

Figure 3.2: Illustration of the grid for the 1D SWE.

The central idea of the FVM is to define the numerical flux $\mathbf{F}_{i+1/2}^n$, at the cell interface, as a function of the cell averages $\mathbf{U}_i^n$ and $\mathbf{U}_{i+1}^n$, since the solution is known only in terms of these cell averages. Consequently, the FVM does not provide pointwise values of the solution, i.e., $\mathbf{U}(x, t)$, but instead gives cell-averaged values, $\mathbf{U}_i^n$, over the control volume. One of the main challenges in the FVM is to determine appropiate numerical flux functions that, based on the available cell averages, can reasonably approximate the fluxes at the cell interfaces. Later in the thesis, we will consider several numerical flux functions that can be used to solve the local Riemann problem at the cell interfaces.

Finite volume methods are closely related to Finite Difference Methods (FDM), but they differs as they are based on the integral form of the conservation laws. Where finite difference methods tend to break down near discontinuities in the solution, finite volume methods are more suited, since they are based on the integral form of the conservation laws. The key distinction between the FVM and the FDM lies in their formulation: while the FVM is based on the integral conservation over finite volumes, the FDM is based on the differential conservation over finite differences.

3.2 Finite Volume Method for the 2D SWE

We now extend the FVM to two space dimensions. Consider the 2D SWE in vector form (2.3.1) with $\mathbf{S}(\mathbf{U}) = 0$:

$$\mathbf{U}_t + \mathbf{F}(\mathbf{U})_x + \mathbf{G}(\mathbf{U})_y = 0. \tag{3.2.1}$$

Following the methods outlined in [3], an explicit finite volume scheme to solve (3.2.1) is given by

$$\mathbf{U}_{i,j}^{n+1} = \mathbf{U}_{i,j}^{n} - \frac{\Delta t}{\Delta x}(\mathbf{F}_{i+1/2,j} - \mathbf{F}_{i-1/2,j}) - \frac{\Delta t}{\Delta y}(\mathbf{G}_{i,j+1/2} - \mathbf{G}_{i,j-1/2}). \tag{3.2.2}$$

This is the unsplit finite volume method, meaning that, in a single step, the cell average $\mathbf{U}_{i,j}^{n}$ in cell $V_{i,j}$ is updated using the fluxes from all intercell boundaries. This means, that in each time step, we need to solve the Riemann problem at all cell interfaces, and then use the fluxes to update the cell averages. The fluxes $\mathbf{F}_{i-1/2,j}$ and $\mathbf{F}_{i+1/2,j}$ are the average fluxes across the lines $x = x_{i-1/2}$ and $x = x_{i+1/2}$. Correspondingly, the fluxes $\mathbf{G}_{i,j-1/2}$ and $\mathbf{G}_{i,j+1/2}$ are the average fluxes across the lines $y = y_{j-1/2}$ and $y = y_{j+1/2}$. We work on a domain discretized into rectangular cells of size $\Delta x \times \Delta y$, where $\Delta x = x_{j+1/2} - x_{j-1/2}$ and $\Delta y = y_{j+1/2} - y_{j-1/2}$. The fluxes are illustrated in the figure below.

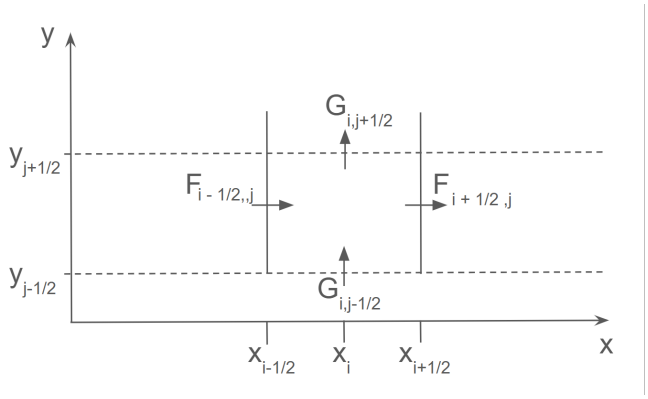

Figure 3.3: Illustration of the fluxes for the 2D SWE.

When using the simultaneous update scheme (3.2.2), we must consider potential stability issues. Certain numerical fluxes, such as those from the Lax-Friedrichs, Lax-Wendroff, and FORCE schemes, are not stable in 2D applications. To address this, several methods can be employed.

The first method we consider is the Weighted Average Flux (WAF) scheme. The basic WAF scheme, without any nonlinear TVD modification, is prone to oscillations. To mitigate this, a Total Variation Diminishing (TVD) constraint can be enforced. To achieve the TVD condition, additional constraints are imposed on the numerical flux or reconstruction process, often through the use of slope limiters. A limiter function is a technique used to reduce oscillations in the solution, especially near sharp edges or discontinuities, such as shock waves. For this project, we use the minmod limiter, defined as

$$\text{minmod}(a,b) = \begin{cases} \max(0, \min(a,b)) & \text{if } a > 0 \\ \min(0, \max(a,b)) & \text{if } a < 0. \end{cases}$$

Another method we consider is the MUSCL (Monotone Upwind Scheme for Conservation Laws) scheme. This method is second-order accurate in both time and space, while the WAF scheme is second-order accurate in space but relies on the time-stepping scheme for temporal accuracy. The MUSCL scheme, combined with slope limiters, ensures the solution remains satisfies the TVD constraint, effectively preventing oscillations that could occur with high-order spatial discretization near shocks, discontinuities, or sharp changes in the solution. The key idea in

MUSCL is that, instead of using cell averages as in the 1D finite volume method, we reconstruct the solution in each cell using piecewise first-degree polynomials. This reconstruction provides a higher-order representation of the solution within each cell. In this project, we use the MUSCL scheme with the TVD criteria to ensure smooth and stable solutions.

3.3 FVM 1D Linearized SWE spherical

In this section, we derive the finite volume method for the 1D shallow water equations in spherical coordinates, where we consider the linearized shallow water equations on a circle. Since we now work on a circle, we must impose periodic boundary conditions. We follow the same method as in section 3.1. We begin by stating the integral form of the 1D LSWE in spherical coordinates on a global domain. Each cell has length $\Delta\theta = \theta_{i+1/2} - \theta_{i-1/2}$. That is, we rewrite (2.6.5) to be in global variables:

$$\int_{\theta_{i-1/2}}^{\theta_{i+1/2}} \mathbf{W}(\theta, t_{n+1})\ \mathrm{d}\theta = \int_{\theta_{i-1/2}}^{\theta_{i+1/2}} \mathbf{W}(\theta, t_n)\ \mathrm{d}\theta - \mathbf{A}\left(\int_{t_n}^{t_{n+1}} \mathbf{W}(\theta_{i+1/2}, t)\ \mathrm{d}t - \int_{t_n}^{t_{n+1}} \mathbf{W}(\theta_{i-1/2}, t)\ \mathrm{d}t\right). \tag{3.3.1}$$

We divide the integral form (3.3.1) with the cell length $\Delta\theta$ to obtain

$$\begin{aligned}\frac{1}{\Delta\theta}\int_{\theta_{i-1/2}}^{\theta_{i+1/2}} \mathbf{W}(\theta, t_{n+1})\ \mathrm{d}\theta = \frac{1}{\Delta\theta}\int_{\theta_{i-1/2}}^{\theta_{i+1/2}} \mathbf{W}(\theta, t_n)\ \mathrm{d}\theta \\ - \frac{\Delta t}{\Delta\theta}\mathbf{A}\left(\frac{1}{\Delta t}\int_{t_n}^{t_{n+1}} \mathbf{W}(\theta_{i-1/2}, t)\ \mathrm{d}t - \frac{1}{\Delta t}\int_{t_n}^{t_{n+1}} \mathbf{W}(\theta_{i+1/2}, t)\ \mathrm{d}t\right).\end{aligned}$$

Averaging over the terms for a finite volume gives the first-order explicit time-stepping finite volume scheme:

$$\mathbf{W}_i^{n+1} = \mathbf{W}_i^n - \frac{\Delta t}{\Delta\theta}(\mathbf{F}_{i+1/2}^n - \mathbf{F}_{i-1/2}^n). \tag{3.3.2}$$

The scheme uses the cell averages:

$$\mathbf{W}_i^n = \frac{1}{\Delta\theta}\int_{\theta_{i-1/2}}^{\theta_{i+1/2}} \mathbf{W}(\theta, t_n)\ \mathrm{d}\theta$$

The flux $\mathbf{F}_{i-1/2}^n$ is the average flux across the line $\theta = \theta_{i-1/2}$ from time t_n to t_{n+1}:

$$\mathbf{F}_{i-1/2}^n = \frac{1}{\Delta t}\mathbf{A}\int_{t_n}^{t_{n+1}} (\mathbf{W}(\theta_{i-1/2}, t))\ \mathrm{d}t,$$

and correspondingly the flux $\mathbf{F}_{i+1/2}^n$ is the average flux across the line $\theta = \theta_{i+1/2}$ from time t_n to t_{n+1}:

$$\mathbf{F}_{i+1/2}^n = \frac{1}{\Delta t}\mathbf{A}\int_{t_n}^{t_{n+1}} (\mathbf{W}(\theta_{i+1/2}, t))\ \mathrm{d}t.$$

The Runge-Kutta 4th order method (RK4) is a numerical technique used to solve ordinary differential equations (ODEs). This method is particularly effective for time-stepping and is an alternative approach to traditional time integration schemes. RK4 provides higher accuracy in time while relying on the same spatial discretization, such as the finite volume method (FVM). In this context, the RK4 method is applied to numerically solve the linearized 1D shallow water equations in spherical coordinates:

$$\frac{\partial h'}{\partial t} = -\frac{h_0}{r\cos\phi}\frac{\partial u}{\partial \theta}, \tag{3.3.3}$$

$$\frac{\partial u}{\partial t} = -g\frac{\partial h'}{\partial \theta} - fu, \tag{3.3.4}$$

where h' is the perturbation in water height, u is the velocity, h_0 is the mean water depth, g is the gravitational acceleration, f is the Coriolis parameter, r is the Earth's radius, and ϕ is the fixed latitude. The RK4 method employs a four-stage time-stepping scheme to update the solution for h' and u. The general update formula is:

$$\mathbf{W}_i^{n+1} = \mathbf{W}_i^n + \frac{\Delta t}{\Delta \theta}\frac{1}{6}\left(k_1 + 2k_2 + 2k_3 + k_4\right),$$

where the state variable $\mathbf{W}_i = \begin{bmatrix} h_i' \\ u_i \end{bmatrix}$ represents the pertubation height and velocity at the $i-$th cell. The intermediate stages k_1, k_2, k_3 and k_4 are computed at each time step. The scheme integrates the equations in time while relying on flux differences to update the solution. At each time step, the fluxes $\mathbf{F}_i$ between neighboring cells are computed as

$$\mathbf{F}_i = \frac{1}{2}(\mathbf{F}_{i-1/2} + \mathbf{F}_{i+1/2}),$$

where $\mathbf{F}_{i-1/2}$ and $\mathbf{F}_{i+1/2}$ are the fluxes at the edges of the adjacent cells. These fluxes depend on h' and u. At each RK4 stage, the fluxes and intermediate derivatives are calculated to ensure accurate time integration. The final values of h' and u are obtained by combining the contributions from all four stages. This approach allows the method to achieve high temporal accuracy while maintaining the spatial resolution provided by the finite volume discretization.

3.4 The Riemann problem

We will now define the Riemann problem, since it plays a crucial role in the finite volume method. In the Riemann problem we distinguish between what we call a wet bed and a dry bed. A wet bed is the case where the water depth is positive everywhere, whereas a dry bed is the case where the water depth is zero in some cells. The special Riemann problem where parts of the bed are dry is dealing with the so-called dry fronts or wet/dry fronts, which are challenging to handle numerically. We will leave these cases for now, and only consider wet bed problems. The Riemann problem for the shallow water equations in 1D with a zero source term is defined as the initial-value problem (IVP) [4]:

$$\begin{aligned} &\text{PDEs: } \mathbf{U}_t + \mathbf{F}(\mathbf{U})_x = 0, \\ &\text{ICs: } \mathbf{U}(x,0) = \begin{cases} \mathbf{U_L}, & \text{if } x < 0, \\ \mathbf{U_R}, & \text{if } x > 0. \end{cases} \end{aligned} \tag{3.4.1}$$

The vectors $\mathbf{U}$ and $\mathbf{F}(\mathbf{U})$ in (3.4.1) are given by

$$\mathbf{U} = \begin{bmatrix} h \\ hu \\ hv \end{bmatrix}, \quad \mathbf{F}(\mathbf{U}) = \begin{bmatrix} hu \\ hu^2 + \frac{1}{2}gh^2 \\ hvu \end{bmatrix}, \tag{3.4.2}$$

and the initial conditions $\mathbf{U_L}$ and $\mathbf{U_R}$ are

$$\mathbf{U_L} = \begin{bmatrix} h_L \\ h_L u_L \\ h_L v_L \end{bmatrix}, \quad \mathbf{U_R} = \begin{bmatrix} h_R \\ h_R u_R \\ h_R v_R \end{bmatrix},$$

which represents the conditions at time $t = 0$ in the left and right states of $x = 0$ respectively. The function $\mathbf{U}$ is piecewise constant, with a discontinuity at $x = 0$. The Riemann problem can be solved either exactly or approximately. However, in this project we will focus on approximate Riemann solvers, which are able to solve the Riemann problem with high accuracy and efficiency. Various approximate Riemann solvers exist, based on finding an approximate solution to the Riemann problem. Some of these solvers will be considered in the next section. An interesting example of a Riemann problem is the so-called dam break problem, which is presented next.

3.4.1 The Dam-Break problem

We now introduce the dam-break problem, a scenario of significant physical interest. This problem models the sudden release of water following the collapse of a dam, making it highly relevant for studying natural disasters such as floods and tsunamis. As a classic test case for numerical methods, the dam-break problem is commonly used to test the ability of a method to capture discontinuities in the solution. The dam-break problem is a special case of the Riemann problem (3.4.1). The difference is that in the dam-break problem, the initial velocity components, u_L, u_R, v_L and v_R, are zero, whereas in the Riemann problem they are allowed to be distinct from zero. The initial setup is visualized in Figure 3.4.

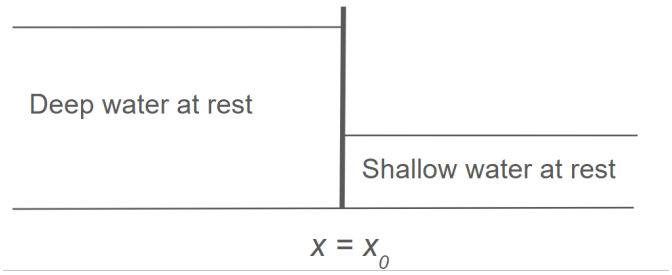

Figure 3.4: Initial conditions for the dam-break problem. An infinitely thin wall at $x = x_0$ divides two sections of water with different water levels.

We can use the shallow water equations to model the flow of water in the dam-break problem, approximately, if we assume that the wall collapses instantaneously at $t =$ [illegible]. In this project we solve both the dam-break problem and cases of the R[illegible]an problem, where the inital fluid velocity is nonzero. The results are presented in chapter 6.

3.4.2 Waves in the Riemann problem

To get a better understanding of the flow in shallow water, we provide some very short background information about the wave structures in the solution of the Riemann problem. In general, the wave structure in the solution of the Riemann problem (3.4.1) consists of three wave families separating four regions. The wave families are denoted W_1, W_2, W_3 and the regions are the spaces between the wave families, denoted by R_0, R_1, R_2 and R_3. The wave structure is illustrated in Figure 3.5.

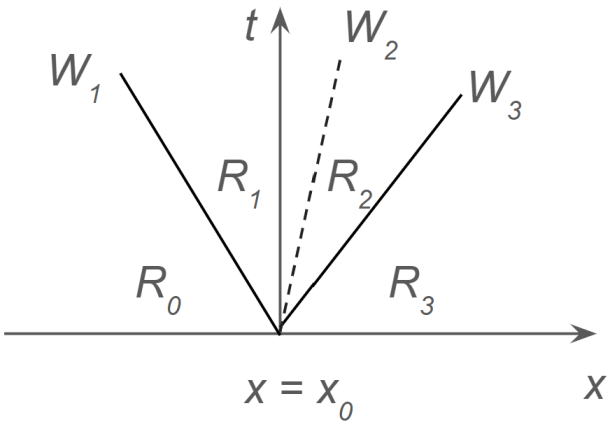

Figure 3.5: General wave structure in the solution of the Riemann problem.

From Figure 3.5 we see how the solution consists of three waves. The left and right waves are either shock waves or rarefaction waves, and correspond to the one-dimensional shallow water equations. The middle wave arises from the $y-$momentum equation in (3.4.1) and is always a shear wave. The region between the left and right wave is called the star region and is interesting, since we do not know the solution in this region. The star region is divided into two subregions R_1 and R_2. The states in the regions are (from left to right) U_L, U_{*L}, U_{*R} and U_R, where U_L and U_R are known, as these are the initial conditions. The states U_{*L} and U_{*R} are in the regions R_1 and R_2, i.e., the star region and are unknown. In the star region, we use h_* to denote the water depth and u_* to denote the velocity. We can use h_* to determine whether the left and right waves are shock waves or rarefaction waves. Since we are considering the wet bed case, we can use the following characteristic:

$$\begin{cases} \text{The left wave is a shock wave} & \text{if } h_* > h_L, \\ \text{The left wave is a rarefaction wave} & \text{if } h_* \leq h_L, \end{cases}$$

and similarly for the right wave:

$$\begin{cases} \text{The right wave is a shock wave} & \text{if } h_* > h_R, \\ \text{The right wave is a rarefaction wave} & \text{if } h_* \leq h_R. \end{cases}$$

In the solution of the Riemann problem (3.4.1) there are four possible wave patterns outcomes, which are combinations of shock waves and rarefaction waves. The left and right waves are either shock waves or rarefaction waves. The four possible wave patterns are as follows:

(a) Left rarefaction, right shock,

(b) Left shock, right rarefaction,

(c) Both left and right rarefaction,

(d) Both left and right shock.

In the example of the dam-break problem, with inital conditions as in Figure 3.4, the solution consists of a left rarefaction wave and a right shock wave. This means that the shock wave moves to the right and is characterized by a discontinuity in the solution and a high speed. Whereas, the rarefaction wave moves to the left and is characterized by a more smooth transition in the solution and a lower speed. The Riemann solver computes the flux across the interface between two cells, considering the left and right states. The numerical fluxes calculated by the Riemann solver allow for the determination of the state in the star region, which represents the solution at the interface between the two regions. This is essential for determining whether the wave is a shock or a rarefaction wave, ensuring both the stability and accuracy of the numerical scheme. In summary, Riemann solvers and numerical fluxes are crucial for solving for the states in the star region, which are then used to update the solution at each timestep.

3.5 Numerical fluxes

In this section we will study the numerical fluxes used to solve the SWE in 1D. At each cell interface, we need to solve the Riemann problem (3.4.1) to find the numerical flux. There are several numerical fluxes that can be used to solve the local Riemann problem, and we will consider some of them in this section. The fluxes we will consider are the Godunov method with an exact Riemann solver, the HLL, HLLC, Rusanov, Lax-Friedrichs, Lax-Wendroff and FORCE fluxes. All of them are later implemented and tested in the numerical experiments in chapter 6.

Godunov method with exact Riemann solver

We consider the Godunov Upwind method, which is a first-order accurate metod to solve non-linear systems of hyperbolic conservation laws [4]. In the method we solve the non-linear Riemann problem at each cell interface. The Godunov flux is given by

$$\mathbf{F}_{i+\frac{1}{2}} = \mathbf{F}(\mathbf{U}_{i+\frac{1}{2}}),$$

meaning that we solve the Riemann problem exactly to find h^* and u^*, and then use these values to compute the flux as

$$\mathbf{F}_{i+\frac{1}{2}} = \begin{bmatrix} h^*u^* \\ h^*(u^*)^2 + \frac{1}{2}g(h^*)^2 \end{bmatrix}.$$

HLL

The HLL (Harten, Lax and van Leer) approach assumes a two-wave structure of the Riemann problem. The solver is based on the data $\mathbf{U}_L := \mathbf{U}_i^n, \mathbf{U}_R := \mathbf{U}_{i+1}^n$ and fluxes $\mathbf{F}_L := \mathbf{F}(\mathbf{U}_L), \mathbf{F}_R := \mathbf{F}(\mathbf{U}_R)$. The HLL flux is given by

$$\mathbf{F}_{i+\frac{1}{2}} = \begin{cases} \mathbf{F}_L & \text{if } S_L \geq 0, \\ \mathbf{F}^{HLL} \equiv \frac{S_R\mathbf{F}_L - S_L\mathbf{F}_R + S_LS_R(\mathbf{U}_R - \mathbf{U}_L)}{S_R - S_L} & \text{if } S_L \leq 0 \leq S_R, \\ \mathbf{F}_R & \text{if } S_R \leq 0. \end{cases} \tag{3.5.1}$$

The wave speeds S_L and S_R must be estimated in some way, and one possibility is to use

$$S_L = u_L - a_Lq_L, \quad S_R = u_R + a_Rq_R,$$

where $a_L = \sqrt{gh_L}, a_R = \sqrt{gh_R}$ and $q_K (K = L, R)$ is given by

$$q_K = \begin{cases} \sqrt{\frac{1}{2}\left(\frac{(\hat{h}+h_K)\hat{h}}{h_K^2}\right)} & \text{if } \hat{h} > h_K, \\ 1 & \text{if } \hat{h} \leq h_K. \end{cases}$$

Here $\hat{h}$ is an estimate for the water depth in the star region, h_*. In the two-rarefaction Riemann Solver, the water depth h in the star region is given by

$$h_* = \frac{1}{g}\left(\frac{1}{2}(a_L + a_R) + \frac{1}{4}(u_L - u_R)\right)^2, \tag{3.5.2}$$

which is what we use in this project for $\hat{h}$ in the HLL solver. Since this is a two-wave model, it is complete for one dimensional problems, but for the augmented system of equations in two dimensions, the HLL solver is not complete, as it ignores the middle wave, the shear wave. This motivates the use of the HLLC solver, which is a modification of the HLL solver.

HLLC

The HLLC (Harten, Lax, van Leer, Contact) solver is an extension of the HLL solver, which includes the middle wave, i.e., it is a three-wave model. In addition to the wave speeds S_L and S_R, the HLLC solver also requires the speed of the middle wave S^*. We can write the HLLC numerical flux as

$$\mathbf{F}_{i+\frac{1}{2}}^{HLLC} = \begin{cases} \mathbf{F}_L & \text{if } 0 \leq S_L, \\ \mathbf{F}_{*L} & \text{if } S_L \leq 0 \leq S^*, \\ \mathbf{F}_{*R} & \text{if } S^* \leq 0 \leq S_R, \\ \mathbf{F}_R & \text{if } S_R \leq 0. \end{cases}$$

The fluxes $\mathbf{F}_{*L}$ and $\mathbf{F}_{*R}$ are given by

$$\mathbf{F}_{*L} = \mathbf{F}_L + S_L(\mathbf{U}_L - \mathbf{U}_{*L}),$$
$$\mathbf{F}_{*R} = \mathbf{F}_R + S_R(\mathbf{U}_R - \mathbf{U}_{*R}),$$

and the middle states $\mathbf{U}_{*L}$ and $\mathbf{U}_{*R}$ are given by

$$U_{*K} = h_K \left(\frac{S_K - u_K}{S_K - S_*} \right) \begin{bmatrix} 1 \\ S_* \\ \psi_K \end{bmatrix}.$$

The function ψ_K can represent either a passive scalar $\psi(x,t)$ or the velocity component $v(x,t)$ if we consider the two-dimensional shallow water equations. Mathematically $\psi(x,t)$ and $v(x,t)$ behave identically. An estimate for the middle wave speed S^* can be calculated as

$$S^* = \frac{S_L h_R(u_R - S_R) - S_R h_L(u_L - S_L)}{h_R(u_R - S_R) - h_L(u_L - S_L)},$$

where S_L and S_R are the wave speeds of the left and right waves, respectively.

Rusanov

The Rusanov flux uses the HLL framework, but with a different choice of wave speeds. To obtain the flux, we assume that an estimate S^+ for the positive wave speed is available. Then we set

$$S_L = -S^+, \quad S_R = S^+. \tag{3.5.3}$$

By substituting (3.5.3) into the $\mathbf{F}^{HLL}$ in (3.5.1), we obtain the Rusanov flux as

$$\mathbf{F}^{Rus}_{i+\frac{1}{2}} = \frac{1}{2}\left(\mathbf{F}_L + \mathbf{F}_R\right) - \frac{1}{2} S^+ \left(\mathbf{U}_R - \mathbf{U}_L\right), \tag{3.5.4}$$

where a simple estimate for the wave speed S^+ is given by

$$S^+ = \max(|S_L|, |S_R|).$$

There are some requirement for S^+ in (3.5.4) to ensure stability. It must hold that

$$S^+ \leq \frac{\Delta x}{\Delta t},$$

where $\frac{\Delta x}{\Delta t}$ is called the mesh speed.

Lax-Friedrichs

In the Lax-Friedrichs method, we use the Rusanov flux, but with a different choice of wave speed. That is, we set the wave speed S^+ as the largest possible speed, while still ensuring stability, i.e.,

$$S^+ = \frac{\Delta x}{\Delta t}. \tag{3.5.5}$$

By inserting the wave speed (3.5.5) into the Rusanov flux (3.5.4), we obtain the Lax-Friedrichs flux as

$$\mathbf{F}^{LF}_{i+\frac{1}{2}} = \frac{1}{2}\left(\mathbf{F}_L + \mathbf{F}_R\right) - \frac{1}{2}\frac{\Delta x}{\Delta t}\left(\mathbf{U}_R - \mathbf{U}_L\right),$$

where $\mathbf{F}_L = \mathbf{F}(\mathbf{U}_L)$ and $\mathbf{F}_R = \mathbf{F}(\mathbf{U}_R)$. The Lax-Friedrichs method is a centred method, which is first-order accurate.

Lax-Wendroff

There are several versions of the Lax-Wendroff flux, but in this thesis we will use the following flux:

$$\begin{aligned} \mathbf{U}^{LW}_{i+\frac{1}{2}} &= \frac{1}{2}\left(\mathbf{U}_L + \mathbf{U}_R\right) - \frac{1}{2}\frac{\Delta t}{\Delta x}\left(\mathbf{F}_R - \mathbf{F}_L\right), \\ \mathbf{F}^{LW}_{i+\frac{1}{2}} &= \mathbf{F}(\mathbf{U})^{LW}_{i+\frac{1}{2}}. \end{aligned} \tag{3.5.6}$$

The Lax-Wendroff method is a centred method, which is second-order accurate in space and time.

FORCE

The FORCE scheme (First-Order Centred) is a combination of Lax-Friedrichs and Lax-Wendroffs fluxes. The numerical flux is given by

$$\mathbf{F}^{FO}_{i+\frac{1}{2}} = \frac{1}{2}\left(\mathbf{F}^{LF}_{i+\frac{1}{2}} + \mathbf{F}^{LW}_{i+\frac{1}{2}}\right),$$

where $\mathbf{F}^{LF}_{i+\frac{1}{2}}$ is the Lax-Friedrichs flux and $\mathbf{F}^{LW}_{i+\frac{1}{2}}$ is the Lax-Wendroff flux. The FORCE scheme is first-order accurate. It is possible to extend the FORCE scheme to multiple dimensions on structured meshes by using dimensional splitting.

Chapter 4

Neural Networks and Fourier Neural Operators

So far, we have studied numerical methods for solving partial differential equations (PDEs). The Finite Volume Method (FVM), along with other numerical solvers such as the Finite Difference Method (FDM) and Finite Element Method (FEM), solves PDEs by discretizing the domain into a grid. A finer grid improves the accuracy of the solution but also increases the computational cost, creating a trade-off between accuracy and efficiency. Complex PDEs often require a fine grid to accurately capture the solution, which can be computationally expensive.

In this chapter, we introduce the use of data-driven methods for solving PDEs. The primary goal of these methods is to reduce computational costs while preserving high accuracy by learning the underlying dynamics of the solution. We will introduce the concepts of Convolutional Neural Networks (CNNs) and Fourier Neural Operators (FNOs) as part of this approach.

4.1 Convolutional Neural Networks

Convolutional Neural Networks (CNNs) are a specialized class of artificial neural networks designed to process and analyze data with a grid-like topology, such as images or time-series data represented af 2D grids. CNNs excel at extracting spatial featues from data through the use of convolutional layers, which apply learnable filters to detect patterns such as edges, shapes or textures. These layers are typically followed by pooling layers for dimensionality reduction and fully connected layers for classification or regression tasks. A key advantage of CNNs is their ability to reduce the number of parameters compared to fully connected networks by sharing weights across spatial regions, making them computationally efficient and less prone to overfitting when working with large inputs. Although CNNs are traditionally used for image recognition tasks, their architecture is adaptable for time-series analysis, especially when the data is structured spatially or sequentially.

In this project, CNNs are used to predict the solutions of the shallow water equations. The network is trained to construct a flow map, which predicts the state of the system at the next time step based on sequences of input data. Meaning the network takes sequences of input data, and predicts the corresponding output data. The output of the CNN is the solution at the next time step, effectively learning the dynamics of the SWE through the time-series data. This setup allows the model to capture both spatial and temporal dependencies in the data, leveraging the CNN's ability to learn localized featires while processing sequential information. A pro of CNN's is that they are efficient. By processing data in parallel using convolutional layers, the CNN efficiently handles large datasets without requiring excessive computational resources. Another pro is the adaptability. The model's ability to learn

from sequential data makes it adaptable for time-series predictions in dynamic systems like the shallow water equations. A con is the data representation. Representing time-series data as sequences may require preprocessing, which can introduce complexity or a potential loss of information. There can also be temporal limitations, as CNNs lack explicit mechanisms to model long-term temporal dependencies (unless extended with additional architechtures like RNNs or Transformers). We will test and evaluate the performance of the CNN model in chapter 7.

4.2 Fourier Neural Operators

In this section, we introduce the concept of Fourier Neural Operators (FNOs), a method for approximating mappings between infinite-dimensional function spaces. The theory and method described here are based on the paper [11]. The goal is to learn a mapping between two infinite dimensional spaces from a finite collection of input-output pairs. Consider the operator $G : A \to U$, which maps from an infinite-dimensional function space A to another infinite-dimensional function space U. We aim to approximate the exact operator G by constructing the map

$$G_\theta : A \mapsto U, \quad \theta \in \Theta,$$

where Θ is a finite-dimensional parameter space. Consider the functions $a \in A$ and $u \in U$. We assume access to data in the form of pointwise evaluations of these functions, i.e., we have access to the observations $\{a_j, u_j\}_{j=0}^N$, in a domain $D \subset \mathbb{R}^d$, which is bounded open set. The first step is to create $v_0(x) = P(a(x))$ by the input layer P, which is typically a shallow fully-connected neural network. The neural operator is iterative, meaning we apply several iterations of updates to obtain $v_1, v_2, \dots$ up to v_T. An update $v_t \mapsto v_{t+1}$ is defined as

$$v_{t+1}(x) := \sigma\left(W v_t(x) + \left(\mathcal{K}(a;\phi)v_t\right)(x)\right), \quad \forall x \in D \tag{4.2.1}$$

where $W : \mathbb{R}^{d_v} \to \mathbb{R}^{d_v}$ is a linear transformation, and $\sigma : \mathbb{R} \to \mathbb{R}$ is a non-linear activation function. The output $u(x) = Q(v_T(x))$ is the final update v_T transformed by the output layer Q. There are various types of operators, but the core of the Fourier Neural Operator lies in its kernel function $\mathcal{K}$. We define the Fourier integral operator $\mathcal{K}$ as

$$\left(\mathcal{K}(\phi)v_t\right)(x) := \mathcal{F}^{-1}\left(R_\phi \cdot (\mathcal{F}v_t)\right)(x), \quad \forall x \in D \tag{4.2.2}$$

where $\mathcal{F}$ is the Fourier transform, $\mathcal{F}^{-1}$ is the inverse Fourier transform, and R is the linear transformation applied on the lower Fourier modes. By transforming the data into the Fourier domain, FNOs can take advantage of the periodicity and smoothness properties of the Fourier basis, which simplifies the learning process for functions defined over continuous domains. This approach leverages the fact that differentiation with respect to time is equivalent to multiplication in the Fourier domain, distinct from the convolution theorem. CNN. The network architechture for the FNO model is illustrated in Figure 4.1.

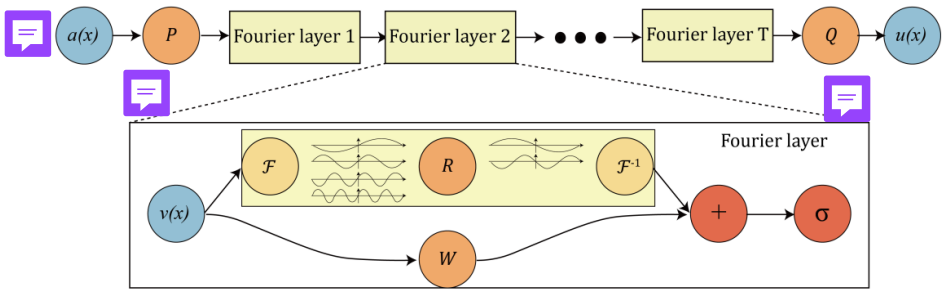

Figure 4.1: An overview of the network architecture with several Fourier layers. Illustration from [11]. Top: Overall structure with input function a, input layer P, several Fourier layers, output layer Q and output function u. Bottom: A Fourier layer consists of two parallel paths. Top is a Fourier transformation $\mathcal{F}$, a linear transformation R and an inverse Fourier transformation $\mathcal{F}^{-1}$. The bottom path consists of a linear transformation W. The parts meet and undertake an activation function σ.

From the top in Figure 4.1 we see that the network consists of an input function $a(x)$, an input layer P, several Fourier layers, an output layer Q and some output function $u(x)$. As we only have access to pointwise evaluations of $a(x)$ and $u(x)$ these are what we will use. That is, our goal is to approximate the input-output mapping:

$$\begin{bmatrix} a_0 \\ a_1 \\ \vdots \\ a_{N-1} \end{bmatrix} \rightarrow \begin{bmatrix} u_0 \\ u_1 \\ \vdots \\ u_{N-1} \end{bmatrix}.$$

In the bottom of Figure 4.1 we see the structure of a Fourier layer, which consists of two parallel paths. In the top path, the data undergoes a Fourier transform $\mathcal{F}$, decomposing it into a sum of Fourier basis functions (sines and cosines) with varying frequencies, amplitudes and phases. A linear transformation R it the applied to filter out the higher Fourier modes, as illustrated in the figure, where high-frequency components are removed. When implementing the model, we choose the number of Fourier modes to retain, depending on how much information we want to preserve. Retaining more modes keeps more information, but may also introduce more noise and oscillations. After filtering, the inverse Fourier transform $\mathcal{F}^{-1}$ is applied to reconstruct the data in its original form. The bottom path involves a linear transformation W, and the two paths merge before applying a non-linear activation function σ.

A key advantage of FNOs is that since they learn mapping between function spaces, they are not constrained by a specific grid or mesh. This allows them to transfor solutions across different grids, a process known as zero-show super-resolution. The learned operator can generalize from the coarse grid to the fine grid without needing to be retrained, making it grid-independent. This is a major advantage because it reduces the computational cost associated with fine-grid simulations. In chapter 7, we will evaluate the performance of the implemented FNO model in this context, testing its ability to maintain high accuracy when making predictions on finer grids.

Multistep prediction

We aim to develop a multi-step prediction model that can predict a specified number of time steps ahead. The input-output pairs are given as $\{a_j, u_j\}_{j=0}^N$, where the points $\{u\}_{j=0}^N$ represent the values one time step after $\{a\}_{j=0}^N$. Feeding this data into the model allows it to learn the flow map for the system. We are dealing with time series data, and the original form of the FNO can predict one time step ahead. However, for many applications, predicting multiple time steps ahead is more useful. To enable multi-step predictions, we organize the input data into sequences. The model is trained to predict the output state based on data from several previous time steps with a specified sequence length. We will conduct experiments to determine the optimal sequence length for our model.

During prediction, the model's output is added to the input as the newest data point, replacing the oldest data. This process is repeated until predictions for the desired number of future time steps are made. The process is illustrated in Figure 4.2.

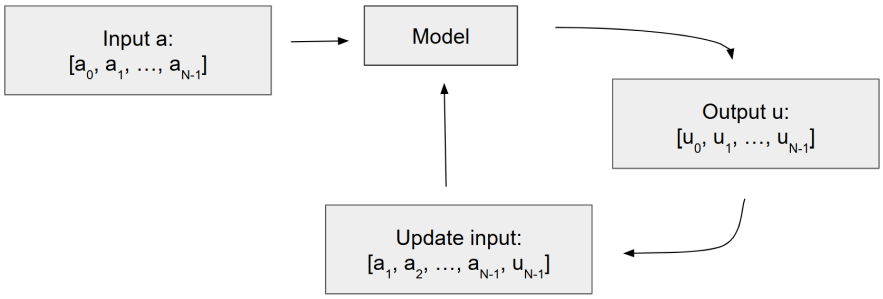

Figure 4.2: Flowchart of the multi-step prediction process.

The results of the multi-step prediction model will be presented in chapter 7.

Chapter 5

Data generation

In this chapter, we outline the process of generating the data required for the data-driven methods. This step is critical, as the quality and relevance of the data directly impact the training and performance of the models. We begin by detailing the data generation process for the 1D SWE using the exact Riemann solver. Next, we describe the approach for generating data for the 1D SWE in spherical coordinates. Finally, we present the methodology for data generation in the context of the 2D SWE.

5.1 Data generation using the FVM

In this section we clarify the data generation using our numerical solver based on the Finite Volume Method (FVM). The FVM is used to solve the SWE in 1D, in 1D with spherical coordinates, and in 2D. We specify the initial conditions, the domain, and the parameters used in the data generation process.

1D SWE with exact Riemann solver

In this section, we present how the so-called true solution is found in the code by solving the Riemann problem exactly. The true solution is found by solving the Riemann problem exact, with 200 cells, and distinguishing between the wetbed or drybed case, and also identifying the shock and rarefaction waves. First we caculate the wave speeds for the left and right states, respectively, as

$$c_L = \sqrt{gh_L}, \quad c_R = \sqrt{gh_R},$$

which are used to determine the critical water height h_{crit} as

$$h_{\text{crit}} = (u_R - u_L) - 2(c_L + c_R).$$

If either $h_L \leq 0$ or $h_R \leq 0$, we are in a drybed case. If $h_{\text{crit}} \geq 0$ it means the water depth is somehow critical, and we are in a drybed case, If none of the above conditions are met, we are in a wetbed case. Summarized:

$$\begin{cases} \text{Dry-bed case} & \text{if } h_L \leq 0, \quad h_R \leq 0 \text{ or } h_{\text{crit}} \geq 0, \\ \text{Wet-bed case} & \text{otherwise.} \end{cases}$$

For a dry bed case, we then identify where the dry is located, i.e., if the left side is dry, the right side is dry, or the middle is dry, and calculate the wave speeds accordingly. For a wet bed case, we compute the characteristics h_*

and u_* for the star region. We then identify the shock and rarefaction waves, and calculate the wave speeds for the left and right states, respectively. The process is illustrated in Figure 5.1.

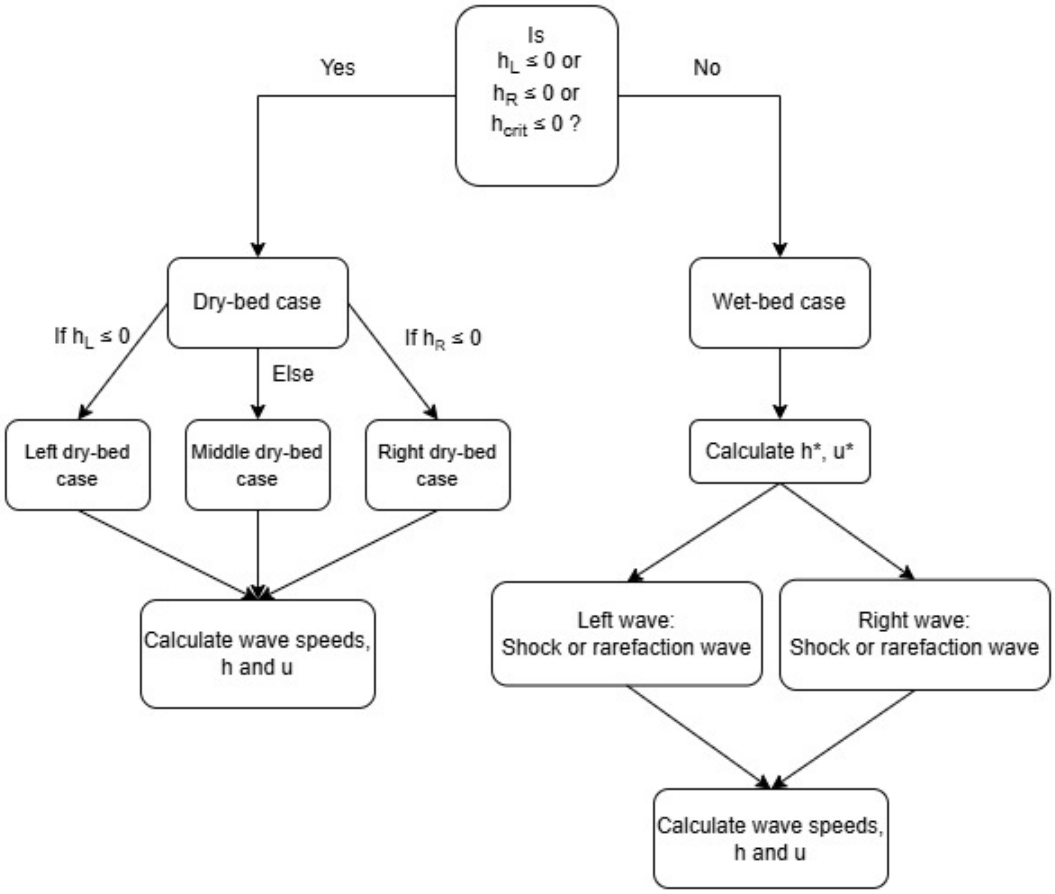

Figure 5.1: Flowchart for generating the solution.

When generating the data, we need an initial condition for the water height h and the velocity u. In this study, we use the Gaussian function as the initial condition for the water height h, that is, we use the function

$$h(x,0) = a\exp\left(\frac{-(x-\mu)^2}{2\sigma^2}\right), \tag{5.1.1}$$

where a is the amplitude of the Gaussian, μ is the mean value, and σ is the standard deviation. We are working on the domain $x \in [0,1]$ and the parameters are set to $g = 9.81$ and $\sigma = 0.$ The value of μ is varied to generate different initial conditions, as seen in Figure 5.2.

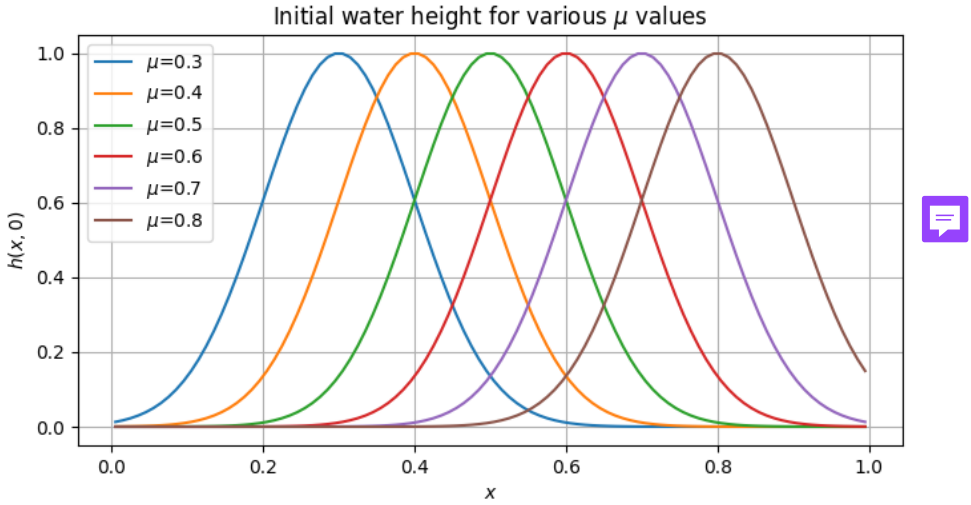

Figure 5.2: Initial conditions for the data generation.

For the initial velocity u, we set it to zero, i.e., $u(x,0) = 0$. This means that the water is initially at rest. The solver is validated by comparing the results with known test cases, such as the dam break problem. We use a CFL number of 0.9 and variable time steps. We generate the data from $t = 0.0$ to $t_{\text{end}} = 1.0$.

Truncation error

When generating data, it is essential to be aware of the truncation error. Truncation error arises from the approximation of the solution of the differential equation by the numerical method. Specifically, it is the difference between the exact solution and the numerical approximation. The critical question is: after a certain number of time steps, how significant is this error? If the error becomes too large, it raises concerms about the reliability of the generated data. Excessive truncation error could compromise the accuracy of the model trained on this data. Therefore, we must carefully evaluate and mitigate these risks to ensure the data's quality. To assess the truncation error, we generate a more accurate solution using a finer grid. This high-resolution solution serves as a reference for evaluating the numerical approximation. By comparing the high-resolution solution with the numerical solution, we gain insights into the error introduces by the approximation.

In this study, we generate a reference solution for $N = 1000$ and compare it with the solution for $N = 100$ at the final time step, $t = 1$. The results are shown in Figure 5.3.

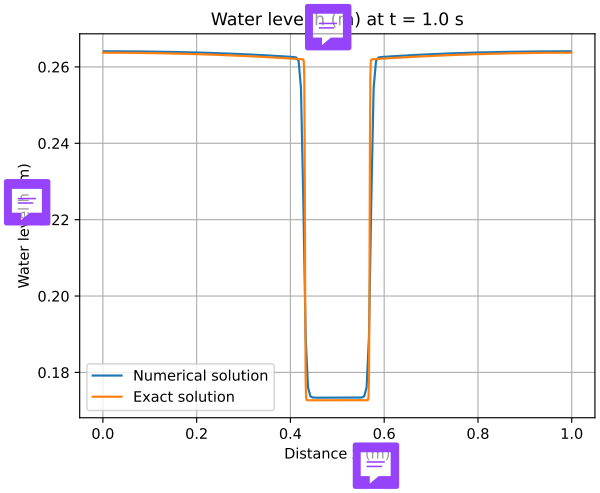

Figure 5.3: Truncation error for the 1D SWE.

From Figure 5.3, we observe that there is a small difference between the high-resolution solution and the numerical solution, as the high-resolution solution has a more discontinuous behavior. However, overall the two solutions are almost identical, indicating that the truncation error is negligible. This suggests that the data generated using the numerical solver is of high quality and can be used for training the data-driven models.

1D SWE in spherical coordinates

We also consider the spherical shallow water equations in a 1D setting, focusing on the linearized SWE on a circular domain. The length of the domain corresponds to the circumreference of the circle, $L = 2\pi$, and is discretized into $N = 500$ points. The initial condition for the water height h is specified as a Gaussian function wrapped around the circle, expressed as:

$$h(\theta, 0) = a \exp\left(\frac{-(\theta - \mu)^2}{2\sigma^2}\right), \tag{5.1.2}$$

(5.1

where the parameters are $a = 1$ and $\mu = \frac{\pi}{4}$. We generate data for varying values of σ to investigate the effect of the standard deviation on the model performance. The data is generated for $\sigma = \frac{\pi}{8}, \sigma = \frac{\pi}{16}$ and $\sigma = \frac{\pi}{32}$. The initial velocity u is set to zero, i.e., $u(\theta, 0) = 0$. The time step size is fixed and set to $\Delta t = 0.0025$. The initial conditions can be seen in Figure 5.4.

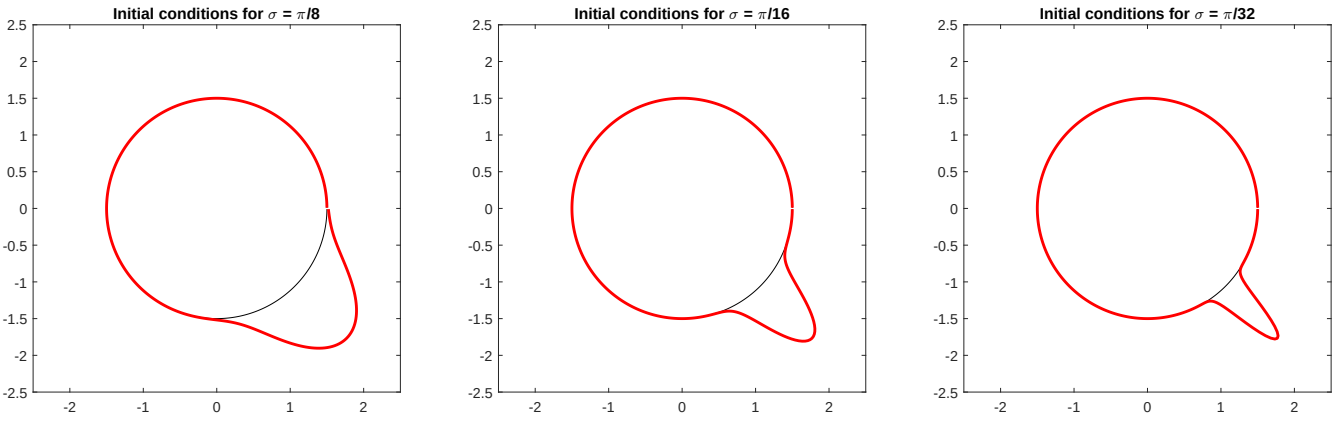

(a) $\sigma = \frac{\pi}{8}$. (b) $\sigma = \frac{\pi}{16}$. (c) $\sigma = \frac{\pi}{32}$.

Figure 5.4: Initial conditions for the 1D linearized shallow water equations in spherical coordinates for different σ values.

From Figure 5.4, we observe that the standard deviation σ affects the width of the Gaussian function. The smaller the σ, the narrower the Gaussian function, meaning the curves are steeper. This is to test the different models abilities to handle steep gradients. The data is generated from $t = 0.0$ [illegible] $t_{\text{end}} = 1.0$.

2D SWE

For the 2D SWE, we also use the Gaussian function as initial condition for the water height h, but now in two dimensions:

$$h(x, y, 0) = h_0 + a \cdot \exp\left(-\frac{(x - x_c)^2 + (y - y_c)^2}{2\sigma^2}\right),$$

where h_0 is the initial water height outside of the Gaussian, a is the amplitude of the Gaussian, (x_c, y_c) is the center of the Gaussian, and σ is the standard deviation. The domain is $x, y \in [0, 40]$ m and is discretized into N points in each direction. We use the parameters $h_0 = 1$, $a = 2$, $(x_c, y_c) = (20, 20)$, and $\sigma = 2$. The initial velocity u is set to zero, i.e., $u(x, y, 0) = 0$. The data is generated for [illegible] values of N to investigate the effect of the grid resolution on the model performance. To generate data like this also makes it possible to test the models abilities to transfer solutions to different grid resolutions. The values of N are $N = 64, N = 128$, and $N = 256$. The time step size is variable and is set to satisfy the CFL condition, where the CFL number is set to 0.9. The initial conditions can be seen in Figure 5.5.

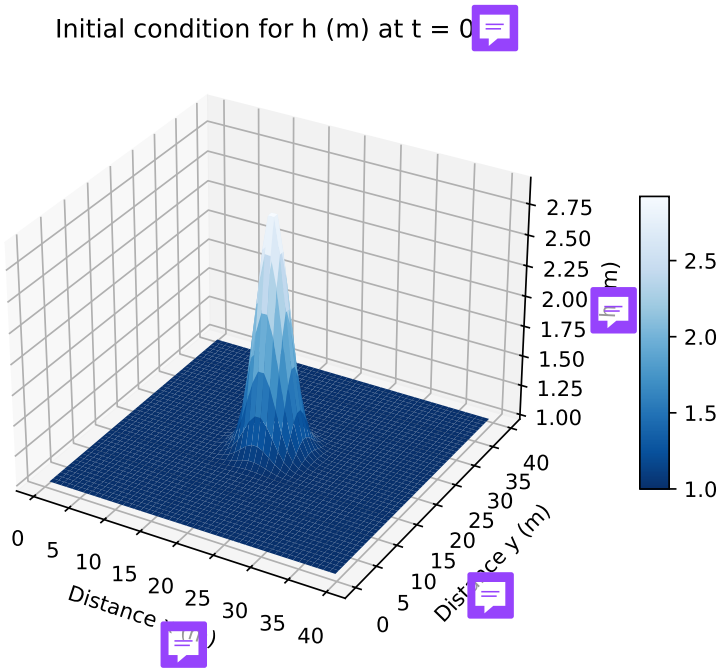

Figure 5.5: Initial condition for the 2D problem.

To generate the data we use our FVM solver to solve the 2D SWE with the initial conditions given above, which is validated by comparing the results with known test cases. The data is generated from $t = 0.0$ to $t_{\text{end}} = 10.0$. In most of our test cases the models are using the data from $t = 0.0$ to $t_{\text{end}} = 5.0$, but we need the data to be generated for a longer time period to test the models ability to make long-term predictions. Since we are making predictions beyond the data, the time step size is unknown, and we must work with a fixed time step size. For generating data for long-term predictions, we employed a constant time step size of $\Delta t = 0.025$ s. To ensure stability, the time step size must be sufficiently small. To determine Δt, we analyzed the time step sizes used in the variable step data generation. By halving the smallest observed tme step size, we obtained $\Delta t = 0.025$ s.

5.2 Data Copernicus

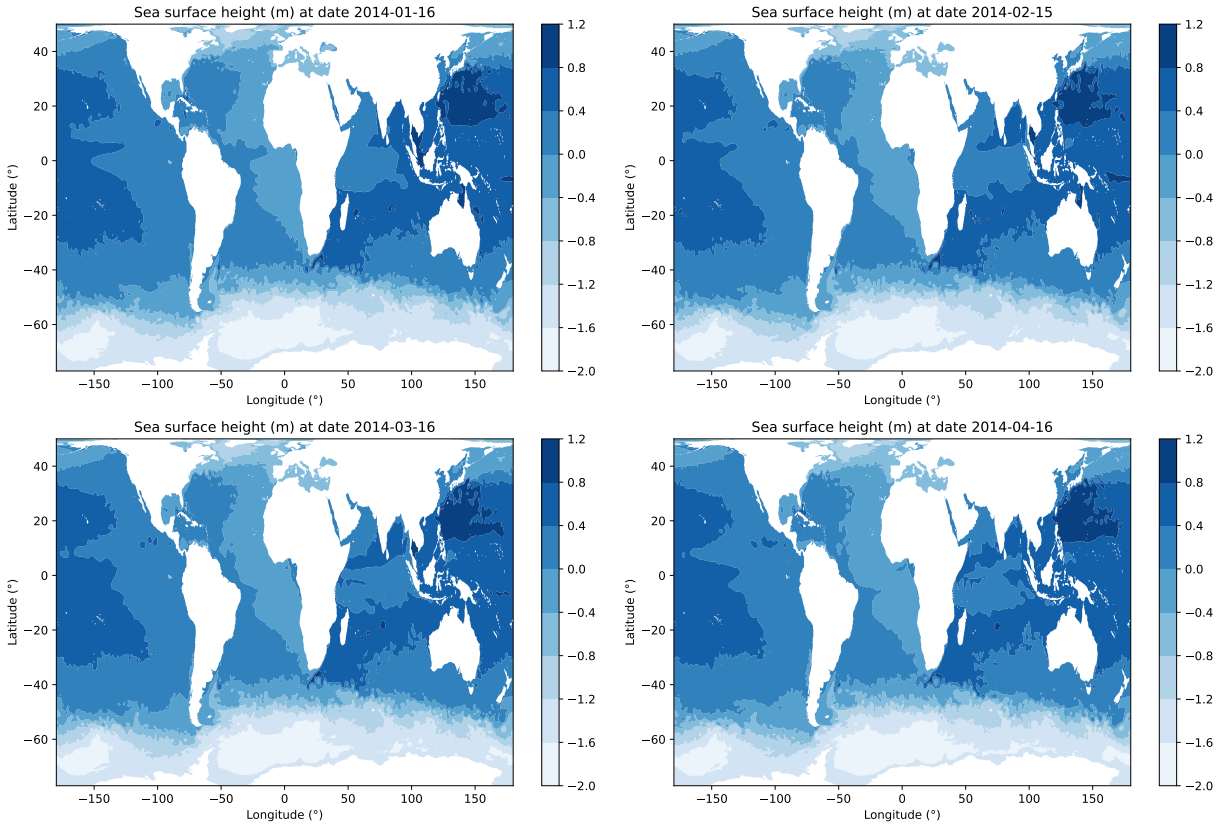

Figure 5.6: Sea surface height as the diffference from reference sea surface height for the months jan-apr 2014.

5.3 Mesh generation for the sphere

To solve the SWE on the sphere, we must use another grid, than the regular grid used in the 2D case. Hence, we use the icosahedral grid, which is a grid that approximates the sphere with triangles. The grid can be generated in different generations, depending on the level of detail we need. For each time we refine to a higher level, the number of triangles increases by a factor of four, i.e., we split each triangle into four smaller triangles. Meaning that the number of triangles is increasing drastically with each level of refinement. The grid is generated by the Github: https://github.com/siddharth-maddali/SphereMesh/tree/master and then rewritten to Python. The grid for the first 4 levels of refinement is shown in Figure 5.7. For simplicity, we will begin by considering the first level of refinement, which consists of 20 triangles. The matrix tri is a 20×3 matrix, where each row represents a triangle and the three columns represent the three vertices of the triangle. The vertices are stored in the matrix P, which is a 12×3 matrix, where each row represents a vertex and the three columns represent the x, y, and z coordinates of the vertex. The vertices are normalized to the unit sphere, i.e., the radius of the sphere is 1. The idea is now, that similar to the case in cartesian coordinates, we loop through each cell, in this case triangles, and calculate the fluxes between the cells. We must be aware of which cells/triangles are neighbors, and we must also be aware of the orientation of the triangles, i.e., the normal vector of the triangle. The normal vector is calculated by the cross product of the two vectors that span the triangle. The normal vector is then normalized to the unit sphere. The matrix tri is my Element to Vertex matrix. I also need an Element-to-Face table and a Element-to-Element table. The Element-to-Face table is used to define which edges or faces belong to each triangle. Each face of a

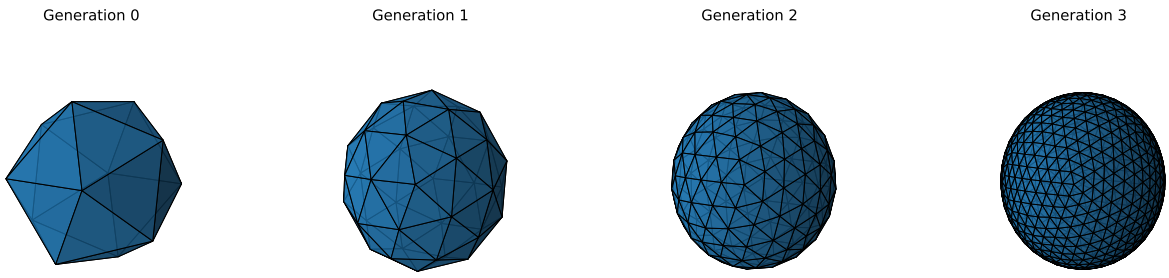

Figure 5.7: Icosahedral grid for the first 4 levels of refinement.

triangle is an edge shared between two triangles. The Element-to-Element table is used to define which triangles are neighbors. That is, it indicates which triangles share an edge. This is important when calculating the fluxes between the triangles. To construct this table we loop through each triangle and check if the edge of the triangle is shared with another triangle.

We make the FVM to solve SWE for a triangular grid on the sphere. For each triangle, we consider each face (edge). For each face we define the normal vector in terms of the spherical unit vectors $\mathbf{e}_\theta$ and $\mathbf{e}_\phi$. The spherical unit vectors at a point are:

$$\mathbf{e}_\theta = \begin{bmatrix} -\sin(\theta) \\ \cos(\theta) \\ 0 \end{bmatrix},$$
$$\mathbf{e}_\phi = \begin{bmatrix} \cos(\phi)\cos(\theta) \\ \cos(\phi)\sin(\theta) \\ -\sin(\phi) \end{bmatrix}.$$

Where $\mathbf{e}_r$ is the radial direction, going outward from the origin. $\mathbf{e}_\theta$ is the longitude direction, and $\mathbf{e}_\phi$ is the latitude direction. The unit vectors are tangensial to the sphere. We do not need to consider the radial direction, as the SWE is only in the tangential directions.

Now we have the cartesian edge vectors in tangential directions, $\mathbf{e}_0, \mathbf{e}_1, \mathbf{e}_2$.

The projection of an edge vector $\mathbf{e}_i = (e_{ix}, e_{iy}, e_{iz})$ onto $\mathbf{e}_\theta$ is:

$$\mathbf{e}_i \cdot \mathbf{e}_\theta = e_{ix}\left(-\sin\theta\cos\phi\right) + e_{iy}\left(-\sin\theta\sin\phi\right) + e_{iz}\cos\theta$$

Similarly, the projection onto $\mathbf{e}_\phi$ is:

$$\mathbf{e}_i \cdot \mathbf{e}_\phi = e_{ix}\left(-\sin\phi\right) + e_{iy}\cos\phi$$

Recall that the cross product between two vectors in 3D produces a third vector that is orthogonal to the two input vectors, i.e., the plane spanned by the two input vectors.

For a given face f of a triangle, we first calculate the Cartesian face normal $\mathbf{n}_f$ as the cross product of the two

vectors that span the face. For a given face f of a triangle, we define the normal vector $\mathbf{n}_f$ is decomposed into the spherical unit vectors as

Chapter 6

Numerical results

In this section we present the results of the numerical experiments, together with the results from the data-driven methods, including neural networks and Fourier neural operators. In chapter 6 we present the results from the finite volume method (FVM), where we have implemented the method for solving the shallow water equations in 1D and 2D and tested it on several problems. We also address the scalability issues of the finite volume method. In chapter 7 we present the results from the data-driven methods, where we have implemented neural networks and Fourier neural operators to solve the shallow water equations in 1D. We compare the results from the data-driven methods with the results from the FVM, and discuss the advantages and disadvantages of the different methods. We expand and in section 7.3 we present the results from the data-driven methods for solving the shallow water equations in 2D.

In this chapter we present the results of the numerical experiments, where we have implemented the finite volume method for solving the shallow water equations in 1D and tested it on several problems. [1] A key focus is to validate the implementation, as it will generate data for the data-driven methods, including neural networks and Fourier neural operators. To test the implementation, we have solved the 1D dam break problem, and the five test cases from Toro's book [2]. These problems are all discontinuous in either the water height h or the fluid velocity u. The idea is, that if the numerical solution can capture the discontinuities, it should be well-suited to handle smoother solutions as well. Finally, we have tested the implementation on the 2D idealised circular dam break problem, which is also from Toro's book [4]. The results from the 2D problem are compared to the results from the book to validate the implementation. Lastly, we have tested the scalability of the FVM to solve the 2D SWE, by running the 2D problem with a Gaussian initial condition for different values of N, i.e., the number of cells in each direction.

6.1 The 1D Dam Break Problem

First we solve the 1D dam break problem, with the following initial conditions:

$$h(x,0) = \begin{cases} h_L, & \text{if } x < x_0, \\ h_R, & \text{if } x > x_0, \end{cases}$$

where $x \in [0, 50], h_L = 3.5$ m, $h_R = 1.25$ m and $x_0 = 20$ m. Since it is a dam break problem the initial fluid velocity is zero, i.e., $u(x,0) =$ We solve the problem starting at $t =$ and ending at $t = 2.5$ seconds. The numerical solution to the 1D Dam Break Problem using the FVM, together with the true solution provided from the course [24], can be seen in Figure 6.1.

[1] Code and small animations can be found at github, visit `https://github.com/MelissaJessen/Shallow-Water-Equations`.

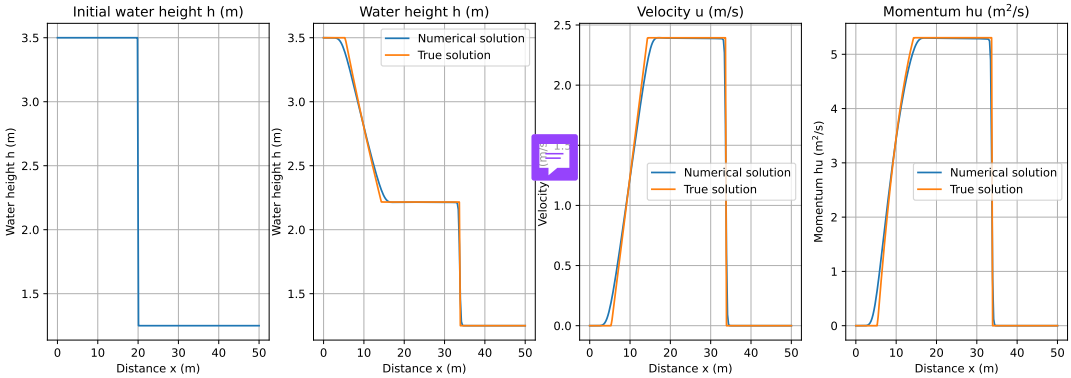

Figure 6.1: The initial water height h at $t = 0$ together with the water height, the fluid velocity u and the momentum hu after $t = 2.5$ seconds.

From Figure 6.1 we see that the numerical solution aligns well with the true solution, and successfully captures the discontinuity.

6.2 Toro test cases

We have tested the method on the five test cases for Riemann problems from Toros book [2]. The initial conditions for the five test cases are given in Table 6.1.

Test case	h_L	u_L	h_R	u_R	x_0	t_{end}
1	1.0	2.5	0.1	0.0	10.0	7.0
2	1.0	-5.0	1.0	5.0	25.0	2.5
3	1.0	0.0	0.0	0.0	20.0	4.0
4	0.0	0.0	1.0	0.0	30.0	4.0
5	0.1	-3.0	0.1	3.0	25.0	5.0

Table 6.1: Initial conditions for the five test cases.

The domain is $x \in [0, 50]$ for all test cases. The Riemann problems are chosen to test the method on different types of waves, such as shock waves and rarefaction waves. To solve the test cases we have used the following fluxes:

1. Godunov method with exact Riemann solver,
2. Lax-Friedrich flux,
3. Lax-Wendroff flux,
4. FORCE flux,
5. HLL flux,

Test case 1

The initial conditions for test case 1 are given in Figure 6.2 and the final solutions after $t = 7.0$ seconds are given in Figure 6.3. In test case 1, we observe a right shock wave and a left rarefaction wave.

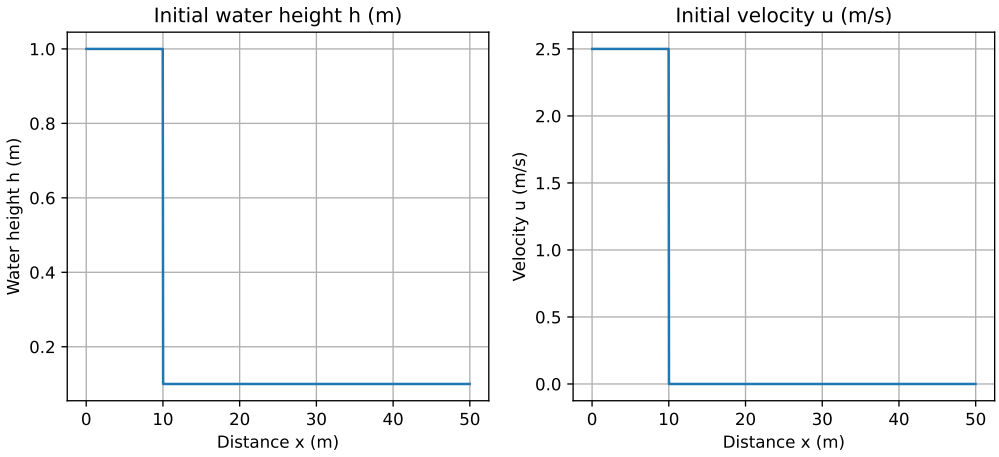

Figure 6.2: Initial conditions for the test case.

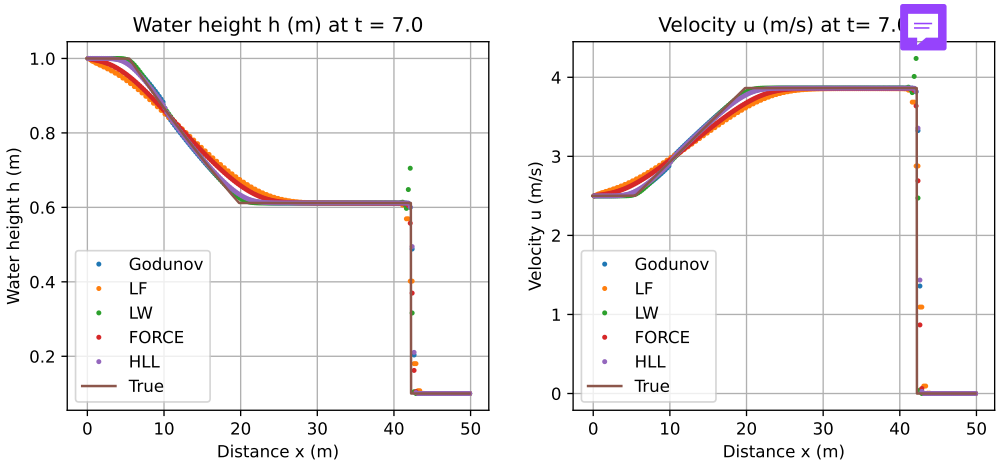

Figure 6.3: Final solution for the test case.

For this test case all the fluxes work well, but there are minor differences in the solution, which can be seen in Figure 6.3. We also see that Lax-Wendroff flux has some oscillations in the solution, which is not present in the other fluxes.

Test case 2

The initial conditions for test case 2 are illustrated in Figure 6.4.

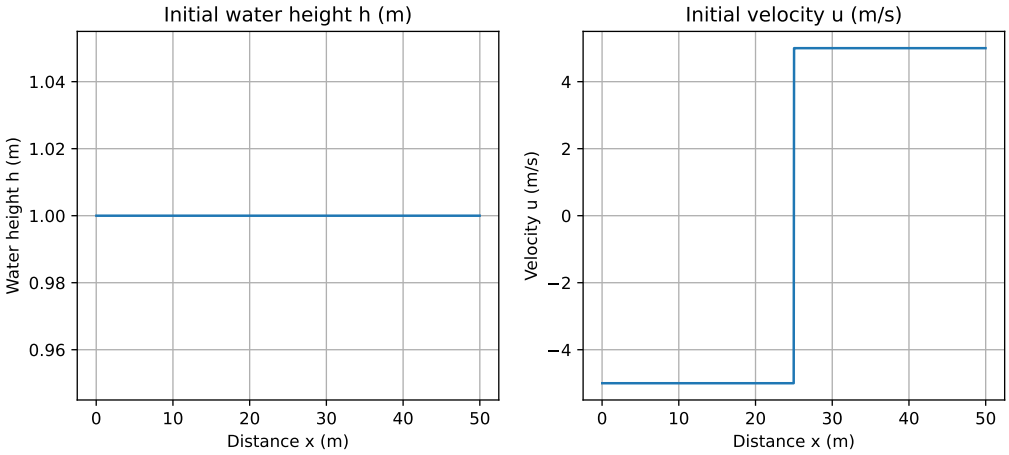

Figure 6.4: Initial conditions for the test case.

In test case 2 we have two rarefaction waves, one on the left side and one on the right side. As they are travelling in opposite directions (away from each other), there will be created a nearly dry bed in the middle of the domain. Many methods have difficulties with this test case as they may compute a negative water height. For these experiments we were able to get close to the true solution, using Lax-Friedrich flux, FORCE flux and HLL flux. The final solutions after $t = 2.5$ seconds are illustrated in Figure 6.5.

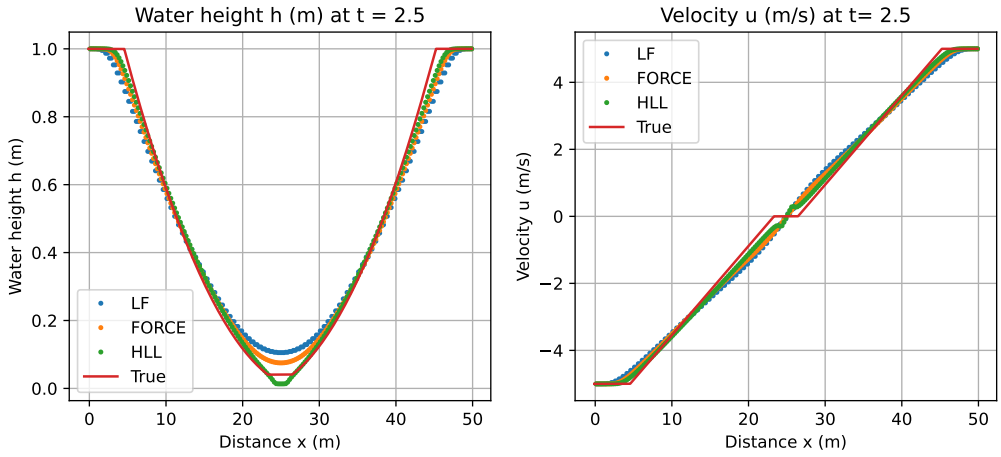

Figure 6.5: Final solution for the test case.

For the fluxes, Godunov method with exact Riemann solver, and Lax-Wendroff, it was not possible to get an acceptable solution.

Test case 3

The initial conditions for test case 3 are given in Figure 6.6, and the final solutions after $t = 4.0$ seconds are given in Figure 6.7.

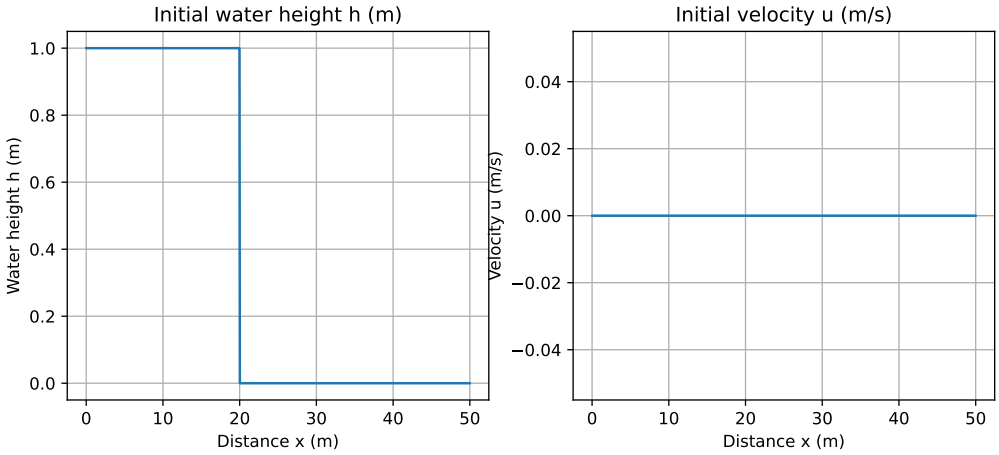

Figure 6.6: Initial conditions for the test case.

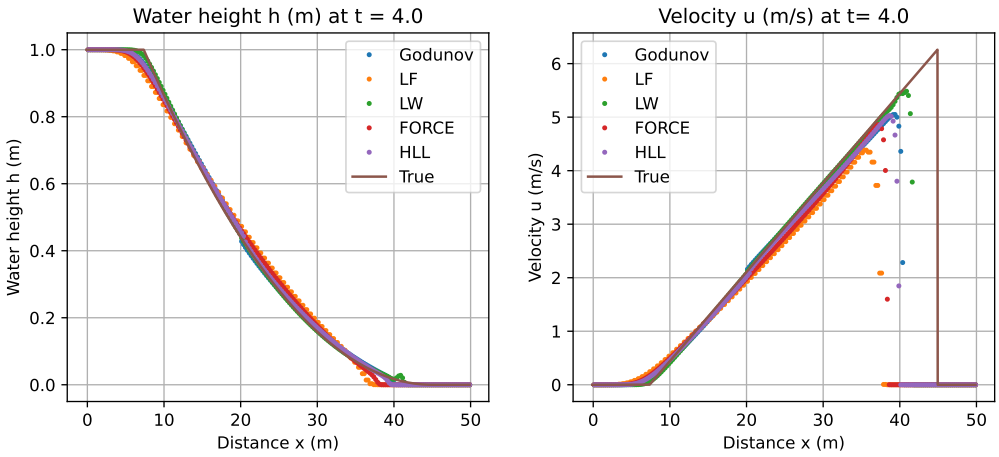

Figure 6.7: Final solution for the test case.

To solve case 3, with the FVM we must add a small amount to h_R, since the code does not handle $h_R = 0$ well. We set $h_R = 0.00005$ to solve it numerically, but the true solution is for $h_R = 0$. By running experiments with different values of h_R, we see that the solution converges to the true solution as h_R approaches 0. The solution consists of a left rarefaction wave. From Figure 6.7 we see that when it comes to predicting the velocity, there are some differences in how the different fluxes perform.

Test case 4

The initial conditions for test case 4 are given in Figure 6.8, and the final solutions after $t = 4.0$ seconds are given in Figure 6.9.

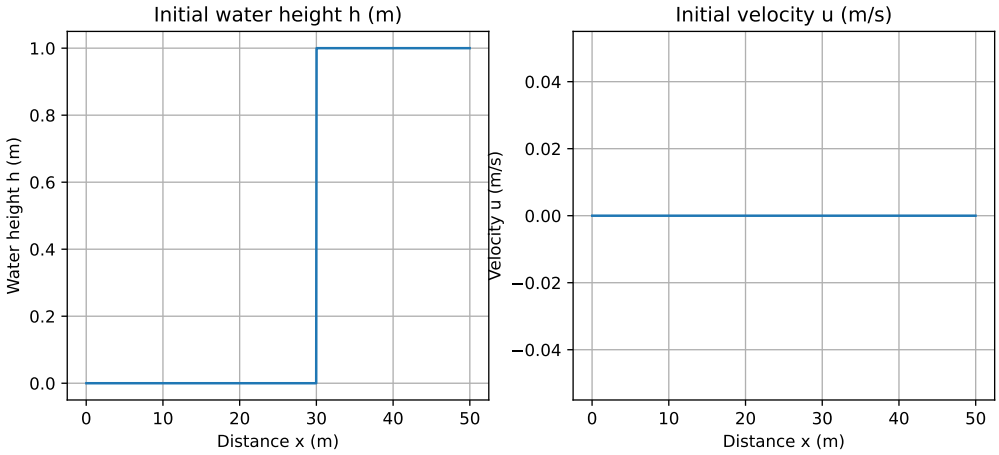

Figure 6.8: Initial conditions for the test case.

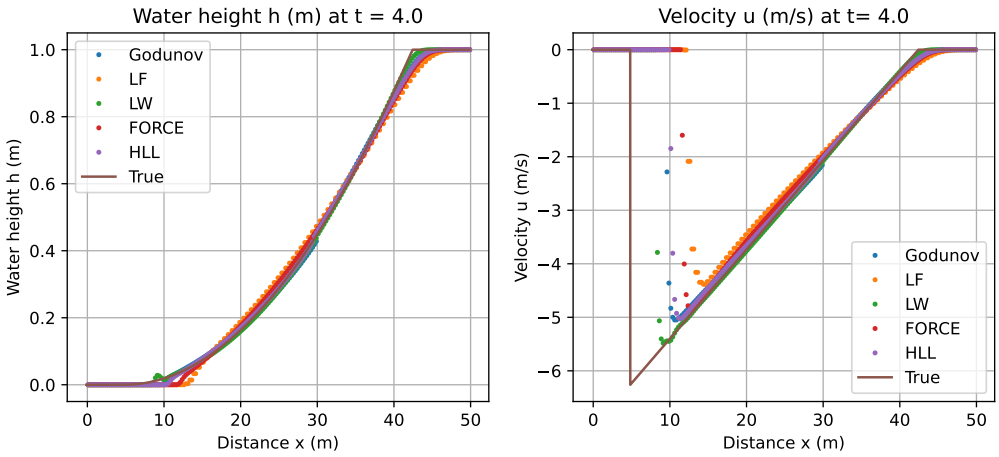

Figure 6.9: Final solution for the test case.

In case 4 we face the same challenges as in case 3. We set $h_L = 0.00005$, and the solution converges to the true solution as h_L approaches 0. This test case is symmetric to test case 3, and the solution consists of a right rarefaction wave. The case is included to test if the results are as expected. As in test case 4, we observe differences in the fluxes performance.

Test case 5

The initial conditions for test case 5 are given in Figure 6.10, and the final solutions after $t = 5.0$ seconds are given in Figure 6.11.

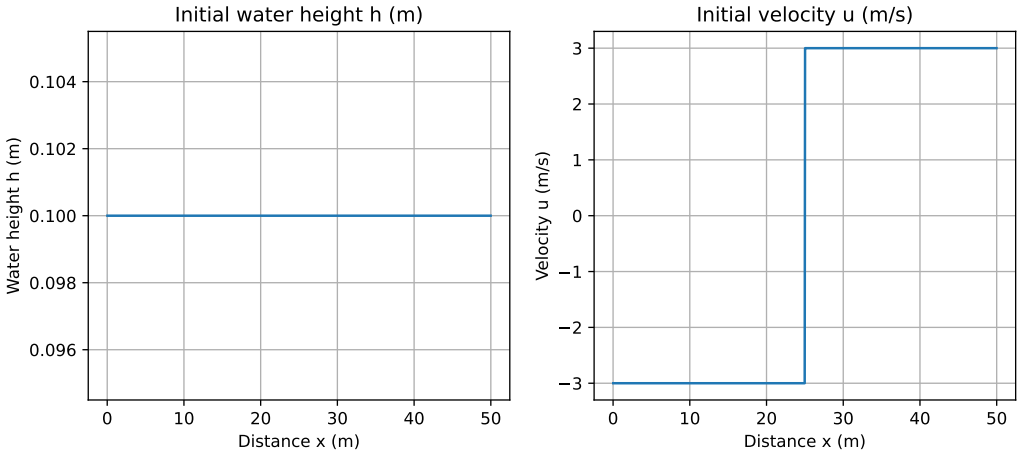

Figure 6.10: Initial conditions for the test case.

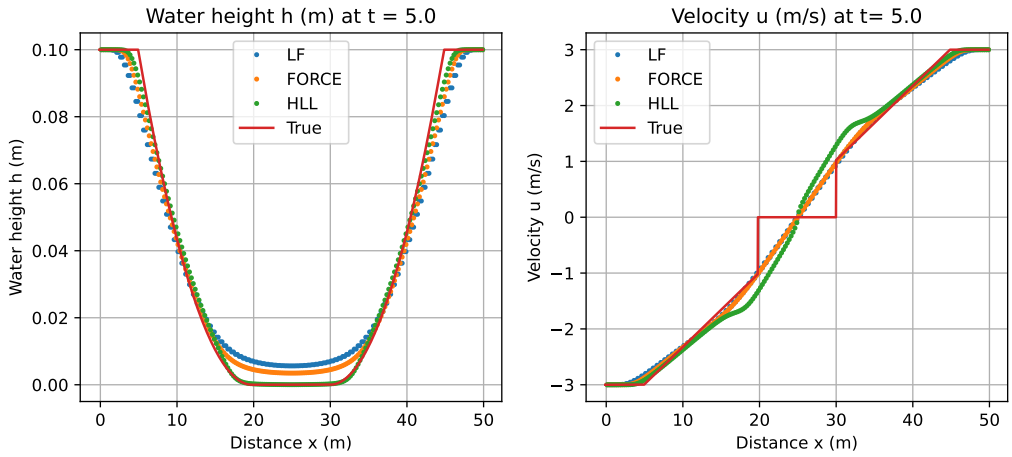

Figure 6.11: Final solution for the test case.

From Figure 6.11 we see that the numerical solutions for the velocity v at $t = 5.0$ are smooth, where the true solution is discontinuous. In this test case there are also challenges with some of the fluxes due to the generation of a dry-bed region. The fluxes that are not able to solve this case are Godunov method with exact Riemann solver and Lax-Wendroff flux, the same as in test case 2. The solution consists of two rarefaction waves, one on the left side and one on the right side, and a dry-bed region in the middle.

To get an overview of which fluxes that were able to produce solutions for the test cases, consider Table 6.2. The table shows which fluxes that were able to produce a solution for the test cases.

Test case	Godunov	LF	LW	FORCE	HLL
1	✓	✓	✓	✓	✓
2	×	✓	×	✓	✓
3	✓	✓	✓	✓	✓
4	✓	✓	✓	✓	✓
5	×	✓	×	✓	✓

Table 6.2: Overview of which fluxes that were able to produce solutions for the test cases.

Note, that as we see in the results, there are still differences in the solutions accuracy between the fluxes that were able to solve the test cases.

6.3 2D idealised Circular Dam Break Problem

We now proceed to the 2D case, focusing on an idealised circular dam break problem over a horizontal bottom. This problem is also from Toro's book [4]. We assume there is an infinitely thin circular wall at radius $R = 2.5$ m is a square domain of size 40×4 th centre at $(x_c, y_c) = (20, 2$ The initial conditions are

$$h(x, y, 0) = \begin{cases} 2.5\ m, & \text{if } \sqrt{(x - x_c)^2 + (y - y_c)^2} \leq R, \\ 0.5\ m, & \text{otherwise,} \end{cases}$$
$$u(x, y, 0) = 0,$$
$$v(x, y, 0) = 0.$$

We use a mesh of size 200×200. The results after $t = 0.0, 0.4, 0.7$ and 1.4 seconds are given in Figure 6.12.

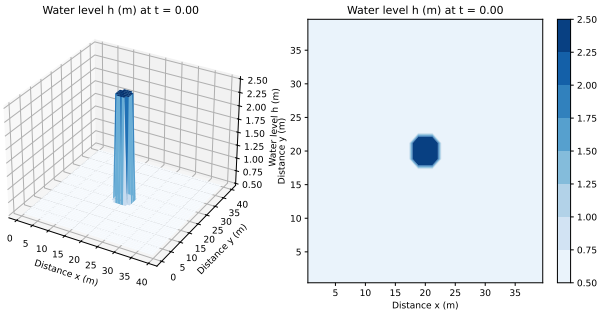

(a) 2D dam break problem after $t = 0$.

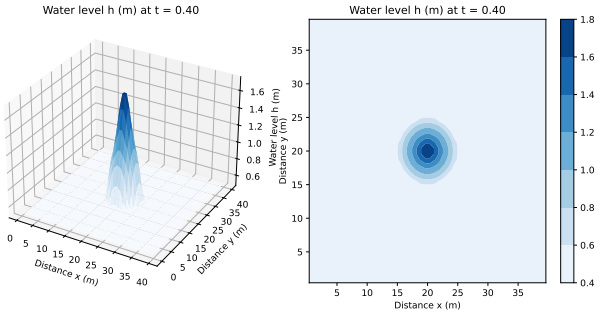

(b) 2D dam break problem after $t = 0.4$.

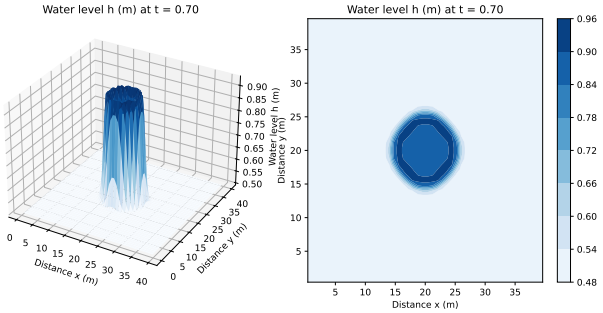

(c) 2D dam break problem after $t = 0.7$.

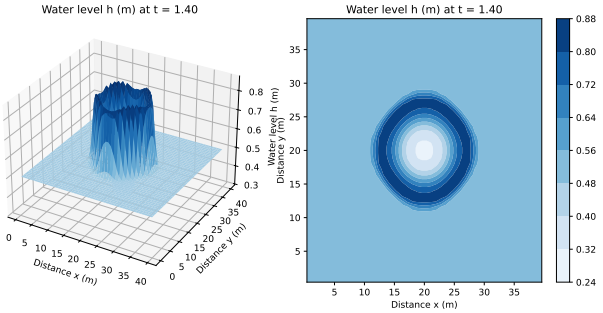

(d) 2D dam break problem after $t = 1.4$.

Figure 6.12: Snapshots of the 2D dam break problem at different times.

By comparing Figure 6.12 with the results from the book by Toro [4], and see that the numerical solution aligns well with the true solution from the book.

6.4 Scalability

To test the scalability of the FVM to solve the 2D SWE, we have run the 2D problem with a Gaussian initial condition, for different values of N, i.e., the number of cells in each direction. Numerical methods are good as they can be more or less as accurate as we want them to be, but the computational cost increases with the number of cells.

N	16	32	64	128	256
Time (s)	0.37	2.73	19.90	170.08	4205.45

Table 6.3: Running time for the FVM to solve 2D SWE for different values of N.

The run time dependent of the number of cells N is illustrated in Table 6.3.

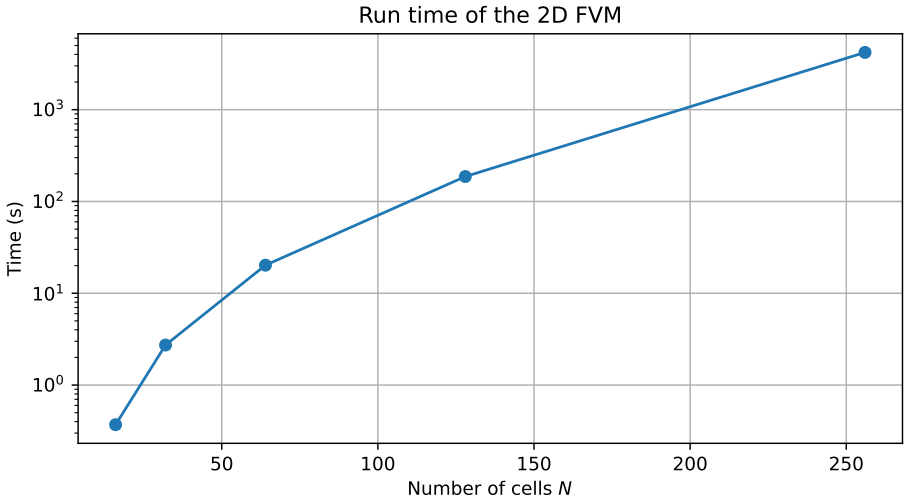

Figure 6.13: Scalability of the FVM to solve the 2D SWE.

From Table 6.3 and Figure 6.13 we see that the run time increases drastically with the number of cells N. This is expected, as the number of cells increases, the number of computations increases as well. This also means that the computational cost increases with the number of cells, and the method is not scalable for large values of N. Ultimately, if we want to model floods or tsunamis for the real world, we need a scalable method. This is also some of the motivation for using data-driven methods, as we will investigate if they can be more scalable.

Chapter 7

Data-driven results

In this section we present the results of the data-driven models, the Convolutional Neural Network (CNN) and the Fourier Neural Operator (FNO), for solving the shallow water equations. We analyse three main cases:

1. 1D SWE with Gaussian initial conditions.
2. 1D linearized SWE in spherical coordinates.
3. 2D SWE with Gaussian initial conditions.

In each case, we evaluate the performance of the CNN and FNO models in terms of Mean Squared Error (MSE), Mean Absolute Error (MAE), training time and prediction time. In addition, we analyze the models' predictions for various initial conditions and their ability to generalize to unseen data. We also explore their capability to transfer solution aross different grid resolutions, such as transitioning from a coarse grid to a fine grid. Finally, we examine the models' long-term predictive performance, assessing how well they maintain accuracy over extended time steps.

In chapter 6, we presented the results of discontinuous test cases, operating under the premise that a solver capable of handling discontinuous solutions should also perform well with smooth solutions. In this chapter, we shift our focus to evaluating the performance of data-driven models under smooth initial conditions, as these are more representative of real-world scenarios.

7.1 1D SWE with Gaussian initial conditions

In this section, we consider the 1D shallow water equations with Gaussian initial conditions, where the data is generated as described in section 5.1. The initial condition for the water height h is given in (5.1.1) and illustrated in Figure 7.1.

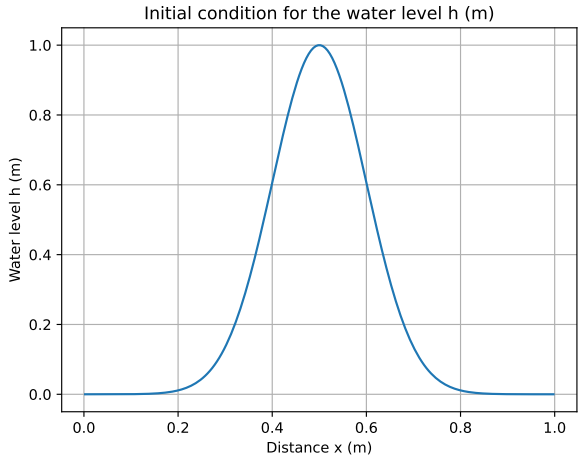

Figure 7.1: The initial conditions for water level h in the 1D SWE is a Gaussian function.

To get an overview of how the solutions evolve, we have plotted the numerical solution in the $x-t$-plane, shown in Figure 7.2, in both a contour plot and a 3D plot.

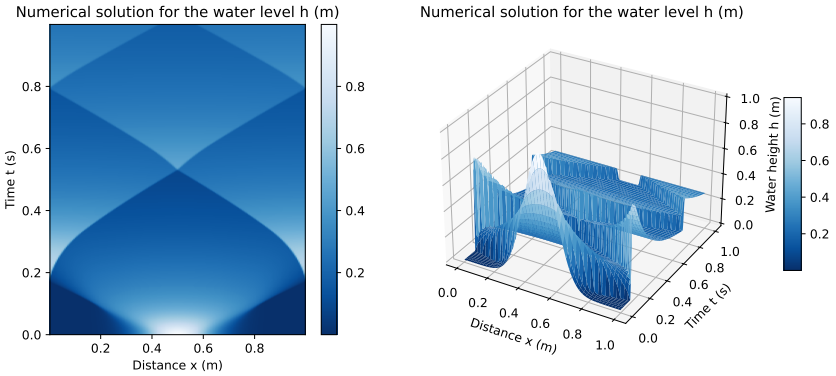

Figure 7.2: Numerical solution of the 1D SWE from $t = 0$ to $t = 1$.

In Figure 7.2, we see how the solution evolves over time. The 3d plot provides an overview of the solution, whereas the contour plot offers a more detailed view of the water level. From the contour plot, we observe that even though the initial condition is smooth, the solution develops discontinuities over time, represented by the lines in the plot. This behavior is typical for the shallow water equations, where the solution can become discontinuous due to the formation of shock waves.

CNN Model

In the convolutional neural network, we train the model using the data generated by the numerical solution of the shallow water equations. The model uses the data from the numerical solution to predict the solution at the next time step. Meaning that the input and output data are the same, but shifted one time step. This way, the

model is supposed to learn the flowmap. The model takes input with multiple channels and applies a series of 1D convolutional layers to extract spatial features. The model uses three convolutional layers with ReLU activation functions. The final convolutional layer reduces the output to a single channel, and a fully connected layer maps the processed features to the output. The model has been trained using the Adam optimizer with a learning rate of 0.001 and a batch size of 32. The criteria is to minimize the mean squared error (MSE). The model is trained on the first 60% of the data, validated on the next 20%, and tested on the last 20%. The training and validation loss for the CNN model is shown in Figure 7.3.

Figure 7.3: Training and validation loss (MSE) for the CNN model.

In Figure 7.3, we see that the training and validation loss decrease over the epochs, demonstrating that the model is learning the dynamics of the solution. However, while the training loss continues to decrease, the validation loss has largely stabilized. This indicates that further training is unlikely to improve the model's performance and may lead to overfitting. Additionally, we assess the accuracy of the model's predictions by examining the error, as shown in Figure 7.4.

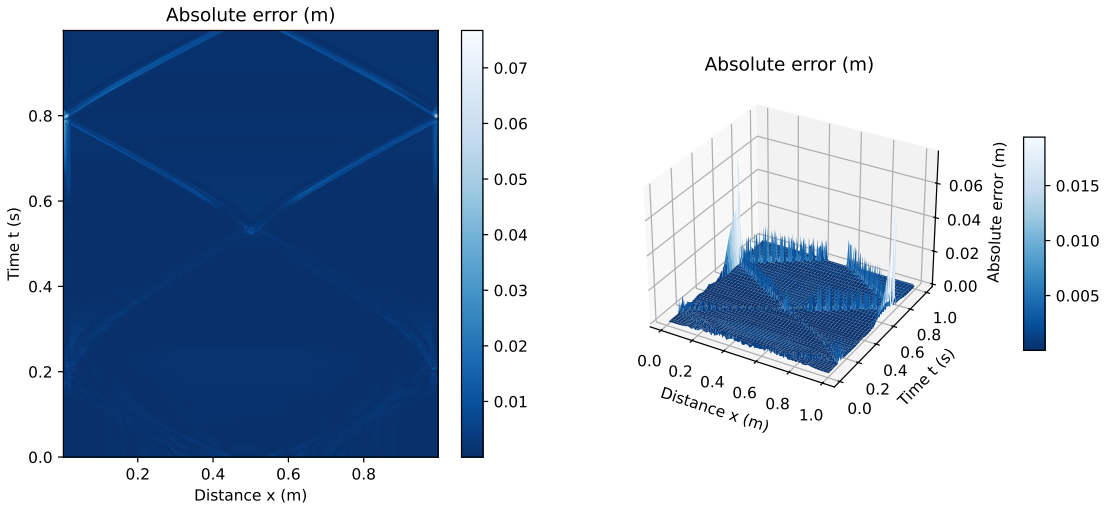

Figure 7.4: Error plot for the predictions for the CNN model.

In Figure 7.4, the largest errors are observed in regions where the solution exhibits discontinuities, which is expected as the model struggles to accurately predict in these areas. We also see that, the error tends to increase over time, reflecting the model's limitations when extrapolating beyond the training data. To gain deeper insight into the model's performance, we examine its predictions at specific time steps, as shown in Figure 7.5.

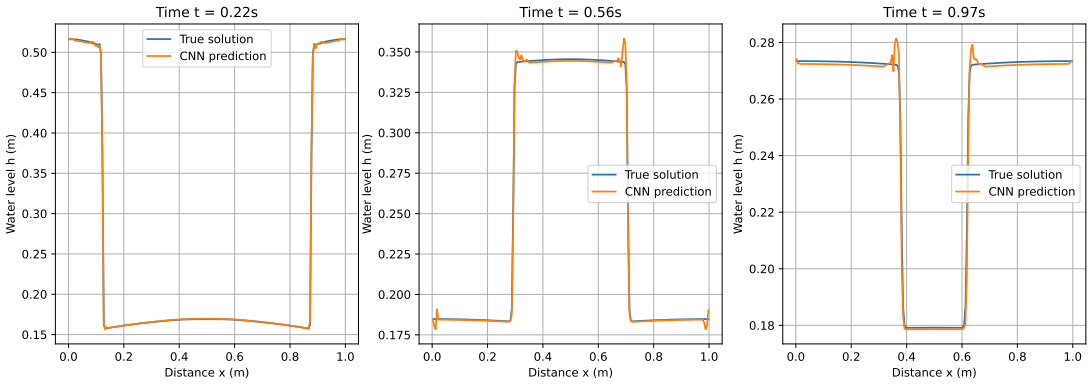

Figure 7.5: Predictions for the CNN model for some given time steps.

From Figure 7.5, we observe that the CNN model overall captures the dynamics of the solution, but struggles to predict the sharp edges. This is expecially illustrated in the prediction at $t = 0.9$ s, where we observe oscillations in the solution that are not present in the true solution.

FNO Model

We define a FNO model, which consists of an input channel, 64 hidden channels and an output channel. We use a Fourier basis with 16 modes and a batch size of 32. The model is trained using the Adam optimizer with a learning

rate of 0.001 and the critera is to minimize the mean squared error (MSE). We use the same train/validation/test split as for the CNN model. The training and validation loss for the FNO model is shown in Figure 7.6.

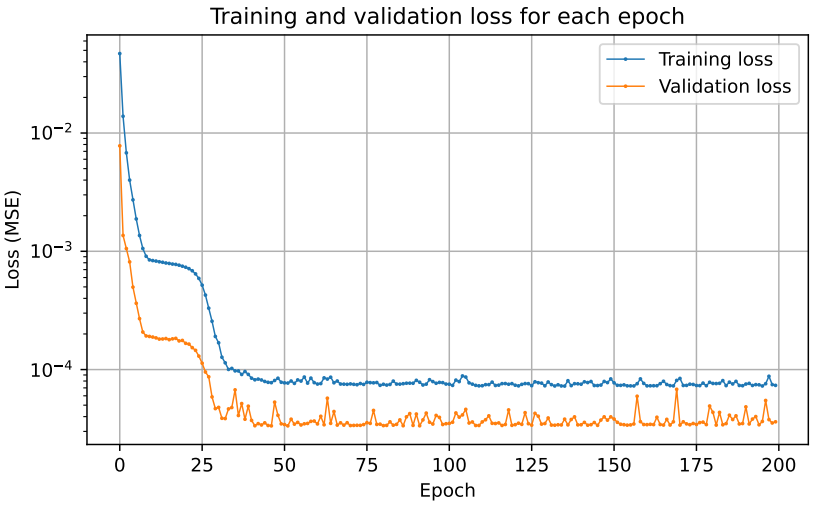

Figure 7.6: Training and validation loss for the FNO model.

From Figure 7.6, we see that the training and validation loss decrease over the epochs, indicating that the model is learning the dynamics of the solution. As with the CNN model, the validation loss has largely stabilized, suggesting that further training is unlikely to improve the model's performance. To see how the errors are distributed in the solution, we plot the error in Figure 7.7.

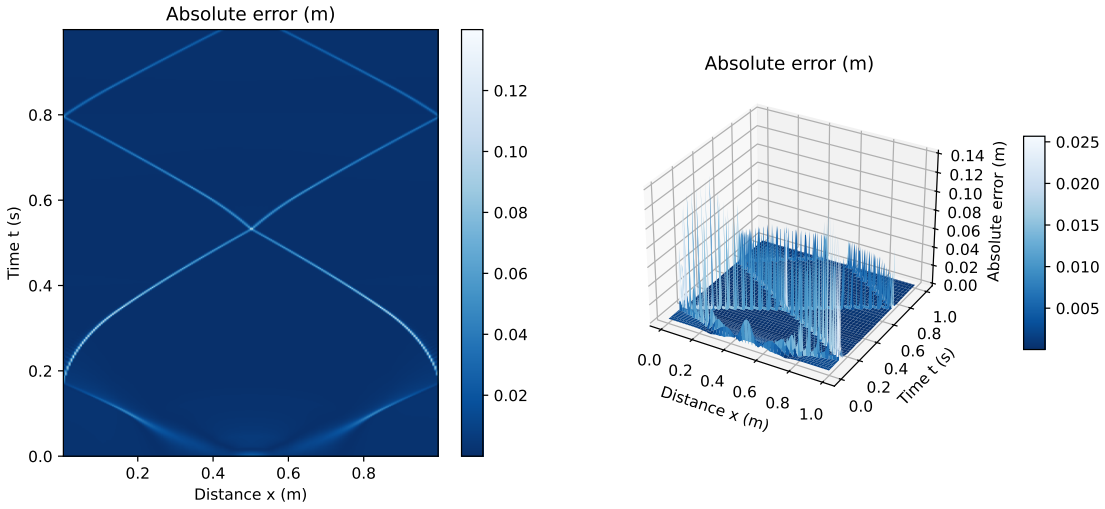

Figure 7.7: Error plot for the predictions for the FNO model.

In Figure 7.7, we see more or less the same error distribution as for the CNN model, with the largest errors at the discontinuities, and the error increasing over time. To get an overview of the performance of the model, we consider the predictions for some given time steps, shown in Figure 7.8.

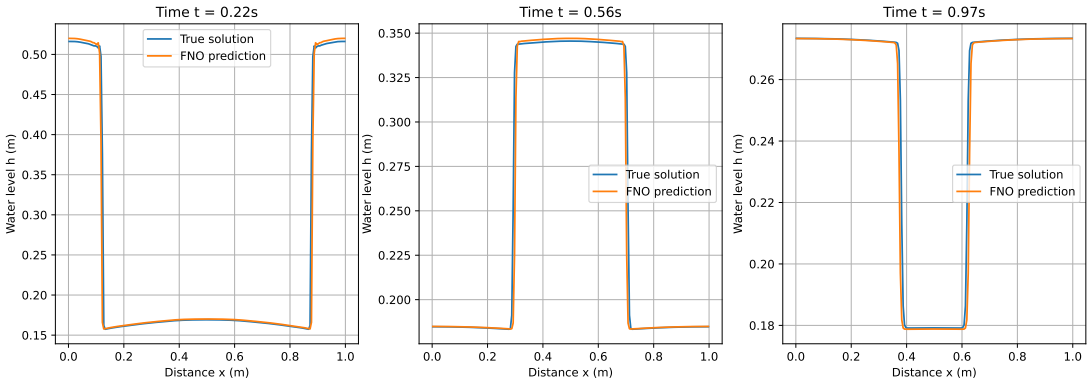

Figure 7.8: Predictions for the FNO model for some given time steps.

From Figure 7.8, we see that the FNO model overall provides a smooth and accurate prediction.

New initial condition

To evaluate the models' ability to generalize to unseen initial conditions, we introduce a new initial condition for the water height h. This new condition retains the Gaussian form described in (5.1.1), but with a different mean parameter μ. Specifically, μ is set to $\mu =$ shifting the initial condition to the left. The new initial condition is illustrated in Figure 7.9.

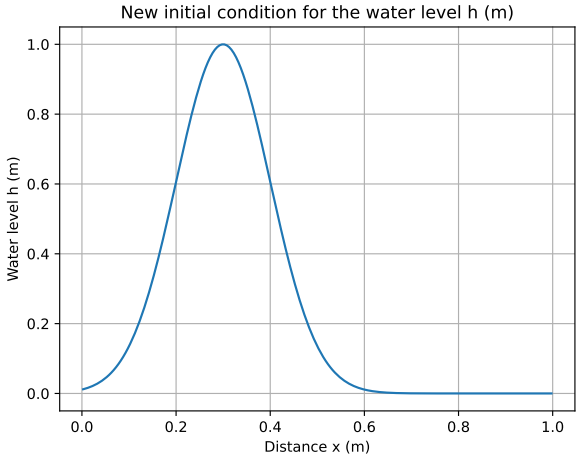

Figure 7.9: New initial condition for the 1D SWE with a Gaussian function.

The performance of the CNN and FNO models for this new initial condition is summarized in Table 7.1.

Comparison

To compare the performance of the CNN and FNO models, we consider the MSE and MAE for the predictions of the 1D SWE with Gaussian initial conditions. The reason we consider both MSE and MAE is that the MSE is more sensitive to outliers, while the MAE provides a more general overview of the error. The results are summarized in Table 7.1.

Model	Gauss initial condition				New initial condition		
	Epochs	MSE	MAE	Training time (s)	MSE	MAE	Prediction time (s)
CNN	500	6.38e-06	1.25e-03	186.52	1.98e-05	1.86e-03	0.16
FNO	200	1.99e-05	1.37e-03	187.82	1.42e-05	1.39e-03	0.59

Table 7.1: Test loss in terms of MSE and MAE, and time for training the models for the 2D SWE.

From Table 7.1, we see that both models has a low MSE and MAE for the Gaussian initial conditions, and hence perform well. We note that the training time for the FNO model is significantly higher than for the CNN model.

7.2 1D linearized SWE in Spherical Coordinates

In this section, we consider the linearized shallow water equations in spherical coordinates in a 1D setting on a circular domain. The length of the domain corresponds to the circumreference of the circle, $L = 2\pi$, and is discretized into $N = 500$ points. The initial conditions is specified as a Gaussian function wrapped around the circle as given in (5.1.2). We use the middle value of σ, i.e., $\sigma = \frac{\pi}{16}$, to generate the initial conditions. The initial conditions can be seen in Figure 7.10.

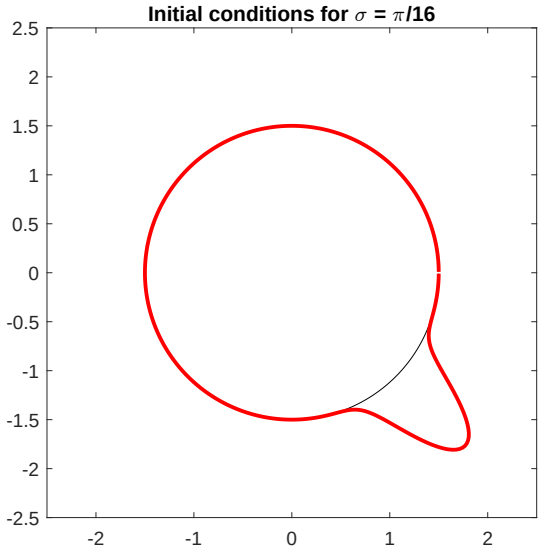

Figure 7.10: Initial conditions for the 1D linearized shallow water equations in spherical coordinates.

To get an overview of how the solution evolves, we have plotted the numerical solution in the θ, t-plane, shown in Figure 7.11.

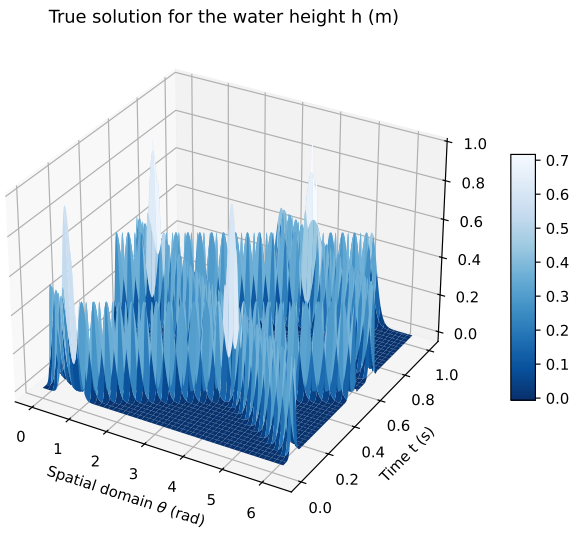

Figure 7.11: Numerical solution of the spherical shallow water equations in 1D in the $\theta, t-$space.

In Figure 7.11, we see that the solution has some steep descents, and it is interesting to see how the data-driven models handle these sharp edges.

CNN Model

Ww define and train a CNN model to solve the 1D linearized shallow water equations (LSWE) in spherical coordinates. The CNN model is trained on the data from $t = 0$ to $t = 0.6$ s, validated on the data from $t = 0.6$ to $t = 0.8$, and tested on the data from $t = 0.8$ to $t = 1.0$ s. The training and validation loss is shown in Figure 7.12.

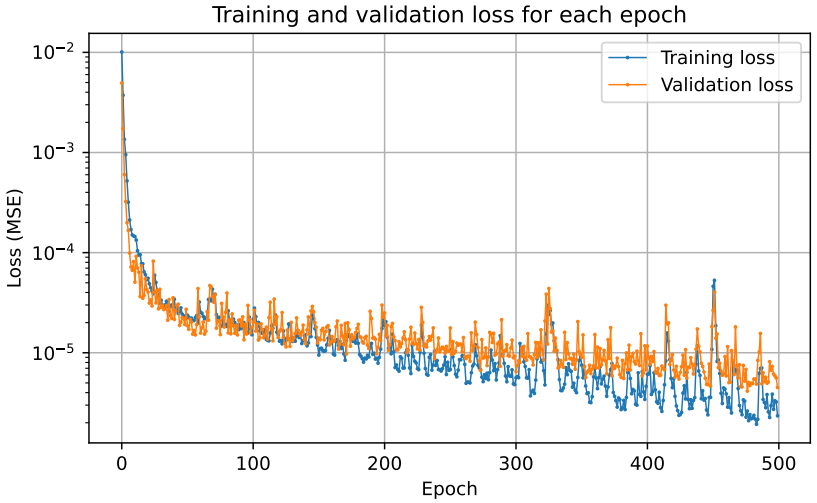

Figure 7.12: Training and validation loss for the CNN model for the 1D spherical LSWE.

To see how the model performs, we consider the error plots in Figure 7.13.

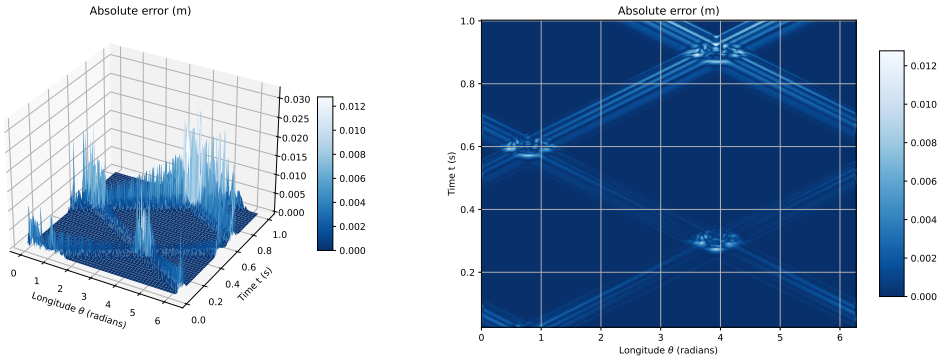

Figure 7.13: Error plots for the predictions of the CNN model for solving the 1D linearized spherical SWE.

In Figure 7.13, we see that errors are largest at the sharp edges of the solution, which is expected as the solution tends to be discontinuous. The predictions for some given time steps are shown in Figure 7.14.

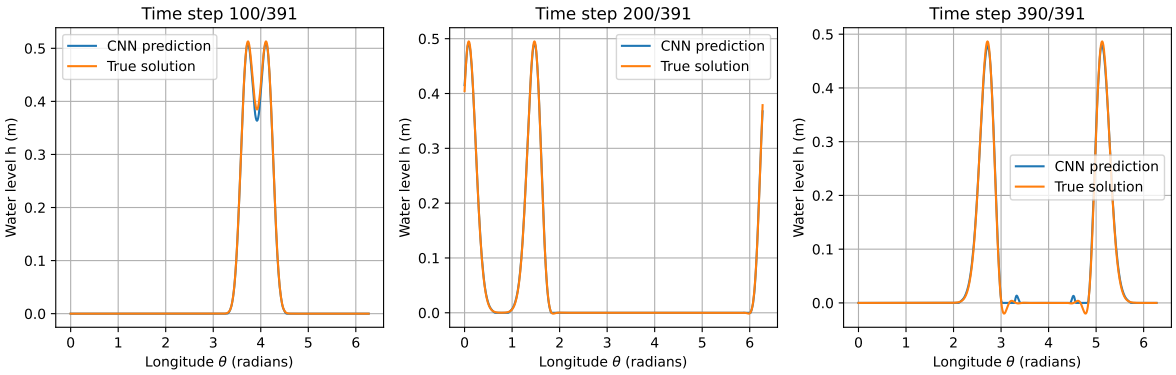

Figure 7.14: Predictions for the spherical shallow water equations in 1D using the CNN model for some given time steps.

From Figure 7.14, we see that the predictions capture the waves, but have some over- or underestimations at the top or bottom of the waves.

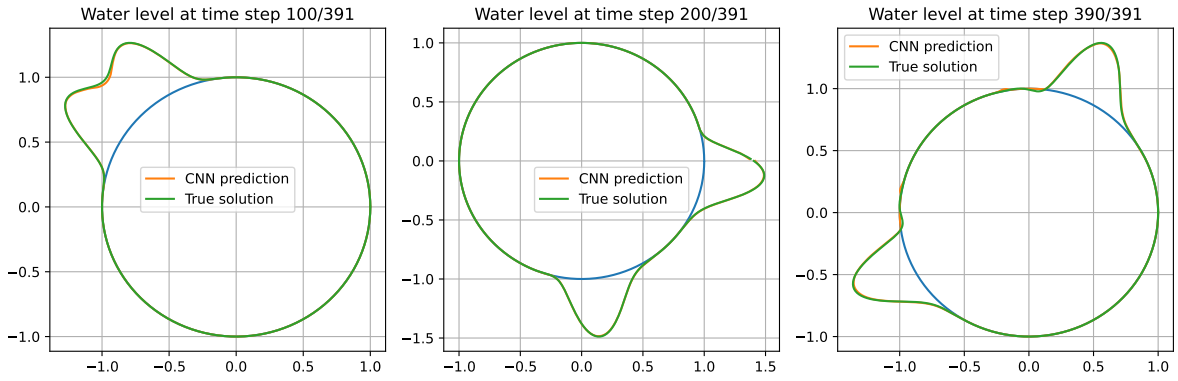

Figure 7.15: Predictions for the spherical shallow water equations in 1D using the CNN model for some given time steps.

FNO model

The FNO model consists of an input channel, 64 hidden channels and an output channel. We use a Fourier basis with 16 modes and a batch size of 32. The model is trained using the Adam optimizer with a learning rate of 0.001 and the critera is to minimize the mean squared error (MSE). The model is trained on the data from $t = 0$ to $t = 0.6$, validated on the data from $t = 0.6$ to $t = 0.8$, and tested on the data from $t = 0.8$ to $t = 1.0$. The training and validation loss is shown in Figure 7.16.

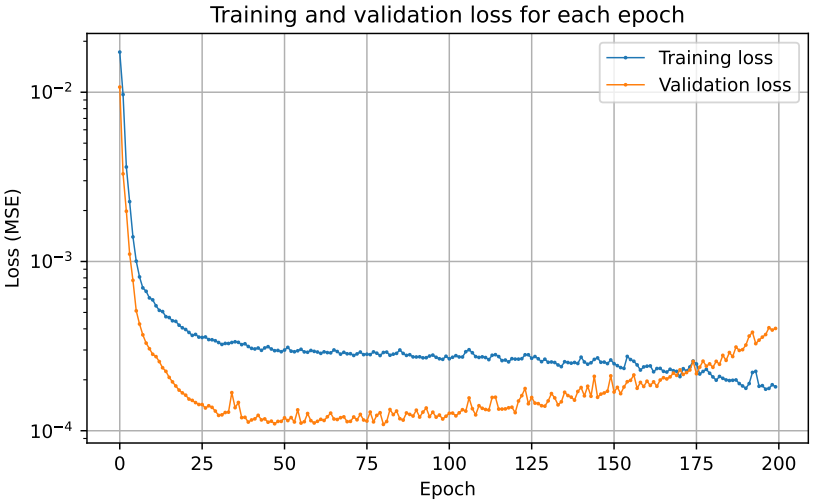

Figure 7.16: Training and validation loss for the FNO model for the spherical shallow water equations in 1D.

Figure 7.16 shows that the training and validation loss decrease over the epochs, indicating that the model is learning the dynamics of the solution. We see that after some time the validation loss increases, indicating that the model is overfitting the training data. The error plots are shown in Figure 7.17.

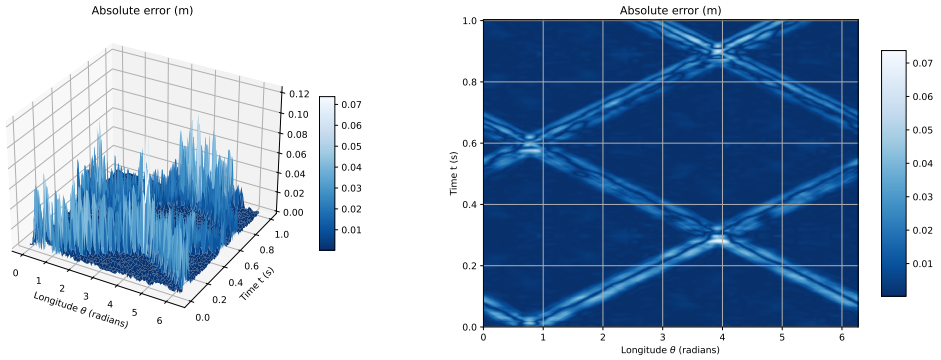

Figure 7.17: Error plots for the predictions of the 1D linearized spherical SWE.

Similar to the CNN model, we observe from Figure 7.17 that the error is largest at the sharp edges of the solution. Furthermore, the plots also indicate that the error increases over time. This is somehow expected, as the model is trained on a limited time interval and may struggle to generalize to unseen data. The predictions for some given time steps are shown in Figure 7.18.

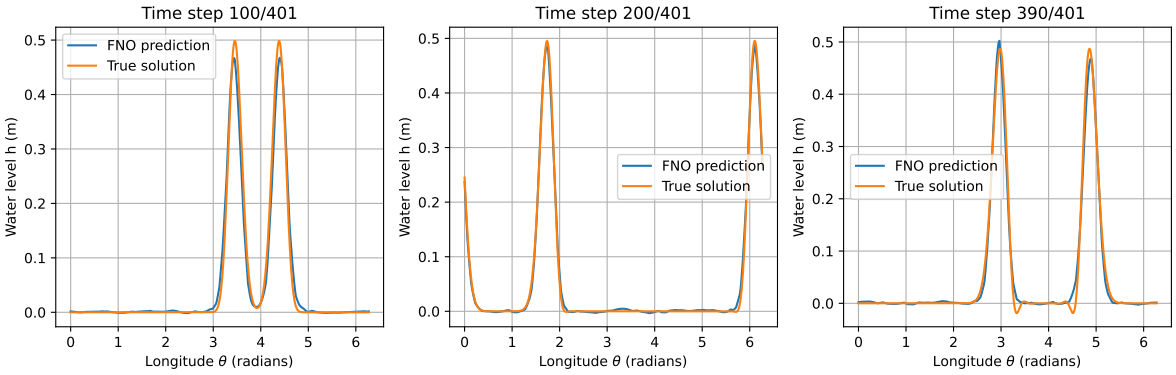

Figure 7.18: Predictions for the spherical shallow water equations in 1D.

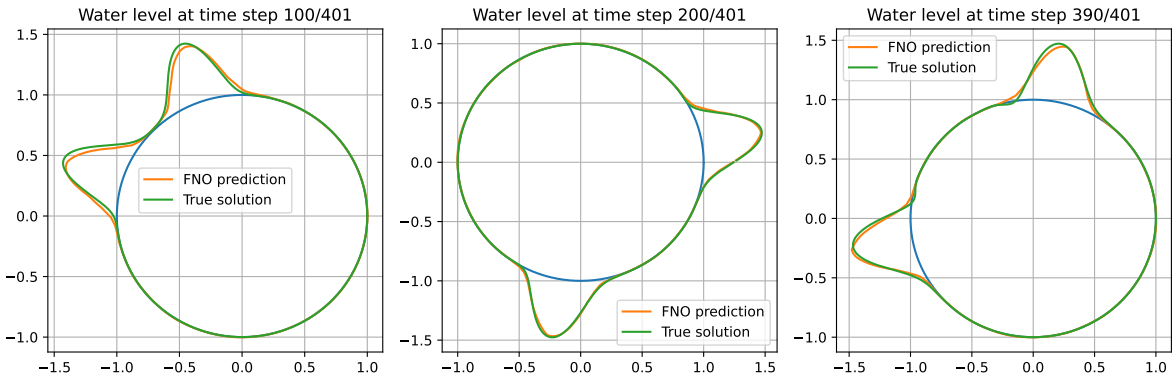

Figure 7.19: Predictions for the spherical shallow water equations in 1D using the FNO model for some given time steps.

The two first plots of Figure 7.18 shows that the FNO model captures the waves really well, but in the last plot we see that the model has some challenges, and for instance is predicting a small wave that is not present in the true solution.

Comparison

We use the MSE and MAE to compare the performance of the CNN and FNO models for the 1D spherical LSWE. In addition, to the results just presented, we have also trained the models for $\sigma = \frac{\pi}{8}$ and $\sigma = \frac{\pi}{32}$. This is done to see how the models perform for different types of initial conditions, depending on how smooth or discontinuous the solution is. The error plots and predictions for given time steps can be found in Appendix section A.1. The results are summarized in Table 7.2.

Model	$\sigma = \pi/8$			$\sigma = \pi/16$			$\sigma = \pi/32$		
	MSE	MAE	Time (s)	MSE	MAE	Time (s)	MSE	MAE	Time (s)
CNN	2.08e-05	2.65e-03	21.22	1.48e-05	1.70e-03	171.27	7.94e-04	1.04e-02	28.17
FNO	1.89e-04	8.42e-03	119.32	1.92e-04	6.81e-03	175.90	4.33e-04	1.05e-02	107.08

Table 7.2: Test loss in terms of MSE and MAE, and time for training the models for the 1D spherical SWE.

From Table 7.2 we see that the CNN model is slightly faster and better than the FNO model for $\sigma = \pi/8$ and $\sigma = \pi/16$, but for $\sigma = \pi/32$, the performance of the CNN model is decreasing. Probably due to the fact that the smaller the σ, the more discontinuous the solution is, and the FNO model is better at capturing the discontinuities. We see that the MAE in general is higher than the MSE, and is also increasing for smaller σ. Additionally, we observe that the MAE is higher, as it places more weight on small errors compared to the MSE.

7.3 Data-driven results for the 2D SWE

In this section we will present the results for the 2D SWE using the data-driven models. We consider the same initial condition (Gaussian function) as in the 1D case, but now in two dimensions. We solve the 2d SWE using both a CNN and a FNO model, and compare the results in terms of run time and accuracy. We also compare the run time to the numerical method FVM, to see if the data-driven models can be used as a faster alternative to the FVM. We also test the ability of the FNO model to generalize to a finer grid, by training the model on a coarse grid and then making predictions on a fine grid. Finally, we will test the FNO model's ability to generalize further in time and make long-term predictions.

The initial condition for the 2D problem is a Gaussian function with a standard deviation of 0.1 and a mean of 0.5. The initial condition is illustrated in Figure 5.5.

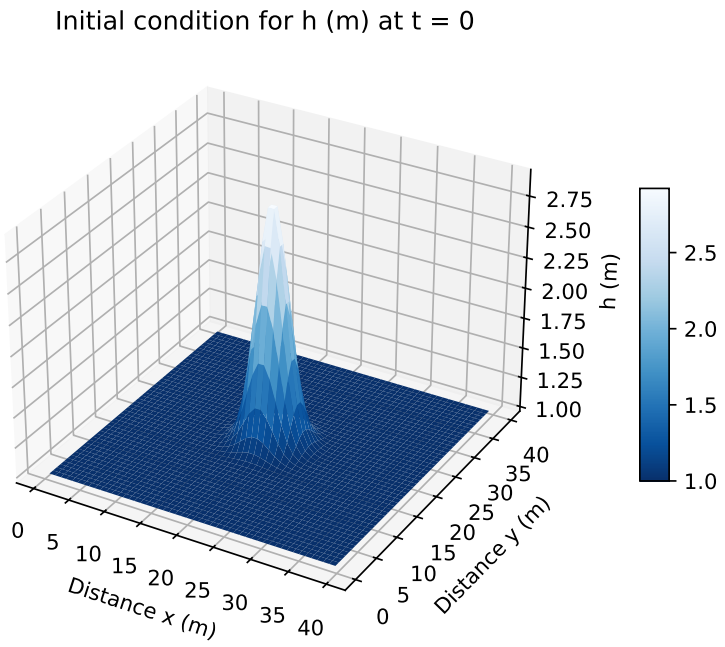

Figure 7.20: Initial condition for the 2D problem.

CNN Model

We train a CNN model with several convolutional layers and ReLU activation functions. We use the Adam optimizer with a learning rate of 0.001 and a batch size of 32. The model is trained on the data for 60% of the time steps, validated on 20% of the time steps, and tested on the last 20% of the time steps. We make predictions from $t = 0$ to $t = 5$. The model is trained for 500 epochs. The training and validation loss for the 2D CNN model can be seen in Figure 7.21.

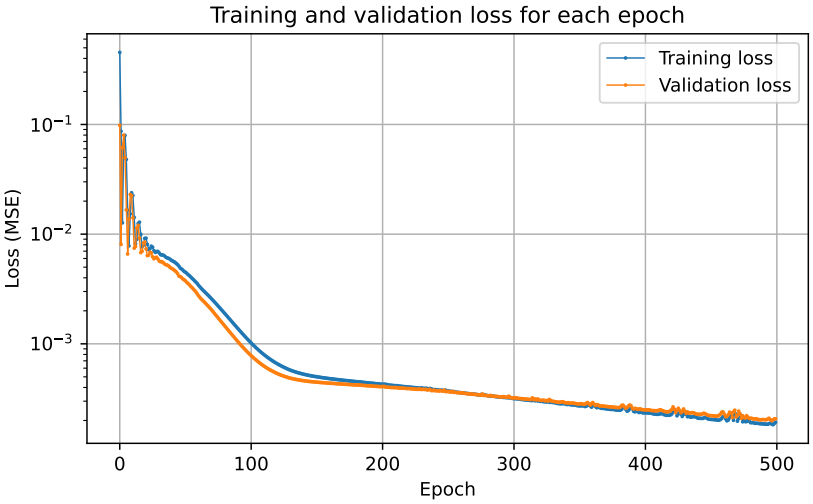

Figure 7.21: Training and validation loss for the 2D CNN model.

Figure 7.21 shows that the training and validation loss are decreasing, as a function of the number of epochs. The error plot for the last prediction for the 2D CNN can be seen in Figure 7.22.

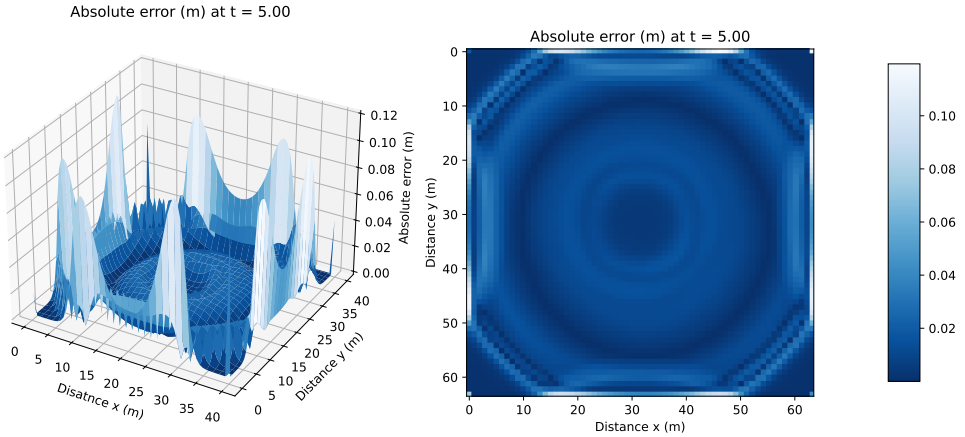

Figure 7.22: Error plot for the last prediction for the 2D CNN.

From Figure 7.22, we see that overall the absolute error is small, meaning that the CNN model is able to learn the dynamics of solution. The error is largest at the boundaries. This may be due to the fact that in this case we are working with boundary conditions simulating a wall. Hence, when the wave hits the wall, the wave is reflected, and the model has to learn the reflection of the wave. This may also lead to discontinuities in the solution, which can be difficult for the model to handle.

FNO Model

We train a FNO model with the same training/validation/testing split as for the CNN model. The FNO model uses 8 Fourier modes, the Adam optimizer with a learning rate of 0.001, and a batch size of 10. The model is trained for 500 epochs. The training and validation loss for the 2D FNO model can be seen in Figure 7.23.

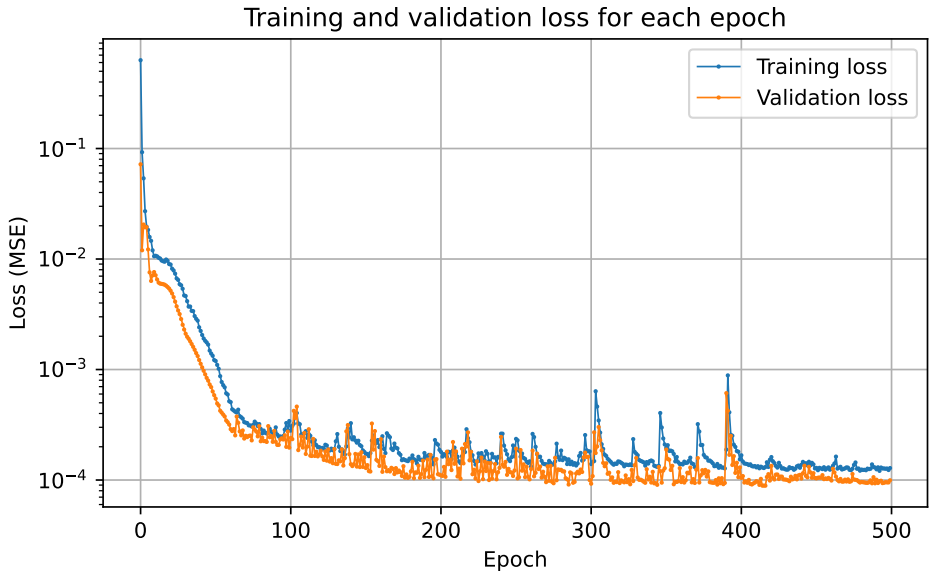

Figure 7.23: Training and validation loss for the 2D FNO model.

From Figure 7.23 we see that the training and validation loss are decreasing, and more or less stable with some fluctations. The plot suggests that the model has converged. The error plot for the last prediction for the 2D FNO can be seen in Figure 7.24.

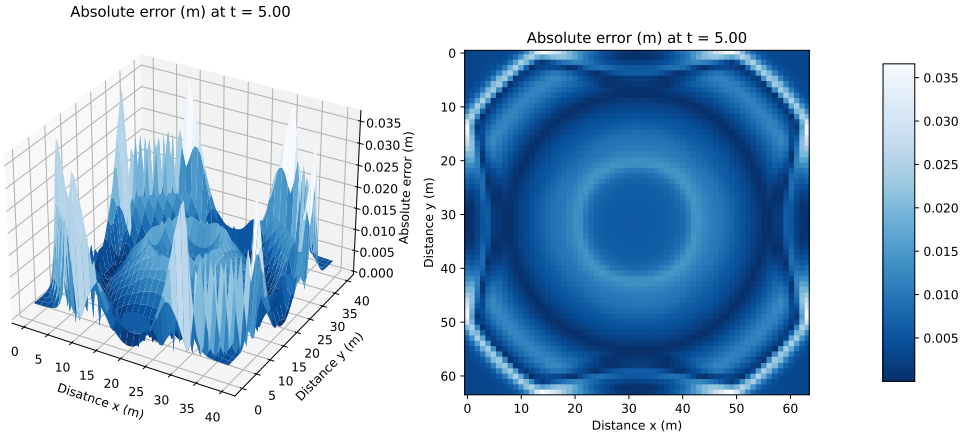

Figure 7.24: Error plot for the last prediction for the 2D FNO.

As for the CNN model, the error is largest at the boundaries. However, we notice that the absolute error is smaller for the FNO model compared to the CNN model.

Comparison

We compare the performance of the CNN and FNO models in terms of the MSE and MAE for the predictions. We test for both $N = 64$ and $N = 128$ grid points in each direction. The errors are calculated for the test data, i.e.,

the last 20% of the time steps. The results are summarized in Table 7.3, together with the time for training the models.

Model	$N = 64$				$N = 128$			
	Epochs	MSE	MAE	Time (s)	Epochs	MSE	MAE	Time (s)
CNN	500	4.34e-04	1.35e-02	59.94	100	5.95e-04	1.28e-02	106.85
FNO	500	1.59e-04	9.21e-03	526.49	100	7.54e-05	4.41e-03	634.74

Table 7.3: Test loss in terms of MSE and MAE, and time for training the models for the 2D SWE.

We see that the FNO model in general needs fewer epochs to converge compared to the CNN model, but it also takes longer time to train. From the theory we know that FNO are supposed to work when we are training on a coarse grid and then make predictions on a fine grid. To test this, we will train the models on a coarse grid and then make predictions on a fine grid. The table below shows the results when the models are trained on a grid with $N = 64$ and subsequently making predictions on a finer grid with $N = 128$.

Model	$N = 128$				
	Epochs	MSE	MAE	Training time (s)	Prediction time (s)
CNN	100	1.58e-02	1.58e-02	13.83	1.01
FNO	100	1.35e-04	6.26e-03	92.85	5.57

Table 7.4: Test loss in terms of MSE and MAE, and time for training the FNO model on a grid with $N = 64$ and then making predictions on a grid with $N = 128$.

From the results in Table 7.4 we see that the errors for the FNO model are small, meaning that the FNO model is able to generalize to a finer grid. The CNN model has a higher error and if it is accurate enough depends on the application. This way, it is possible to train the FNO model on a coarse grid and then make predictions on a fine grid, which is a great advantage when solving the SWE numerically, as it is very computationally expensive to solve the SWE on a fine grid using the FVM. By comparing the run time of the FVM, see Table 6.3, we observe that the data-driven models offer an alternative, which may be advantageous depending on the specific application. This approach provides a potential solution to the scalability challenges we are facing when solving the SWE numerically. To test this ability further, we will train the models on a grid with $N = 64$ and then make predictions on a grid with $N = 256$. The results are summarized in Table 7.5.

Model	$N = 256$				
	Epochs	MSE	MAE	Training time (s)	Prediction time (s)
CNN	100	3.11e-02	3.11e-02	12.22	13.84
FNO	100	8.34e-04	1.89e-02	85.19	90.10

Table 7.5: Test loss in terms of MSE and MAE, and time for training the FNO model on a grid with $N = 64$ and then making predictions on a grid with $N = 256$.

The results in Table 7.5 show that the FNO model is able to generalize to a grid with $N = 256$. While the errors are a bit higher than for the predictions on a grid with $N = 128$, the errors are still small, and for many applications the errors may be acceptable. The results for the CNN model are not as good as for the FNO model, but the CNN model is still, to some extent, able to generalize to a finer grid.

Long-term predictions

We are particularly interested in evaluating the models' ability to generalize further in time. To do this we train the model on the generated 2D data with a fixed time step size of $\Delta t = 0.0025$. To test this, we will train the models on a time interval $[0, 5]$ and make predictions for up to $n = 200$ time steps in the future.

Initially, we adopted an iterative approach, where the model made a prediction for the next time step and used that prediction as input for the next time step. While this approach produces acceptable results for the inital time steps, the error increases as we make predictions further in time, probably due to accumulating errors. To address this issue, we implemented an alternative approach by creating sequences of data and training the model to predict the next time step based on the entire sequence. In this method, the most recent prediction becomes part of a sequence, distributing the influence across subsequent predictions, rather than heavily impacting the next prediction alone. This approach aims to stabilize long-term predictions. The error plot for the long-term predictions from the CNN model can be seen in Figure 7.25.

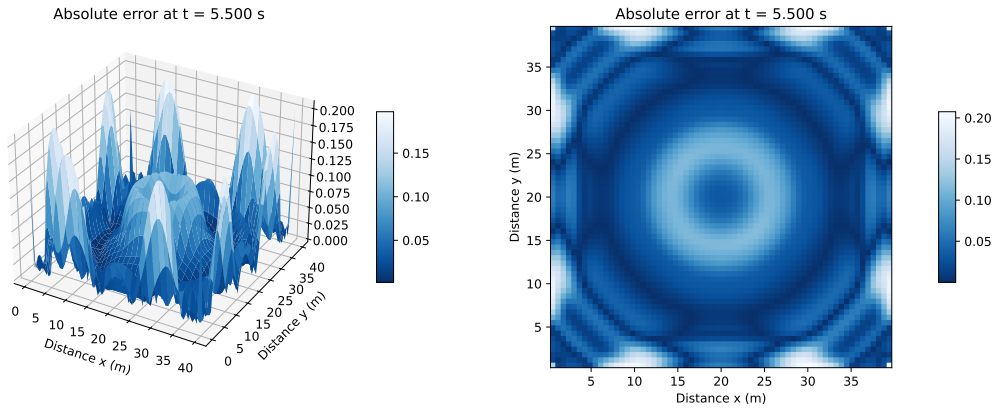

Figure 7.25: Error plot for the long-term prediction for the 2D CNN model.

Figure 7.25 shows that the error is larger for the short-term predictions in Figure 7.22 compared to the long-term predictions. But it has not increased drastically. We run the same test for the FNO model. The error plots of the long-term predictions from the FNO model after 20 time steps, equivalent to $t = 0.5$ s, can be seen in Figure 7.26.

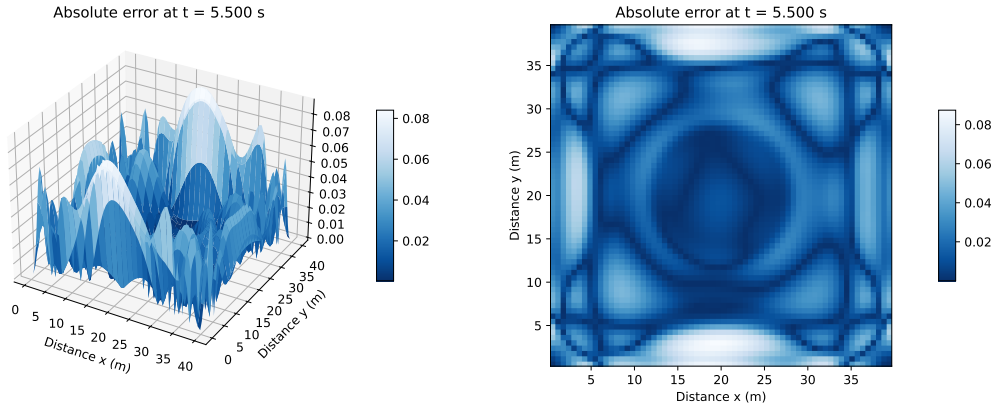

Figure 7.26: Error plot for the long-term prediction for the 2D FNO model.

From the error plot in Figure 7.26, we see that the error is bigger than for the short-term predictions in Figure 7.24, but for many applications still acceptable. We also see that error for the FNO model is smaller than for the CNN model, indicating that the FNO model is able to generalize further in time and make long-term predictions. A plot of the predictions and the ground truth can be found in Figure A.13 in Appendix section A.3. The corresponding error plot for $n = 40$ time steps can be seen in Figure A.14 in Appendix section A.3, where we see that the error has increased.

To get an overview of how the model performs over time, we plot the error in each time step for the long-term prediction for up to $n = 200$ time steps in the future. To compare the error we have plotted the MSE, MAE and the max error for the long-term predictions for the CNN and FNO models in Figure 7.27.

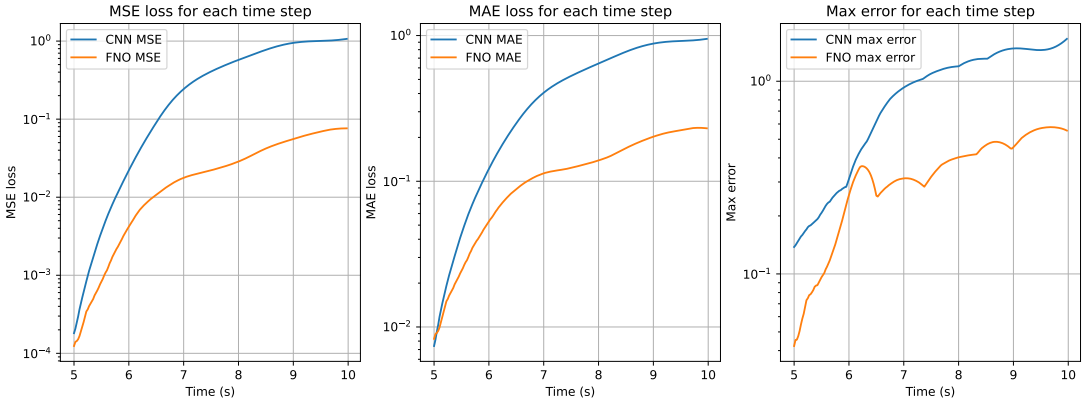

Figure 7.27: MSE, MAE and max error for the long-term predictions for the 2D CNN and FNO models.

When making predictions, it is essential to consider the physical properties of the system, rather than relying solely on the loss functions. The choice of error metric should align with the goals of the predictions. For instance, it may be more important to minimize the MSE or the maximum absolute error, depending on the physical properties of the system. This raises a key question: is it better to have one large error or many small errors?

As shown in Figure 7.27, the error increases as we make predictions further in time. Overall, the FNO model demonstrates lower errors compared to the CNN model, indicating it may offer more accurate long-term predictions.

Chapter 8

Discussion

Chapter 9

Conclusion

- By training the FNO on a coarse grid and evalue on a fine grid, the run time is XX times faster, while maintaining the same accuracy.
- Long-term prediction: the FNO can predict the solution for a longer time than the training time. However, I do not have good results for training on coarse grid, predicting for a fine grid for long-term prediction.
- Long-term prediction: the FNO model outperforms the CNN model for long-term prediction.
- Grid independence: when training on a coarse grid and evaluating on a fine grid, the predictions by the FNO is much better than the predictions by the CNN. Aligning with the theory that FNOs are grid independent.
- Efficiency: CNN is faster than FNO, but FNO is more accurate. Which we prefer depends on the application.
- CNN has shown potential for many of the same abilities as the FNO - especially in the 1D case.
- Some of the theoretical advantages of the FNO are better realized in the 2D case than in the 1D case.

9.1 Further work

Bibliography

[1] European Space Agency (ESA). Valencia flood disaster, 2024. Accessed: 2024-12-27.

[2] E.F. Toro. *Shock-Capturing Methods for Free-Surface Shallow Flows*. Oxford University Press, 2001.

[3] E.F. Toro. *Riemann Solvers and Numerical Methods for Fluid Dynamics*. Springer, 2009.

[4] E.F. Toro. *Computational Algorithms for Shallow Warer Equations*. Springer, 2024.

[5] Ilya Peshkov. Advanced numerical methods for environmental modeling. https://www.unitn.it/dricam/1116/advanced-numerical-methods-environmental-modeling, 2023. Lecture notes.

[6] Manuel J. Castro, Sergio Ortega, and Carlos Parés. Well-balanced methods for the shallow water equations in spherical coordinates. https://www.sciencedirect.com/science/article/pii/S0045793017303237, 2017.

[7] Alex Bihlo and Roman O. Popovych. Physics-informed neural networks for the shallow-water equations on the sphere. *Journal of Computational Physics*, 456:111024, 2022.

[8] David J. Raymond. Shallow water on a sphere. http://kestrel.nmt.edu/~raymond/classes/ph332/notes/sphere/sphere.pdf, New Mexico Tech. Accessed 2024.

[9] L. Gavete, B. Alonso, M.L. Gavete, F. Ureña, and J.J. Benito. An adaptive solver for the spherical shallow water equations. *Mathematics and Computers in Simulation*, 79(12):3466–3477, 2009. The International Conference on Approximation Methods and numerical Modeling in Environment and Natural Resources.

[10] Joseph Galewsky, Richard K. Scott, and Lorenzo M. Polvani. An initial-value problem for testing numerical models of the global shallow-water equations. *Tellus A: Dynamic Meteorology and Oceanography*, Jan 2004.

[11] Zongyi Li, Nikola Kovachki, Kamyar Azizzadenesheli, Burigede Liu, Kaushik Bhattacharya, Andrew Stuart, and Anima Anandkumar. Fourier neural operator for parametric partial differential equations. https://arxiv.org/pdf/2010.08895, 2021.

[12] Boris Bonev, Christian Hundt, Thorsten Kurth Jaideep Pathak, et al. Modeling earth's atmosphere with spherical fourier neural operators. https://developer.nvidia.com/blog/modeling-earths-atmosphere-with-spherical-fourier-neural-operators/, 2023.

[13] Boris Bonev, Thorsten Kurth, Christian Hundt, Jaideep Pathak, Maximilian Baust, Karthik Kashinath, and Anima Anandkumar. Spherical fourier neural operators: Learning stable dynamics on the sphere. https://arxiv.org/abs/2306.03838, 2023.

[14] Keiron O'Shea and Ryan Nash. An introduction to convolutional neural networks, 2015.

[15] François Chollet. A comprehensive guide to convolutional neural networks — the eli5 way. *Towards Data Science*, 2017. Accessed: 2024-12-27.

[16] C.B. Vreugdenhil. *Numerical Methods for Shallow-Water Flow*. Kluwer Academic Publishers, 1994.

[17] Wikipedia. Leibniz integral rule. https://en.wikipedia.org/wiki/Leibniz_integral_rule, 7/10-2024.

[18] Adrian E. Gill. *Atmosphere-Ocean Dynamics*. Academic Press, 1982.

[19] Longitude and latitude map with degrees. https://animalia-life.club/qa/pictures/longitude-and-latitude-map-with-degrees, Accessed: 2024.

[20] Wikipedia. Coriolis force. https://en.wikipedia.org/wiki/Coriolis_force, 14/11-2024.

[21] Boris Bonev, Jan S. Hesthaven, Francis X. Giraldo, and Michal A. Kopera. Discontinuous galerkin scheme for the spherical shallow water equations with applications to tsunami modeling and prediction. *Journal of Computational Physics*, 362:425–448, 2018.

[22] Claes Eskilsson and Spencer J. Sherwin. Discontinuous galerkin spectral/hp element modelling of dispersive shallow water systems. *Journal of Scientific Computing*, 22:269–288, 2005.

[23] Randall J. LeVeque. *Finite Volume Methods for Hyperbolic Problems*. Cambridge Texts in Applied Mathematics. Cambridge University Press, 2002.

[24] A. P Engsig-Karup and J. S. Hesthaven. An introduction to discontinuous galerkin methods for solving partial differential equations. https://www2.compute.dtu.dk/~apek/DGFEMCourse2009/, 2009. Lecture notes.

Appendix A

Appendix

The code can be found at: `https://github.com/MelissaJessen/Shallow-Water-Equations`.

A.1 Additional figures from 1D SWE spherical CNN and FNO

Results for the other sigma values.

CNN, $\sigma = \frac{\pi}{8}$.

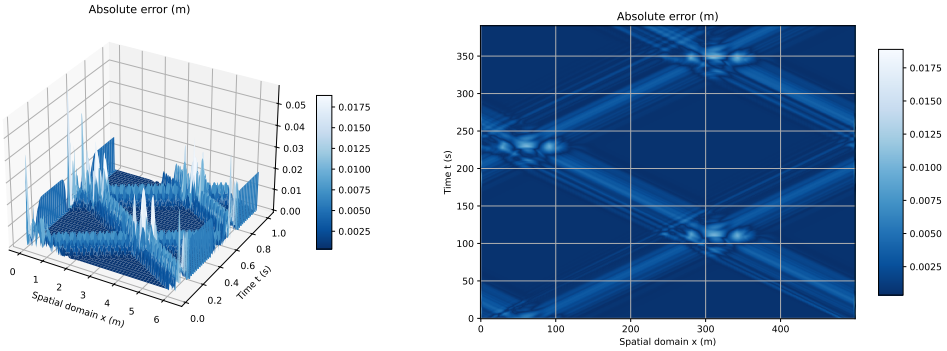

Figure A.1: Error for the 1D SWE spherical CNN with $\sigma = \frac{\pi}{8}$.

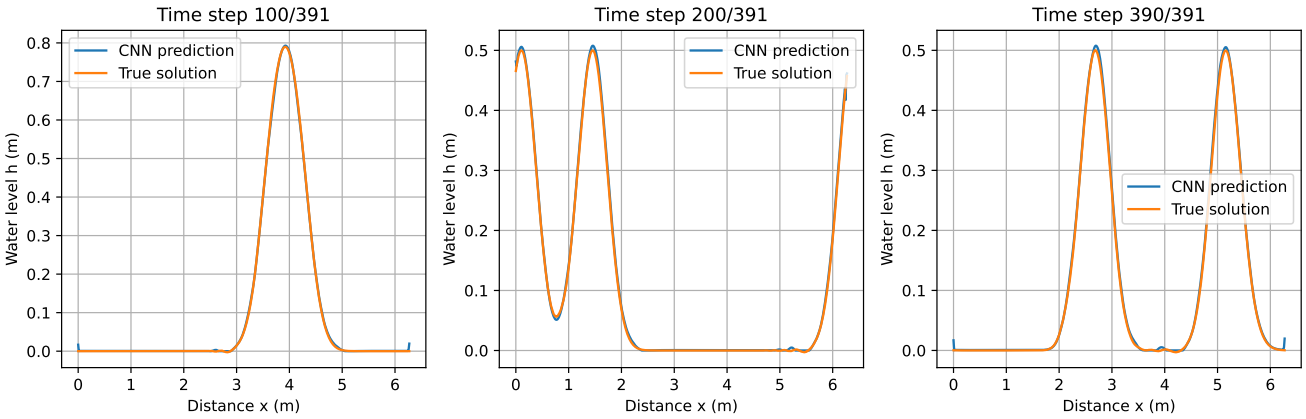

Figure A.2: Results for the 1D SWE spherical CNN with $\sigma = \frac{\pi}{8}$.

FNO, $\sigma = \frac{\pi}{8}$.

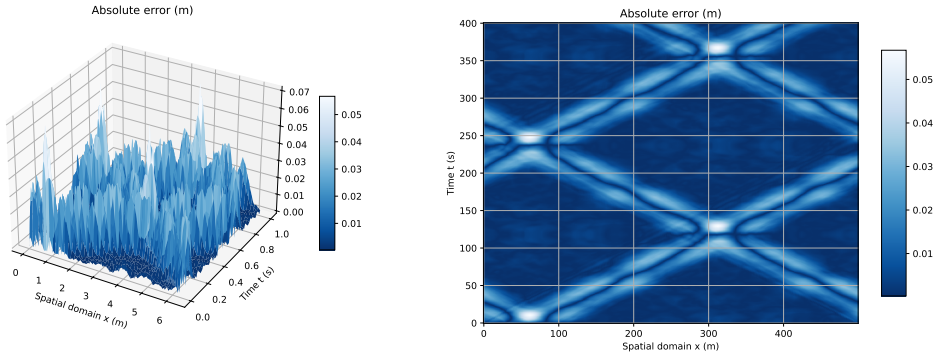

Figure A.3: Error for the 1D SWE spherical FNO with $\sigma = \frac{\pi}{8}$.

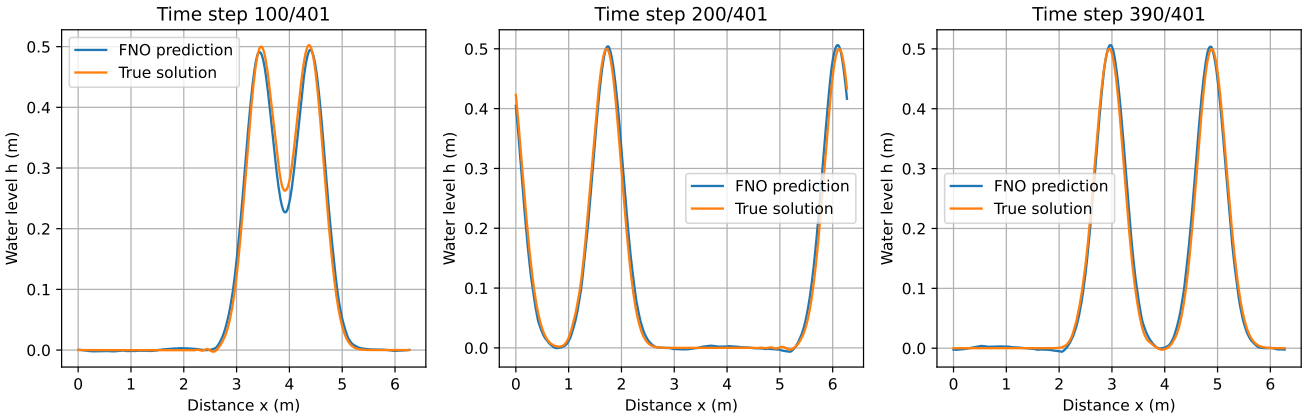

Figure A.4: Results for the 1D SWE spherical FNO with $\sigma = \frac{\pi}{8}$.

CNN $\sigma = \frac{\pi}{32}$.

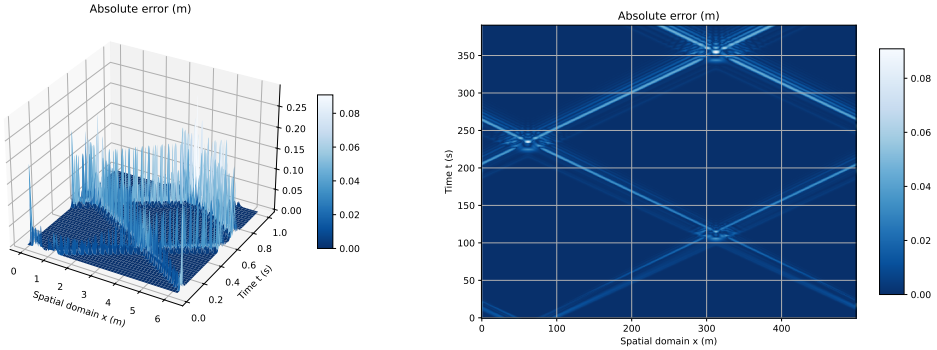

Figure A.5: Error for the 1D SWE spherical CNN with $\sigma = \frac{\pi}{32}$.

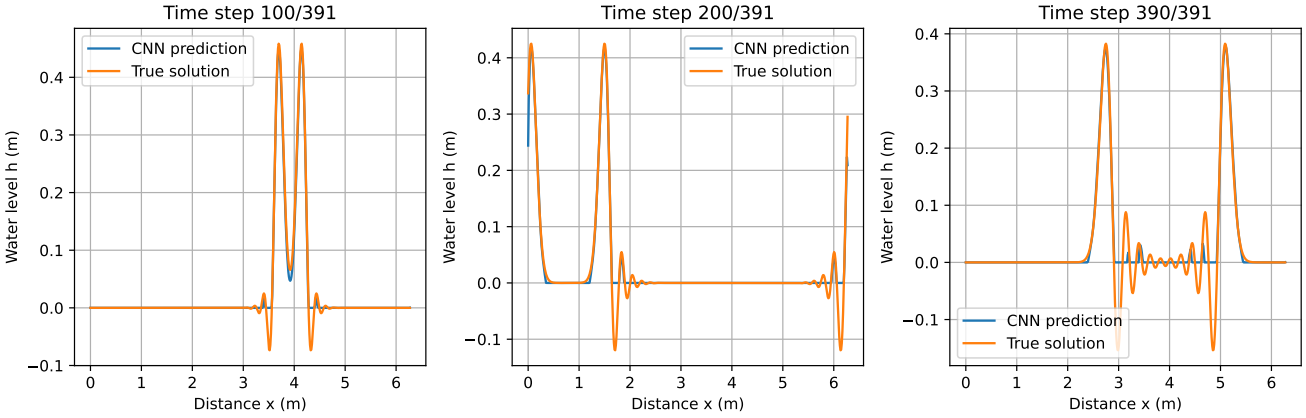

Figure A.6: Results for the 1D SWE spherical CNN with $\sigma = \frac{\pi}{32}$.

FNO $\sigma = \frac{\pi}{32}$.

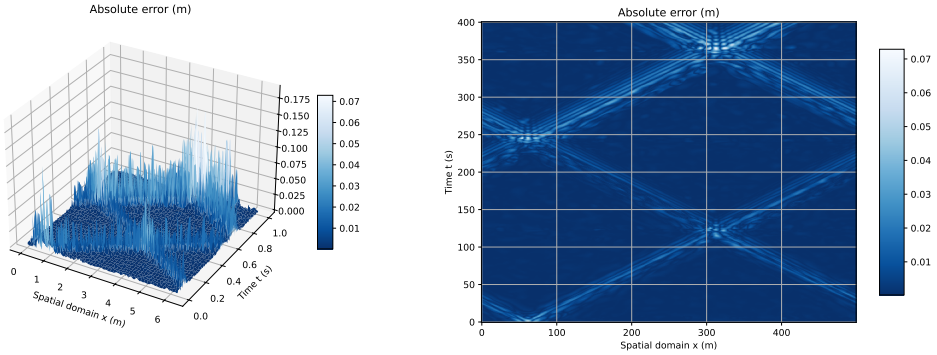

Figure A.7: Error for the 1D SWE spherical FNO with $\sigma = \frac{\pi}{32}$.

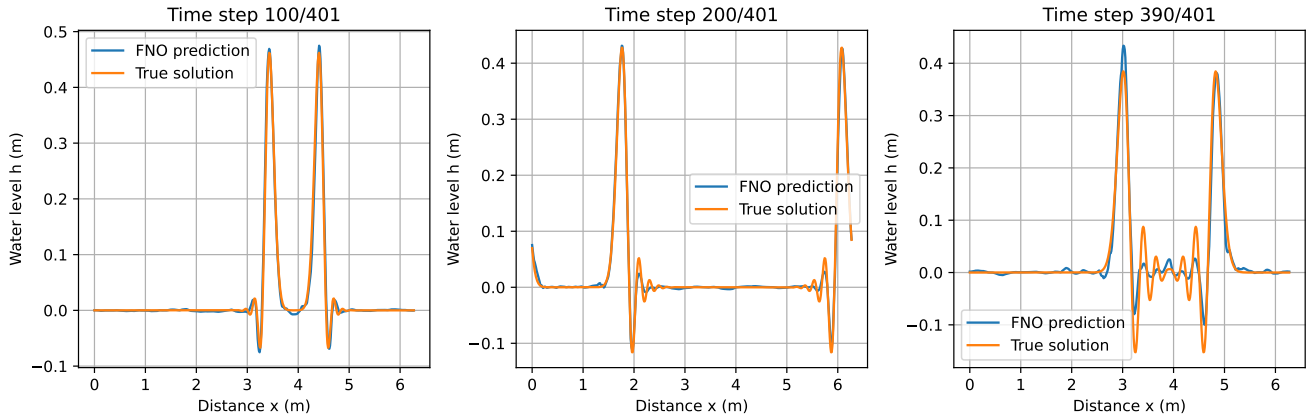

Figure A.8: Results for the 1D SWE spherical FNO with $\sigma = \frac{\pi}{32}$.

A.2 FNO Toro test 1

To test the FNO model on a more challenging problem, we consider the Toro test case 1. We use the same model as before, but we train it on the data from the Toro test case 1. Again, we use the first 80% of the data for training and the last 20% for testing. The results of the model are shown in Figure A.10 and **??**.

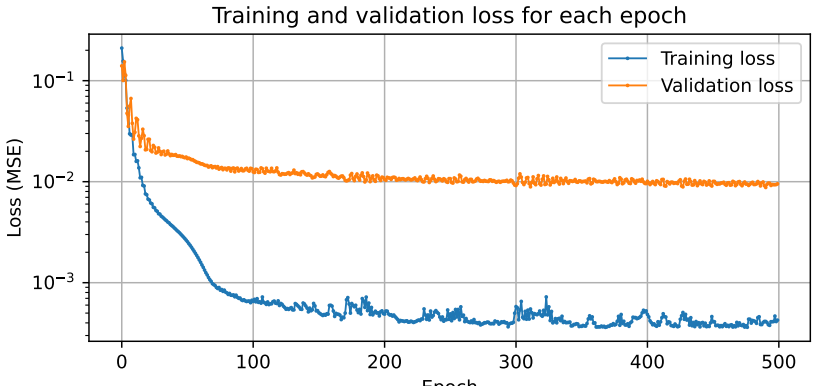

Figure A.9: FNO Toro test 1 loss.

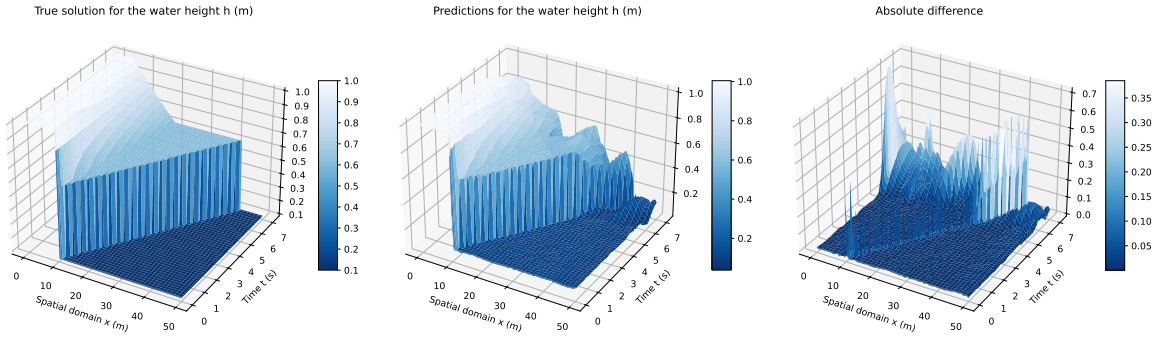

Figure A.10: FNO Toro test 1 predictions in 3d.

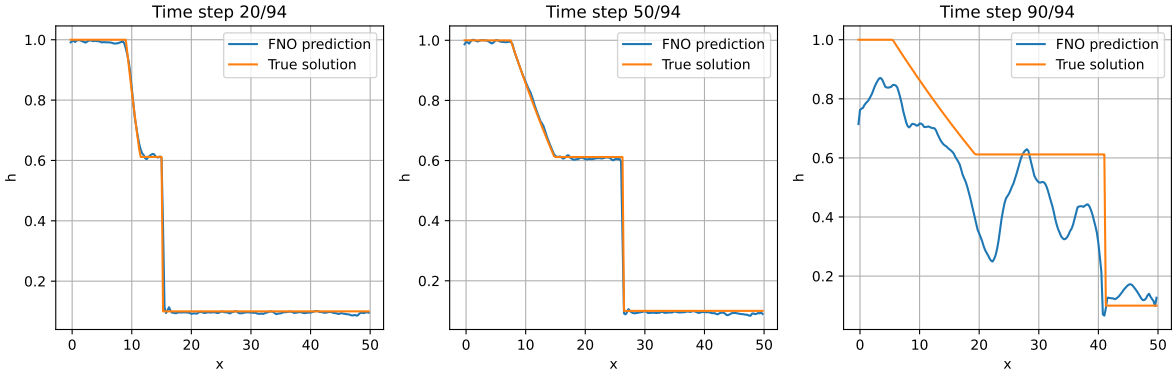

Figure A.11: FNO Toro test 1 predictions timesteps.

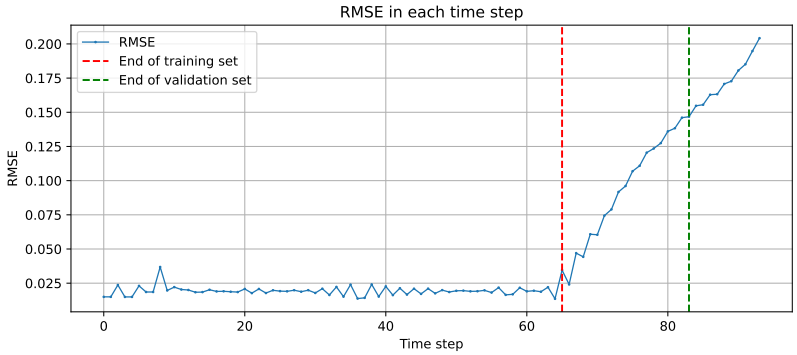

Figure A.12: FNO Toro test 1 predictions RMSE.

A.3 2D SWE long term prediction

The results for the long-term predictions can be seen in Figure A.13.

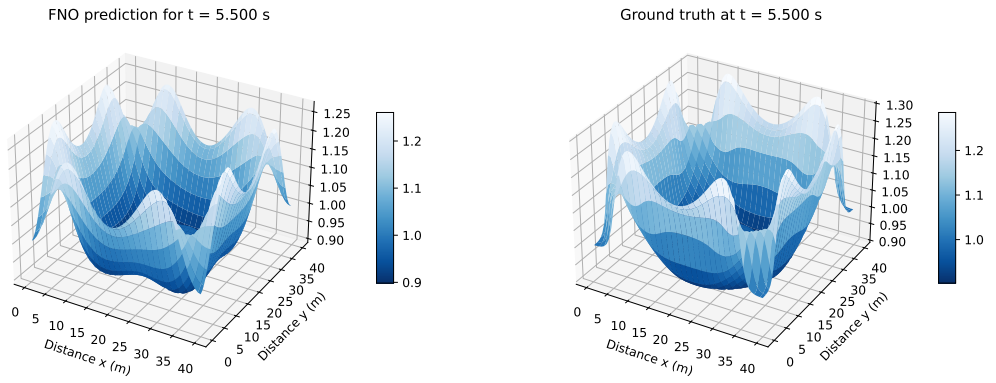

Figure A.13: Long-term prediction for the 2D FNO model.

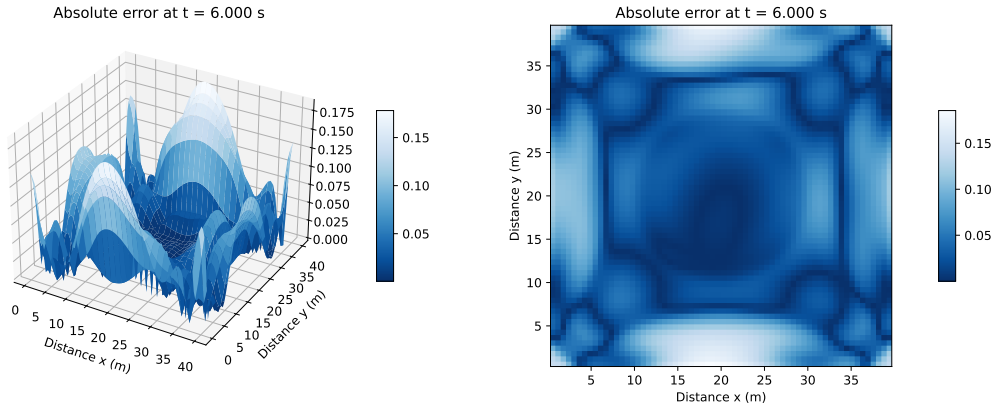

Figure A.14: Error plot for the long-term prediction for the 2D FNO model.

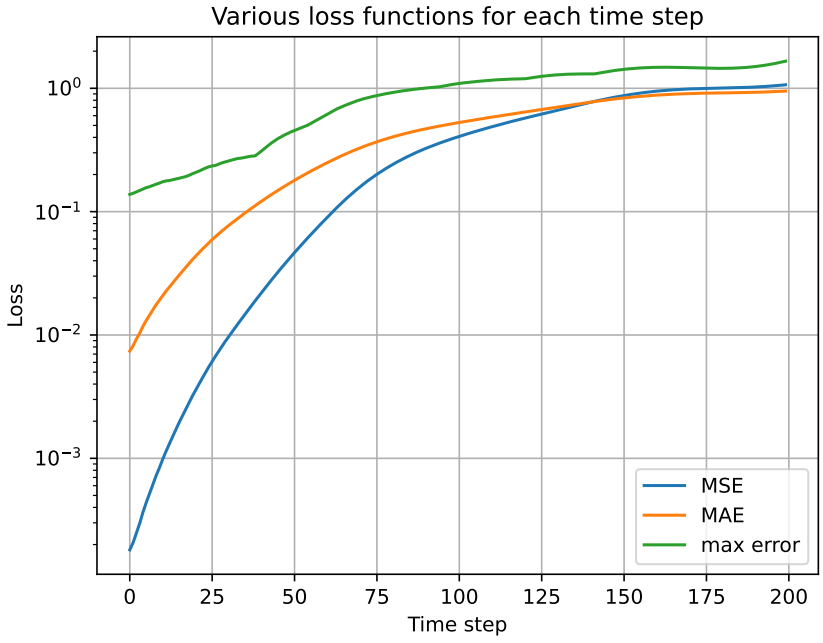

Figure A.15: MSE and MAE for the long-term predictions for the 2D CNN model.

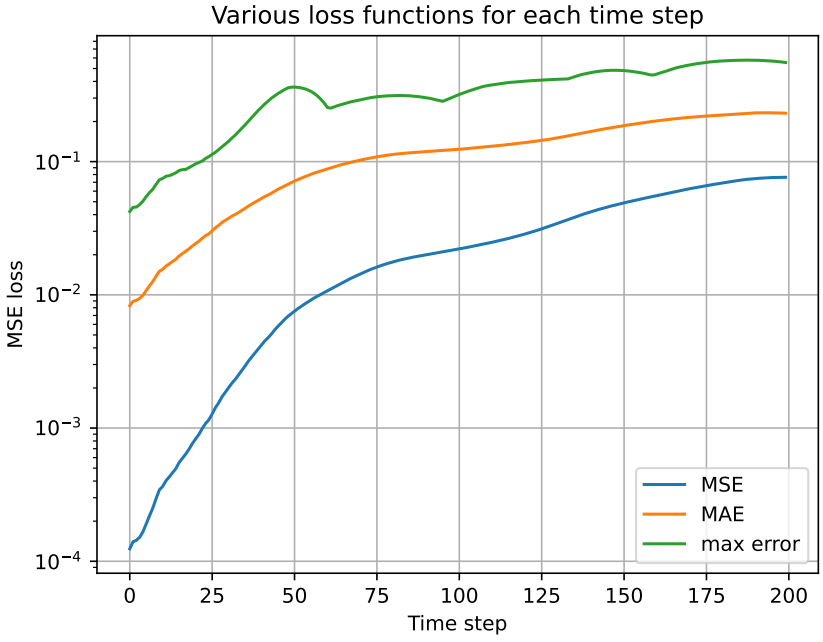

Figure A.16: MSE and MAE for the long-term predictions for the 2D FNO model.